A study of Arctic sea ice freeboard heights, gravity anomalies and dynamic topography from ICESat measurementes

Skourup, Henriette

Publication date:
2010

Document Version
Publisher's PDF, also known as Version of record

FACULTY OF SCIENCE
UNIVERSITY OF COPENHAGEN

PhD thesis

Henriette Skourup

A study of Arctic sea ice freeboard heights, gravity anomalies and dynamic topography from ICESat measurements

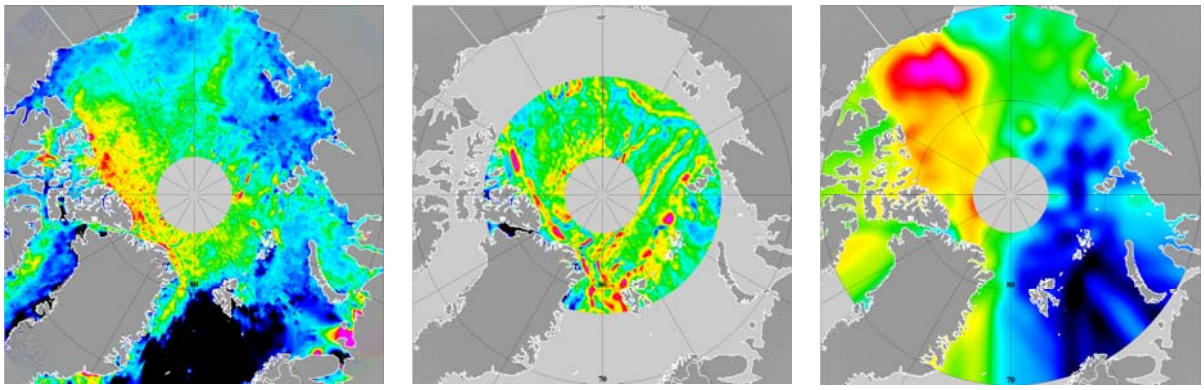

Supervisor: Carl Christian Tscherning

Co-supervisor: Rene Forsberg

Submitted: 04/11/09

DTU Space
National Space Institute

Resume

Havisen, der dækker det arktiske ocean, har en stor indflydelse på klimaet og påvirkes ligeledes hurtigt af klima forandringer. Siden 2003 har NASA's satellit ICESat (Ice, Cloud and land Elevation Satellite) observeret jordens overflade op til 86° N med et laser altimeter. I denne afhandling er hovedformålet at bestemme havoverfladen i det isdækkede arktiske ocean ved brug af observationerne opsamlet af ICESat's altimeter. Og at anvende denne til at bestemme fribordet (højden af isen over havoverfladen), tyngdefeltet samt havets topografi, der afspejler den storskala havcirkulation.

Laser altimeteret måler med stor nøjagtighed afstanden fra satellitten til en reflekterende overflade. Grundet bevægelsen af havisen i det Arktiske ocean, opstår der revner med åbent vand i isdækket. Ved at lokalisere disse åbent vands områder i satellit observationerne, kan de anvendes som reference for havoverfladen. Her anvendes en metode der udvælger de laveste højder i datasættet og antager, at disse stammer fra åbent vand. Havoverfladen findes ved at fitte en glat kurve mellem de udvalgte punkter. Metoden er oprindeligt udviklet til opmålinger fra fly, og er her tilpasset observationer foretaget fra satellit. Metoden er afhængig af, at de udvalgte punkter stammer fra åbent vand. Sammenligning af tilsvarende højopløselige målinger fra fly viser at metoden undervurderer højden af fribordet i områder med tyk is eller høj iskoncentration.

Overordnet er den geografiske fordeling af isens fribord sammenfaldende med den geografiske fordeling af tyk polaris (> 2 m tyk is) målt fra satellit med QuikSCAT scatterometeret. Fra begyndelsen af ICESat observationerne i 2003 er isens fribord reduceret med 10 - 15 cm, hvilket svarer til $\sim$ 70 - 75 cm istykkelse.

Tyngdefeltet bestemt fra ICESat data afbilder de tektoniske områder samt havrygge og plateauer. Sammenlignes resultaterne over havis med flymålinger og eksisterende tyngdemodeller, er kvaliteten på højde med tilsvarende målinger over åbent hav. Havets topografi afspejler storskala cirkulationen i det arktiske ocean, f.eks. den anti-cyklone havstrøm i Beaufort havet og de lavere højder over det Grønlandske hav. Hav topografien bestemt fra ICESat observationer er i god overensstemmelse med eksisterende oceanografiske modeller.

Abstract

The Arctic sea ice cover has a great influence on the climate and is believed to respond rapidly to climate changes. Since 2003 the Ice, Cloud and land Elevation Satellite (ICESat) laser altimetry mission has provided satellite altimetry over the ice covered Arctic Ocean up to 86° N. In this thesis, the main topic is to estimate the sea surface height in the Arctic Ocean from ICESat laser altimetry data and to use this information to estimate sea ice freeboard heights, gravity anomalies and mean dynamic topography.

The laser altimeter measures the height of the surface topography, which in the Arctic is a combination of sea ice and open water. The sea surface height is found by a "lowest-level" filtering procedure, originally developed for airborne lidar measurements, which assumes that the lowest levels measured represent the open water in the ice pack. The sea surface obtained this way is used to estimate the sea ice freeboard, and shows good qualitative correlation to QuikSCAT scatterometer data. As the method depends on the presence of open water, the method is underestimating the sea ice freeboard heights, when compared to coincident high resolution airborne lidar measurements in areas with thick ice or ice of high concentration. Overall, a decrease in the mean freeboard heights of approximately 10 - 15 cm (corresponding to $\sim$ 70 - 75 cm in thickness) are observed, since the beginning of the ICESat observations in 2003.

The potential for ICESat derived geoid and gravity anomalies are investigated. The ICESat gravity grid shows all the major tectonic features of the Arctic Ocean at high resolution. The results show that the laser altimetry data provides excellent gravity results comparable to open ocean altimetry even over the most heavy ice conditions. Subtracting a geoid model from the mean sea surface can be used to improve the knowledge of the sea surface topography (semi permanent circulation patterns). The dynamic topography observed by ICESat maps the main circulation in the Arctic, e.g. the Beaufort Gyre and the lower heights in the Norwegian-Greenland Sea. A comparison to existing global and regional oceanographic models of the Arctic mean dynamic topography shows good qualitative agreement.

Preface

This thesis, is submitted in partial fulfilment of the requirements for obtaining the Ph.D. degree at the Niels Bohr Institute, University of Copenhagen. The research presented here was carried out within the Division of Geodynamics, National Space Institute (DTU Space), under the supervision of C. C. Tscherning at University of Copenhagen and R. Forsberg at DTU Space. The Ph.D. program is partly funded by the Danish Natural Science Research Council (FNU) under the Ministry of Science, Technology and Innovation, and part of the initial work is done within the ArcGICE project funded by the European Space Agency (ESA). The thesis includes three published papers with the author as the first author.

The work is inspired by my interest in the nature, which I have been able to combine with my carrier. I received my M. Sc. in geophysics from University of Copenhagen in 2004, and worked as a research assistant at DTU Space until starting this Ph.D. program in January 2006. My experience in sea ice started in 1997, where I began working part time during my studies as a sea ice analyst at the Danish Meteorological Institute.

I have participated in multiple field campaigns since 1999 primarily with airborne altimetry (laser and radar) in the Arctic for retrieval of sea ice freeboard heights, as well as height estimates of glaciers and ice sheets. In addition, I have participated in various airborne gravity surveys in Mongolia and Germany, as well as on-the-ice measurements of gravity in the Arctic as part of the Danish Law of the Sea project working out of ice camps, and most recently from the swedish icebreaker, Oden.

In combination with the research related to this thesis, it has given me insight into the geophysical processes in the Arctic, not only of the sea ice, but also in oceanography and geodesy.

I am deeply grateful to all the people, who have been involved in the process both professionally and in my private life.

In paticular, I give my deepest thanks to my supervisors C. C. Tscherning and R. Forsberg for their support and inspiration; I would also like to thank my co-authors, my colleagues at DTU Space, and my colleagues all over the world with a special thank to A. Braun and V. Renganathan whom I worked with during my visit at the University of Calgary. Furthermore, I would like to thank S. L. S. Sørensen, G. Strykowski, M. Lamplugh, S. M. Olsen and U. L. Bull for professional help and support.

I want to acknowledge, the National Ice and Data Center (NSIDC), Boulder, Colorado, for access to the ICESat data, and the European Space Agency (ESA) for access to ENVISAT data. Furthermore, the QuikSCAT Polar Sea Ice (PSI) data product is downloaded from CERSAT, at Ifremer, Plouzané (France), and the sea level pressure fields from NCEP/NCAR NOAA-ESRL PSD Climate Diagnostics Center Branch, Boulder Colorado. Finally, I want to thank; J. Zhang (University of Washington) for his always quick response and for providing the oceanographic model of the dynamic topography, L. Padman (Earth & Space Research) for the tide model, and J. Brozena (Naval Research Laboratory) for the original airborne gravity data.

Henriette Skourup

Copenhagen November, 2009

Cover: ICESat sea ice freeboard heights, gravity anomalies and dynamic topography.

Contents

1 Introduction

The Arctic Ocean sea ice cover is believed to respond rapidly to climate changes, both in extent and thickness. Since the beginning of the satellite era almost 40 years ago the total sea ice extent has decreased by 11.1% per decade in September and 2.8% per decade in March (Richter-Menge et al., 2008) with an extreme minimum in the summer of 2007 (Comiso et al., 2008). The partial coverage of thick perennial sea ice has also decreased and was record low in March 2008 (Nghiem and Neumann, 2009). Again other sources indicate that sea ice in the Arctic Ocean undergoes major thinning, based on submarine (Rothrock et al. (2008), Rothrock et al. (2003), Wadhams and Davis (2000), Tucker III and Weatherly (2001) and Rothrock et al. (1999)), satellite (Laxon et al., 2003) and helicopter (Haas et al., 2008) measurements. Such changes in the Arctic sea ice will have profound implications, potentially opening new shipping routes and opening vast new areas for natural resource exploitation.

Remote sensing techniques such as satellite laser and radar altimetry, give the opportunity to measure surface topography with high precision. In the presence of sea ice, the freeboard (h_f), defined as the part of the ice above the sea surface, can be obtained directly from altimetry observations if the sea surface height is known (h_{ssh});

$$h_f = (H - R) - h_{ssh} \tag{1}$$

where H is the ellipsoidal height of the satellite and R is the measured range. Under assumptions of the snow depth, ice and ocean densities, measurements of freeboard heights allow us to determine the ice thickness and thus remote sensing opens up for the possibility to derive sea ice thickness.

The sea surface height is a combination of the geoid (h_{geoid}), the dynamic topography (h_{DT}) and errors (h_{errors}) occurring from models and measurement inaccuracies;

$$h_{ssh} = h_{geoid} + h_{DT} + h_{errors} \tag{2}$$

where the sea surface height has been corrected for tides and atmospheric pressure loading. Thus if the geoid and dynamic topography are known to a high accuracy, the sea surface height can be modelled directly and the sea ice freeboard heights can be found by equation 1.

Geoid models are available for the Arctic, e.g. through the Arctic Gravity Project (ArcGP) (Kenyon et al., 2008) and more recently Earth Gravitational Model (EGM08) (Pavlis et al., 2008). The models are compiled from various data sources, based primarily on airborne and marine gravity campaigns. Even though these individual surveys are of high quality, there are still some inconsistencies between different campaigns and areas with sparse data or data of poor quality. The estimates of the Arctic dynamic topography, which basically maps the large scale ocean circulation, are so far based on oceanographic models, bottom pressure buoys and satellite gravity missions (CHAMP and GRACE). Intercomparison of different oceanographic models show large variations (Forsberg et al., 2007).

Over the open ocean, classical radar altimetry measures the sea surface height directly and standard methods have been developed to estimate the marine geoid (Sandwell and Smith (1997) and Knudsen et al. (1992)) and the dynamic topography (Fu and Cazenave, 2001). In the Arctic, the presence of sea ice complicates this procedure. However, a method has been developed to observe sea ice freeboard heights from altimetry, which is highly

dependent on identification of open water in ice covered areas. Such knowledge can estimate the sea surface height in the Arctic Ocean and give insight into an altimetry derived geoid and dynamic topography. The ability to map changes in the dynamic topography in the Arctic and thus the underlying ocean circulation provides insight into the basic melting process of the sea ice, since the changing inflow of Atlantic and Pacific waters is believed to be a major source of currently observed sea ice changes (Shimada et al. (2006), Morison et al. (2006), Zhang et al. (1998) and Steele and Boyd (1998)).

1.1 Satellite altimetry missions

Classical satellite altimetry missions started in the beginning of the 70'ies with SKYLAB. Such missions have primarily focused on covering the vast ocean regions and have been launched into polar orbits with relativly low inclination (TOPEX/Poseidon and Jason cover up to 66°N/S; GEOSAT and GFO cover up to 72°N/S) leaving the Arctic Ocean totally uncovered. For Arctic Ocean sea ice freeboard measurements by altimetry, a new era started in 1991 with the launch of the ESA mission ERS-1, followed by ERS-2 and ENVISAT. The satellites were launched into an orbit inclination covering up to 81.5°N and even though these latitudes still leave most of the Arctic Ocean without observations, it includes regions covered with sea ice.

With the increased focus on climate concerns, special dedicated cryosphere altimetry missions have come into existence. The Ice, Cloud and land Elevation Satellite (ICESat), which was launched in January 2003, is part of NASA's earth observing programme primarily for measuring the height changes of icesheets and glaciers using high precision laser altimetry. ICESat covers up to 86°N/S. ESA's cryosphere mission CryoSat-1 was launched in October 2006, but unfortunately a failure in the launch procedure ended the mission few minutes after launch. CryoSat-1 carried a high resolution radar altimeter (SIRAL) to measure the heights of ice sheets, glaciers and icecaps, together with sea ice freeboard heights (Wingham, 1999). The altimeter was supposed to measure the highly varying ice sheet margins with interferometry. The satellite also intended to use a combination of classical radar altimetry and SAR techniques to improve the horizontal resolution better suited for sea ice freeboard measurements than classical altimeters. Furthermore, the orbit for CryoSat was chosen to be in an orbit with unusually high inclination covering up to 88°N/S. Fortunately, a CryoSat-2 is already in production and is expected to be launched in February, 2010.

1.2 Sea surface height in the Arctic

1.2.1 Satellite altimetry

Peacock and Laxon (2004) developed a technique for estimating the sea ice freeboard heights from radar altimetry based on observations from ERS-1/2. The shape of the returned radar signal changes signature depending on the surface characteristics. Over very flat surfaces, the signal shows a characteristic narrow peak compared to rougher surfaces, where the signal is less strong and broader. In sea ice covered waters, the peaked signals originate from open water or very thin ice in between the ice floes, whereas returns from ice floes are of the more broader type. Discriminating the signals in this way, the returns and the corresponding height of the sea surface can be found and thus the sea ice freeboard can be estimated (see equation 1).

The return of the laser altimeter pulses does not show the same characteristic specular returns over flat surfaces. A typical lead dimension is from a few meters to many kilometers wide and from a few meters to several hundred kilometers long (Lindsay and Rothrock, 1995). The relatively small footprint size of a laser altimeter (ICESat $\sim$ 65 m) is an order or two smaller than the classical radar altimeter footprint (ENVISAT and ERS $\sim$ 2 -10 km) and is believed to better pick up the heights of the open leads. In this case, a "lowest-level" filtering procedure is used, where the lowest levels of the altimeter heights are simply assumed to represent open water or very thin ice. The algorithm was originally developed for sea ice freeboard estimates of high resolution airborne lidar measurements by Hvidegaard and Forsberg (2002). Preliminary studies of sea ice freeboard heights from ICESat altimeter measurements have been published in Kwok et al. (2004), Forsberg and Skourup (2005), as well as Kwok et al. (2006). A more detailed study was published in Kwok et al. (2007).

The "lowest-level" filtering method is reliable, if all the altimeter measurements, that are used to determine the reference ocean level, are from open water leads of dimensions larger than the ICESat footprint. However, if the lead is covered by thin ice or only part of the ICESat footprint are from within the lead, there is a bias in the calculated ocean level that would lead to an underestimation of the freeboard height.

1.2.2 Airborne altimetry and *in situ* GPS measurements

Airborne surveying with laser altimetry and on-the-ice measurements with Global Positioning System (GPS) give the opportunity to measure the surface height with higher resolution and precision, than by the use of satellite altimetry. This allows such measurements to be used for validation of satellite altimeter measurements, as well as geoid models.

The airborne laser altimeter used here, is a laser scanner measuring with a horizontal resolution of 1 m x 1 m (Hvidegaard and Forsberg, 2002). The vertical accuracy is in the order of 10 - 20 cm depending primarily on errors in the kinematic GPS-solutions, due to long baselines (Krabill et al., 1995). As a result of the high resolution, the airborne laser scanner data system picks up even the smallest leads and hence freeboard heights from these data should not be biased. In this thesis, airborne laser scanner data is used for validation of sea ice freeboard heights from ICESat.

On-the-ice measurements with a geodetic GPS measures, in principle, the same surface height ($H - R$) as the surface measured by altimetry, thus both equation 1 and 2 applies. The vertical accuracy of the processed data is a few centimeters, which make the GPS measurements usefull for validation of geoid models, as well as ICESat observations of sea surface heights. Of special interest is GPS profiles in fiord systems, where the accuracy of geoid models are uncertain, due to large variations in the geoid related to large variations in bathymetry, topography and geology. Here is included, an experiment with *in situ* GPS measurements in west Greenland to validate geoid models and ICESat sea surface heights in a narrow fiord system.

1.3 This study

In this thesis, the main topic is to estimate the sea surface height in the Arctic Ocean from ICESat laser altimetry data (release 28) from the period 2003 - 2008 and to use this

information to estimate sea ice freeboard heights, dynamic topography and gravity anomalies.

The technique used for sea surface height estimation is based on a "lowest-level" filtering algorithm. Best results are found when taking the lowest levels for each 20 km ($\sim$ 120 ICESat shots) along-track, and assumes these represent open water or thin ice in between the ice floes. A smooth curve determined by least-square collocation (optimal estimation) is fitted through the "lowest-level" points. This curve is assumed to represent the sea surface height. The reliability of the "lowest-level" filtering method is discussed and compared to near coincident high resolution airborne laser scanner measurements in sea ice covered waters north of Greenland.

The sea ice freeboard heights can be estimated directly by subtracting the sea surface heights on a track-by-track basis from the measured altimetry ellipsoidal heights. The sea ice freeboard heights obtained from ICESat are compared qualitatively to the backscatter coefficient from QuikSCAT scatterometer data, where a high backscatter coefficient is correlated with multiyear ice, defined as sea ice thicker than 2 m (Kwok, 2004). A more statistical approach is presented to investigate trends in seasonal and year-to-year variations.

The sea surface height, is dominated by long wavelength geoid undulations. The dynamic topography of the Arctic is derived by subtracting a geoid model (here using ArcGP) from the sea surface heights. The results are compared to an oceanographic model from University of Washington, and the coupling to large scale atmospheric circulation is investigated. All of the existing ICESat data is merged into a composite mean sea surface by use of a draping technique. Standard inversion methods and GRACE data are used to compute the gravity anomalies for the Arctic Ocean. The results are compared to the ArcGP gravity anomalies, as well as airborne gravity campaigns. An example is presented of direct GPS measurements of geoid and tides in west Greenland fiords.

1.4 Field campaigns

Field campaigns in the Arctic are an integrated part of this Ph.D. work. The primary task has been to retrieve high resolution sea ice freeboard heights from airborne laser and radar measurements as part of various EU- (DAMOCLES) and ESA (CryoVEx) projects. The DTU Space laser scanner system has been in operation since 1998 and is used with other instruments and *in situ* measurements to collect information on e.g. snow depths, freeboard-to-thickness conversion and radar penetration depths. Three underflights of satellites were carried out as part of this study, to evaluate the sea ice freeboard heights obtained from satellite altimetry. The first underflight was an underflight of ICESat during the spring 2004 over very thick sea ice north of Greenland. To follow up, a similar underflight of ICESat was performed in 2007 north of Alaska to evaluate the method over thinner sea ice types (Hutchings et al. (2008) and Hutchings (2007)). The third underflight was of ENVISAT in the Fram Strait in 2006 to evaluate individual echo waveforms over sea ice and coincident freeboard estimates (Skourup et al. (2007b) and Stenseng et al. (2007)). Unfortunately, only the first underflight turned out to be successful.

In addition, two airborne gravity campaigns, BalGRACE and NorthGRACE, were carried out in October 2006 and June 2007, respectively. The campaigns were a joint project with Bundesamt für Kartographie and Geodäsie (BKG), in order to, improve the gravity field and geoid in the border areas between Germany and Denmark. Results are presented in

Skourup et al. (2008) and Schäfer et al. (2008). These campaigns were relevant for this Ph.D. work, because the primary objective was to determine high resolution local geoids, and thus gave insights into the highest possible accuracy and spectral behaviour in the errors of the Arctic geoid.

In the fall of 2008 airborne measurements of the thickness of the ice margin and glaciers in an area between Kangerlussuaq and Nuuk (Greenland) took place. The project was carried out for the US mining company Alcoa to assist the planning and development of a potential hydroelectric power plant in the area. To measure the thickness of the ice a combination of laser and radar techniques were used, to map the surface and bottom of the ice. The total area covered approximately 10,000 km^2 and were measured with 2 km spacings between parallel tracks. This survey did not cover sea ice, but gave insight into the errors in airborne lidar, due to the many crossover tracks over the ice sheet. For a detailed description of the project see Mottram et al. (2009).

1.5 This report

The content of this thesis is as follows: Chapter 2 gives a brief introduction to the coupled sea ice, atmosphere and ocean environment in the Arctic, e.g. circulation patterns, ice types and settings. Chapter 3 includes a thorough theoretical background of the altimeter operation, with focus on the radar and laser altimeter characteristics and differences. This chapter, also presents a description of the changes in waveforms expected as the altimeter moves from open ocean into an ice covered area, and the response of the altimeter to geophysical effects.

Chapter 4 gives a description of the data used in this project, with focus on the corrections and filtering applied to the ICESat data, and includes a presentation of the various geophysical models used, either directly in the processing or to compare to the results. Chapter 5 introduces the "lowest-level" filtering technique, followed by the method to estimate the sea ice freeboard heights, the ocean dynamic topography, as well as the gravity anomalies. Chapter 6 presents the results and these are discussed in details. Finally chapter 7 contains the conclusion and chapter 8 an overview of future operations.

The freeboard maps of all ICESat (data release 28) results are enclosed in appendix A together with the corresponding QuikSCAT backscatter maps. Freeboard results from earlier ICESat data release 18 are enclosed in appendix B, and information on the sea ice extent can be found in appendix C. Appendix D and E include a brief presentation of the airborne underflights of ICESat in April 2007 and of ENVISAT in May 2006.

In appendix G are enclosed the three published papers, which are included in this thesis. Skourup and Forsberg (2006) gives a detailed description of the airborne underflight of ICESat. The paper by Skourup et al. (2007a) includes a presentation of the gravity anomalies of the Arctic Ocean obtained from ICESat data (release 18), and the results are compared to high precision airborne gravity data. The paper by Skourup and Forsberg (2008) includes a presentation of ICESat derived dynamic topography, as well as the validation of geoid models and ICESat sea surface heights from *in situ* GPS measurements along a profile in a west Greenland fiord system.

Prints of the two main programs, programmed and used in this thesis, are enclosed in appendix F.

2 The Arctic

In this study, the data analysis is limited to the Arctic Ocean north of 70°N. Figure 1 shows the International Bathymetric Chart of the Arctic Ocean (IBCAO) compiled by Jakobsson et al. (2008). It maps the deep Canadian, Makarov, Amundsen and Nansen Basins, which are divided by the Alpha - Mendeleev, Lomonosov and Gakkel ridge systems and surrounded by the shallow continental shelves. The bathymetry is strongly correlated with the gravity anomalies (see section 3.4.1). The surface of the Arctic ocean is covered by sea ice of up to 3 - 4 meter of thickness all year round. Changes in the sea ice extent and thickness are tightly coupled to changes in the atmosphere and ocean. In this section, the basic geophysical mechanisms, e.g. the various sea ice conditions and the main circulation patterns in the Arctic, are described.

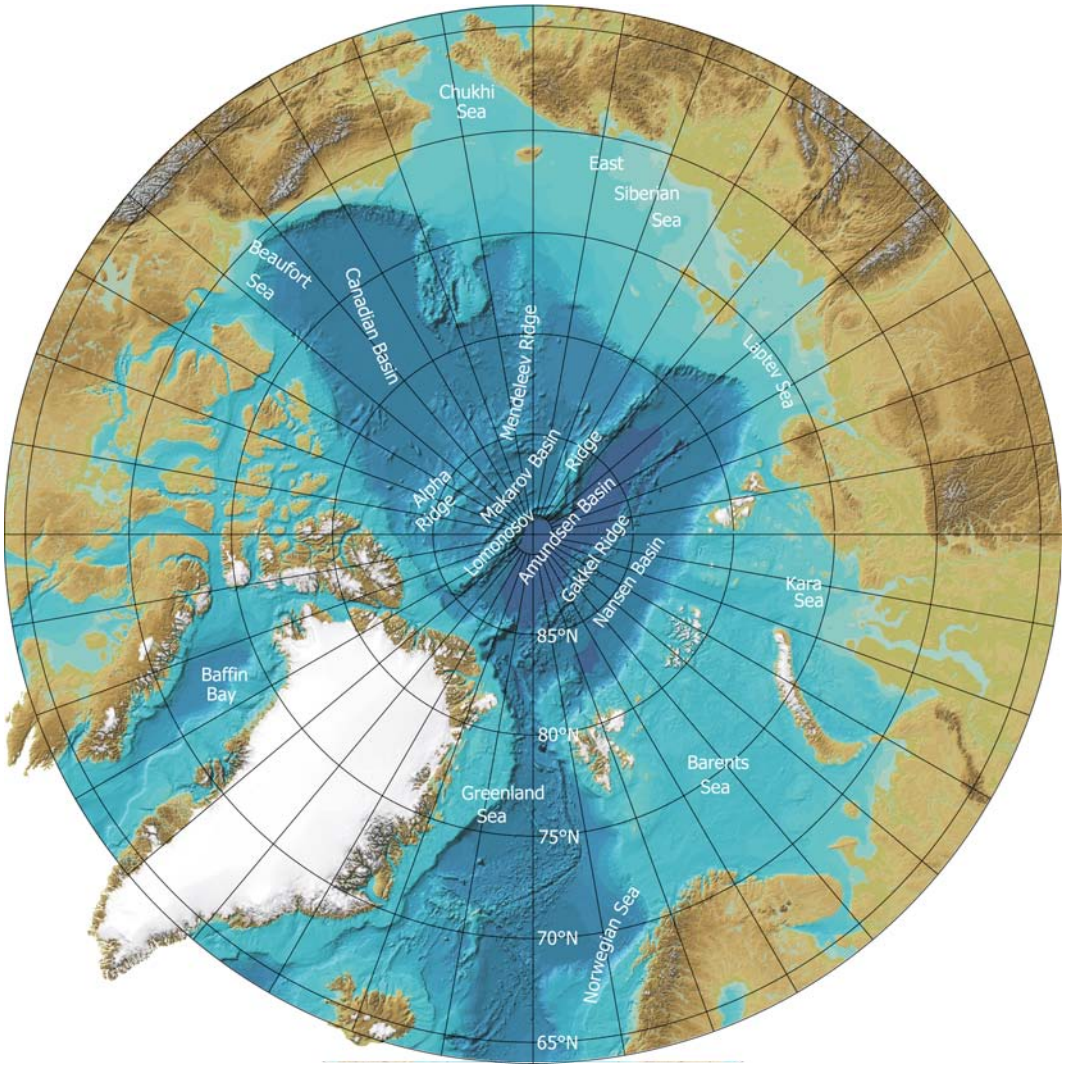

Figure 1: The International Bathymetric Chart of the Arctic Ocean (IBCAO) by Jakobsson et al. (2008).

2.1 Sea ice thickness distribution

The thickness of sea ice is determined by a combination of thermodynamic processes (growth and melt), snowloading and dynamic forcing (ocean and wind circulation), which are described in more detail below.

2.1.1 Thermodynamic growth

In the Arctic, the main sea ice type present all year is multiyear ice, which is defined to have survived more than one summer's melt. The thickness of multiyear ice is about 3 - 4 meters. Also present are thinner ice types (new ice, young ice and first year ice) depending on time of year. In table 1 are listed the definitions of the sea ice thickness or stage of development as formulated by the World Meteorological Organization (1970).

First year ice starts to form in the marginal seas at the end of September or beginning of October. In the fall, the ice grows rapidly and reaches a maximum thickness of 1.5 - 2 m within a single season by thermodynamic growth alone. Most of the first year ice and thinner ice classes melt completely during the melt season (typically May - September). However, a small fraction survives the summer and forms part of the following winters cover of multiyear ice. Compared to first year ice, multiyear ice has a much smaller annual growth cycle of 40 - 45 cm (Maykut and Untersteiner, 1971).

Ice Type	Thickness		Comments
New ice	0 - 10	cm	
Young ice	10 - 30	cm	
First year ice	30 - 200	cm	Sea ice of not more than one winter's growth
Multiyear ice	> 2	m	Sea ice having survived at least one summer's melt

Table 1: Definition of the sea ice thicknesses or stages of development (World Meteorological Organization , 1970).

2.1.2 Dynamics - Redistribution

The Arctic is a dynamic region where the ice is influenced by winds and currents. This dynamic environment causes the ice to become thicker or thinner than it would be in the case of thermodynamic processes alone.

In divergent areas the ice is spreading, leaving cracks and leads of open water, which refreeze rapidly at subzero temperatures. A typical lead dimension is from a few meters to many kilometers wide and from a few meters to several hundred kilometers long (Lindsay and Rothrock, 1995). The thickness of the ice covering a refrozen lead is thinner than the surrounding ice and depends on air temperature and days since freeze up. In convergent areas the sea ice is pushed together and thickened by *rafting* and *ridging* processes (Babko et al., 2002). *Rafting* typically occurs where thinner ice floes (less than 1 meter) override each other. *Ridges* form where ice is crushed into pieces and piled up on top of each other. Ridges are typically formed of first year ice along the edges of multiyear ice and reach a meter or more above and many meters below the surrounding ice. In shear zones, e.g. where landfast ice meets the drifting sea ice, ice ridges cover large areas addressed as *rubble fields*.

The general Arctic circulation pattern (see section 2.5) favours geographic variations with thicker ice north of Greenland pushed up against the coast of Greenland and north-eastern Canada by the Transpolar Drift and Beaufort Gyre. The draft, defined as the part of the sea ice below the sea surface, varies from 2.2 m near Alaska to just over 4 m near Ellesmere Island (Rothrock et al., 2008).

2.1.3 Snow loading

Snow information in the Arctic is relatively sparse and limited to a few studies based on field work conducted in the 1960's, see Maykut and Untersteiner (1971) and Warren et al. (1999).

The mean annual snow load in the Arctic is approximately 35 cm, accumulated during September to end of May. Snow accumulates rapidly in late September and October, followed by a seasonal stable period from November to January with little accumulation and a moderate accumulation from February to May. Snow ablation starts mid-June and ends in late June, leaving the ice mostly free of snow during August.

The large scale variability in snow depth is primarily dependent on the ice thickness. Multiyear ice will carry the full snow load, while first year ice will only bear part of the load depending on the time at which growth started, which is typically in the beginning of October after the heavy snowfalls in September (Wadhams et al., 1992).

Locally, snow depths show large spatial variability in response to wind and topographic variations. The snow tends to pile up behind ridges, leaving drifts as deep as 1 meter, whereas other areas are left bare of snow.

Annual changes in multiyear ice thicknesses are primarily due to changes in snow depths. From late October to late February snow depth accounts for $\sim 90\%$ of the increase in multiyear sea ice freeboard heights (Kwok et al., 2007).

2.2 Interseasonal ice extent

The ice concentration is defined by the World Meteorological Organization (1970) to be the sea surface covered by ice, as a fraction of the whole area being considered, expressed in ratios of tenths. Ice extent is defined as the area of the ocean with a fractional ice cover (i.e. an ice concentration) of at least 15% (Serreze et al., 2007).

In the Arctic, the total sea ice extent reaches a maximum in March and thereby marks the end of the growth period and the start of the melt season. At the end of the melt season in September the sea ice cover reaches a minimum extent. Perennial ice is the ice cover that remains during minimum ice extent and consists mainly of thick multiyear ice floes. During the beginning of freeze up in late September and October, seasonal ice grows rapidly both in thickness and extent. Together, the perennial and seasonal ice constitute the total Arctic sea ice cover.

The ice extent has been monitored by passive microwave since the beginning of the satellite era in 1979. Figure 2 shows the total sea ice extent averaged over the years 1979 - 2000 at its maximum of about 16 million km^2 in March and minimum of 7 million km^2 in September (Serreze et al., 2007).

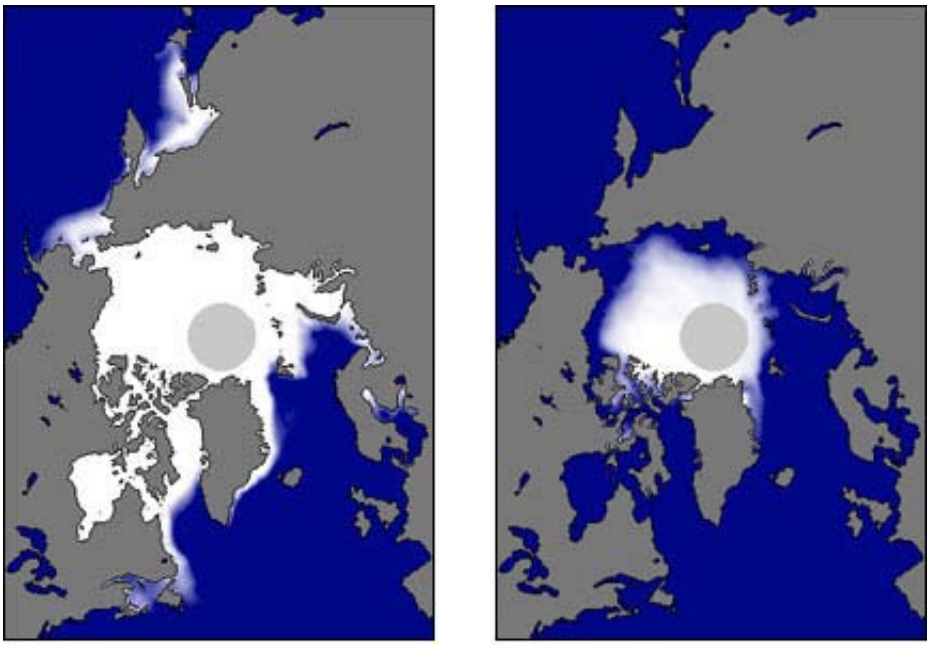

(a) Maximum extent, March (b) Minimum extent, September

Figure 2: Total ice extent averaged through 1979 to 2000. By courtesy of National Snow and Ice Data Center, Boulder, CO.

2.3 Long term trends

The interannual changes of the sea ice extent and thickness are highly variable, depending on the thermodynamic and dynamic state of the Arctic region at a given time.

2.3.1 Total ice extent

In general the linear trends in the total Arctic sea ice extent over the period 1979 - 2007 show a decrease in every month (Serreze et al., 2007) with this pattern being especially pronounced in the late summer and early fall.

Figure 3 shows this trend for March and September. The decrease in ice extent is 2.8% per decade in March, which is low compared to the 11.1% decrease per decade in the September ice extent (Richter-Menge et al., 2008). Figure 3 also shows the interannual variability. The September minimum in 2007 was extremely low covering ~ 4.2 million km^2, which is 36% lower than the longterm average (Comiso et al., 2008). The retreat has been particularly pronounced north of Alaska (Beaufort Sea) and the eastern Siberian Seas (Chukchi, Laptev and Kara Seas). The unusually low Arctic sea ice coverage during the summer of 2007 was caused by anomalously high temperatures and southerly winds (Comiso et al., 2008). There have been a recovery of the minimum ice extent in September 2008 and 2009, but the values are still more than 20% below the longterm average and less than previous observed minimum in 2005 (credit: National Snow and Ice Data Center, September 17, 2009).

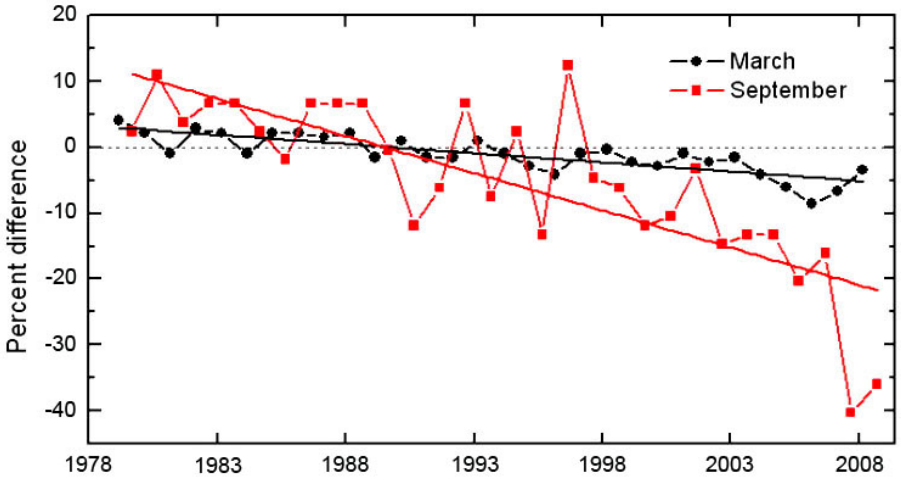

Figure 3: Trend in total sea ice extent for March and September 1979 - 2008 (Richter-Menge et al., 2008).

2.3.2 Variations in thickness distributions

The distribution of sea ice thickness has also changed towards thinner sea ice. Part of this can be explained by the redistribution of the perennial and seasonal ice cover, where a decrease in partial coverage of perennial sea ice and a coincident increase in seasonal ice cover results in a shift in the thickness distribution towards thinner ice. In addition, the thicknesses of multiyear and first year ice have decreased, as concluded from submarine measurements by upward looking sonar (ULS) and thickness measurements by use of electromagnetic induction (EM).

Redistribution of perennial and seasonal ice coverage

The difference between seasonal and perennial sea ice can be detected by active microwave measurements from their distinctive backscatter signatures, where a high backscatter coefficient is correlated with perennial sea ice. These differences are based on the physical characteristics in salinity, porosity, layering and surface properties of the different ice types (Kwok et al., 1999).

At the beginning of January 60% of the total ice extent in the Arctic basin is covered by perennial sea ice (averaged through 1999 - 2003) (Kwok, 2004). The coverage of perennial ice decreases by the beginning of May to 55%, primarily due to an accelaration in the transport of multiyear sea ice through the Fram Strait (see section 2.5) and to a less extent by changes due to rafting and ridging.

The interannual trend of winter perennial ice extent has been decreasing since the 1970s, with an significant acceleration during this decade (Nghiem et al., 2007). The longterm (1979 - 2007) rate of the shrinking perennial ice cover is estimated to be 10.2% per decade by Comiso et al. (2008). However, recent interannual rates have by far exceeded this trend. Nghiem et al. (2006) and Nghiem et al. (2007) found a yearly winter decrease of about 10 - 14% between 2004 and 2007 with the most profound changes in the eastern Arctic Ocean. The total ice cover during winter has been relatively stable over the past nine years (Nghiem and Neumann, 2009), see figure 3, indicating that most of the extent lost by

perennial ice was replaced by seasonal ice. The perennial ice extent in March 2008 was reported to be record low by Nghiem and Neumann (2009) and the boundary between perennial ice and seasonal ice crossed the North Pole area leaving the area around the North Pole covered by seasonal ice.

Observations of ice thickness trends

Comparison of submarine data from the 1960s - 1970s to the end of the 1990s shows a decrease by approximately 40% in mean draft from values larger than 3 m to drafts of about 2 m with no sign in a reversal or rebound beyond the data series (Rothrock et al. (2008), Rothrock et al. (2003), Wadhams and Davis (2000), Tucker III and Weatherly (2001) and Rothrock et al. (1999)). This reduction in sea ice drafts is confirmed by Laxon et al. (2003), when comparing submarine measurements to a mean of eight years of sea ice thicknesses (1993 - 2001) derived from ERS-1/2 satellite altimeters. Similarly, the fraction of ice thicker than 4 m has reduced by roughly 50%. The decrease is greater in the central and eastern Arctic than in the Beaufort and Chukchi seas, with no similar trend found for the North Pole area.

More recent measurements made with a helicopter towed electromagnetic (HEM) device extend these thickness trends to 2007 and confirm the continuation of a reduction in thickness. Haas et al. (2008) reports recent changes in modal thickness[1] in the region of the North Pole by up to 53% (from 1.9 m to 0.9 m) between September 2001 and 2007. The dramatic thinning is mainly due to a regime shift from predominantly multiyear ice in earlier years to first year ice in 2007 in this region. However, both modal multiyear ice and first year ice thicknesses have decreased in the region of the North Pole by 20% and 28% respectively.

The above analysis states a negative trend in sea ice thicknesses in the Arctic Ocean. However, reliable interpretation of the results are complicated, due to the fact that data are sparsely distributed both in space and time.

2.4 Leads

Leads (open water or thin ice) in the ice cover are very important in this study, as they are used as reference for the local sea surface height. Open and refrozen leads occupy only a small fraction of the total ice cover, but this varies with season and ice conditions. Thus, the lead fraction observed from submarine measurements (Wadhams and Horne, 1980) are as high as 20% in late summer (September), decrasing to 10% due to the rapid thermodynamic growth of thinner ice in the freeze up season (October) and further decreasing to 3% by April. This is in agreement with estimates from 1 year (1989) infrared satellite imagery (Lindsay and Rothrock, 1995) showing a reduction in lead area from 33% in September to 13% in October and further to between 5% and 7% from January to April. In general, the lead fraction of the perennial ice cover in winter is less when compared to the winter seasonal ice cover. In summer the method based on infrared imagery is inaccurate especially in the seasonal ice cover.

[1]Modal thickness it the most frequent ice draft found in the thickness distribution. For HEM measurements this is the most reliable parameter, as the HEM system underestimates keels of ridges by up to 50%

2.5 Circulation systems

The circulation of the sea ice cover and ocean surface layer are primarily wind-driven and closely coupled.

Figure 4 shows the circulation pattern in the Arctic Ocean. The circulation of the upper ocean layer is obtained from the drift of ice camps, ships and buoys, as well as from geostrophic calculations from oceanographic measurements of the water-density distribution. The surface circulation pattern is dominated by the anticyclonic *Beaufort Gyre* (BG) in the Canadian Basin and a weaker cyclonic circulation in the Eurasian basin separated by the *Transpolar Drift* (TD). Normally, the drift of the sea ice follow these currents.

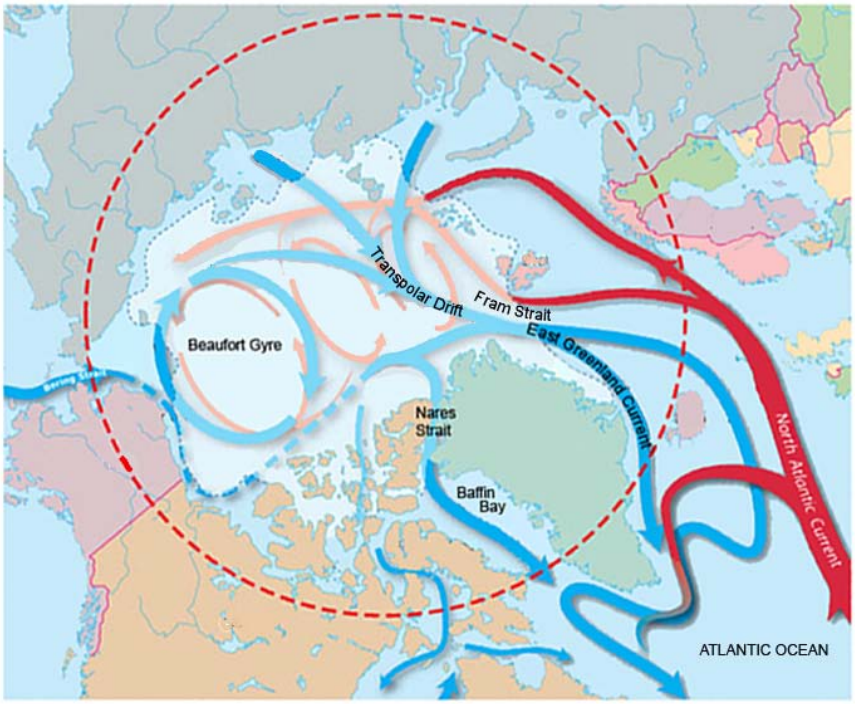

Figure 4: Map of the circulation patterns in the Arctic Ocean (Credit: Woods Hole Oceanographic Institution, September 2009).

The largest export of multiyear sea ice from the Arctic Ocean is through the Fram Strait. The ice is carried southward in the *East Greenland Current* (EGC) into the Greenland Sea and then to the North Atlantic, where it melts. A small amount enters Baffin Bay through the Nares Strait and the various straits in the Canadian Archipelago (see figure 4).

2.5.1 The Arctic Oscillation index

The strength and location of BG and TD are largely controlled by wind patterns and hence changes in atmospheric pressure. Variability in the arctic system can be described by the

Arctic Oscillation (AO) index (Rigor et al., 2002), which defines the differences in pressure between the central Arctic and the pressure at mid-latitudes ($\sim 45^{\circ}$N). Changes in the AO index forces changes in sea ice motion, which again changes the sea ice concentration and thickness. A schematic presentation of the surface circulation of the Arctic Ocean under positive and negative AO states are plotted to the left in figure 5.

A positive AO index is associated with lower than normal sea level pressure over the central Arctic and higher than normal pressure at mid-latitudes. This pressure pattern results in cyclonic winds in the Arctic Ocean, causing the anticyclonic circulation of the BG to slow down. The TD becomes more pronounced and moves towards the North Pole under these conditions. The change in circulation increases the export of sea ice through the Fram Strait and opens up the ice cover in the Arctic Ocean, leaving cracks and leads as well as the presence of younger and thinner sea ice. With very high positive AO (larger than 2), the circulation of the BG can become cyclonic (Rigor et al., 2002).

A negative AO index is associated with a higher than normal atmospheric sea level pressure in the Arctic and lower than normal pressure at mid-latitudes causing prevalence of anticyclonic winds. Under these conditions the clockwise circulation of the BG is relatively strong and tends to recirculate the ice longer ($\sim$ 6 years for negative AO index and $\sim$ 3 years for postive AO index (Steele et al., 2004)) in the Arctic Ocean before being exported through the Fram Strait. Thus, a negative AO index favors thicker ice.

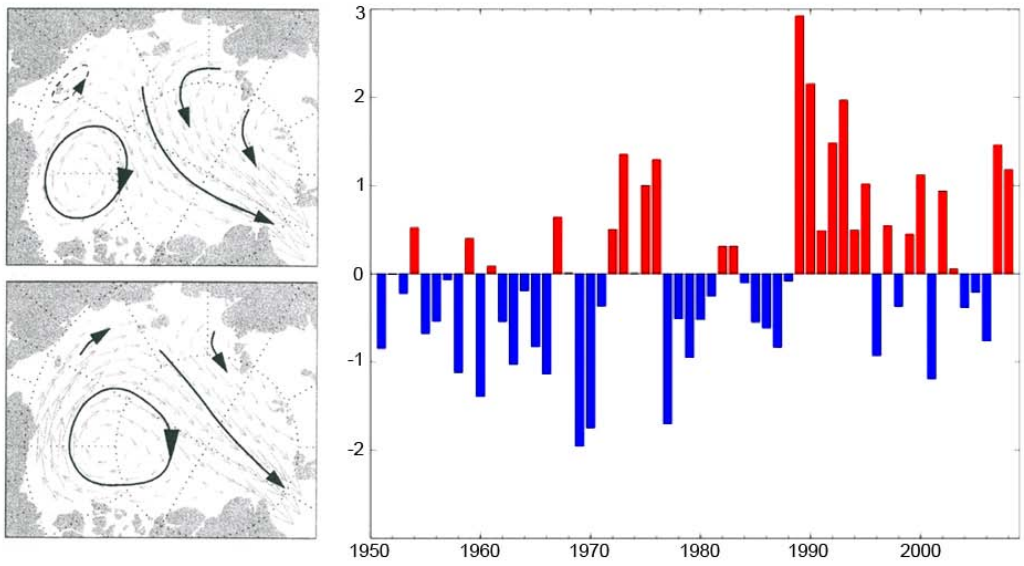

Figure 5: Sea ice motion for positive AO index (upper plot) and negative AO index (lower plot) from Rigor et al. (2002). On the right the extended winter (DJFM) AO index from 1950 to 2008 is shown (Overland et al., 2008).

In Figure 5 (right) the winter AO index from 1950 - 2008 is plotted. The Arctic Oscillation index fluctuates between the cyclonic (positive AO) and anticyclonic (negative AO) state. High positive AO indicies dominated in the period 1989 - 1996, and are correlated with the decreasing ice cover. This period is followed by a period, 1997 - 2006, characterized by an anticyclonic atmospheric circulation, which is consistent with an AO index fluctuating about zero (Proshutinsky et al., 2008). During, 2007 - 2008, the AO index returns to

positive values, but with lower values than in the 1990s. The ice extent of the summer 2007 and 2008 was characterized by anomalously low values, which is expected at positive AO index due to the acceleration of the Transpolar Drift. The french sailing vessel Tara drifted across the Arctic in the Transpolar Drift during September 2006 - December 2007. This is three times as fast as Nansen's drift in 1893 - 1896 (Gascard et al., 2008) and confirms an acceleration of the TD.

Changes in the atmospheric circulation system have been associated with changes in the sea surface temperature, as well as a redistribution of the heat transport into the Arctic from the warm Atlantic and Pacific waters. These mechanisms are described below.

Heating by radiation

The surface air temperature has increased in the Arctic since the mid-1960s (Overland et al., 2008). Anomalously high temperatures in winter can limit ice growth and warmer temperatures in spring and summer can accelerate melt. This mechanism is more pronounced in years of high AO index, where the sea ice concentration is low and more solar radiation is absorbed by the upper ocean resulting in more bottom melt of the sea ice. The bare ice reflects 65% and snow covered ice 85%, whereas open water reflects only 7% of the incident solar radiation (Perovich et al., 2002). Steele et al. (2008) observed cooling of the sea surface temperature (SST) at negative AO and heating at positive AO.

Furthermore, an ice cover thinned by excessive bottom melt transmits more solar radiation directly to the ocean than the original thicker ice cover (Perovich et al., 2008). Warm anomalies of the SST were observed by Steele et al. (2008) in 2002 - 2005 and 2007, where the 2007 summer anomaly was extreme with an increase in SST by up to 5°C. This anomaly was explained by the thinner ice cover in combination with more extensive areas of open water, which caused large bottom melt (more than six times the annual average) in the Beaufort Sea (Perovich et al., 2008).

Heating by transport

Advection of heat in the ocean from the north Atlantic and Pacific influences the sea ice cover in the Arctic Ocean (Zhang et al., 1998). The warm saline Atlantic water enters the Arctic Ocean through eastern Fram Strait and the Barents Sea and forms an intermediate layer at 150 - 800 m depth, as it subducts below colder less dense Arctic surface waters. In the Canadian Basin the primary oceanic heat source to the sea ice cover is the Pacific water, which enters the Arctic Ocean through the Bering Strait and is located at about 40 - 150 m depth. The Pacific water is characterized by being less saline and colder than the Atlantic water.

A high positive AO index increases the inflow of the Atlantic water into the Barents Sea and the outflow of Arctic water through the Fram Strait, resulting in a stronger East Greenland Current (Zhang et al., 1998). This redistribution of ocean masses weakens the cold upper Arctic Ocean layer, that isolates the ice cover from the warm Atlantic water causing larger bottom melt of the sea ice (Steele and Boyd, 1998). Accordingly, the location of the front between halocline waters of Atlantic and Pacific origin changes with the AO index (Steele et al., 2004). In years with negative AO index, the front follows the Lomonosov ridge and moves counter clockwise to a position roughly parallel with 0°-180° longitude in years of positive AO index.

During the period 1989 - 1996 of high AO index, the Atlantic water has been traced by oceanographic measurements all the way to the North Pole area and the Makarov Basin, where an increase in salinity (2 psu) and temperature (1 - 2°C) has been detected by Morison et al. (2006). In 2005 the temperature and salinity of the ocean in the North Pole

region and Makarov Basin returned to the values observed pre 1990s, and the observed salinities were consistent with the salinities of the Pacific water in the Canadian Basin (Morison et al., 2006). It was concluded that the redistribution of the intermediate layers, lags the AO index by 3 - 7 years. This could explain, why the sea ice volume kept on shrinking, even though the AO index has been fluctuating about zero since the end of the 1990s. In addition, Shimada et al. (2006) found an increase in temperature of the Pacific water to be correlated with the reduction in the sea ice cover in the Beaufort Sea during the period 1997 - 2003.

3 Satellite altimetry

3.1 Altimetry missions in the Arctic

As described in the introduction four satellite missions have had profound implications for the investigation of the Arctic Ocean. These are the laser altimeter mission ICESat and the radar altimetry satellites ERS-1/2 and ENVISAT.

The Ice, Cloud and land Elevation Satellite (ICESat) was launched on January 12, 2003, into a polar orbit covering the area from 86°N to 86°S. ICESat is part of NASA's Earth Observing System (EOS) missions and is specially dedicated to detect height changes of ice sheets and glaciers (Zwally et al., 2002). The Geoscience Laser Altimeter System (GLAS), carried onboard the satellite, consists of three identical lasers operating one at a time for continuous mapping of the Earth's surface. Each laser operates at two different wavelengths, 532 nm (visible green) primarily for cloud detection and 1064 nm (near-infrared) for surface reflections. ICESat's laser footprint diameter is ∼65 m in diameter on the Earth's surface. Each shot is separated by an along track spacing of 172 m center-to-center, determined by the orbit velocity and 40 Hz laser pulserate. The nominal precision for surface elevations are estimated to be better than 15 cm (Zwally et al., 2002).

ENVISAT was launched on February 28, 2002, as follow up on the ERS-1/2 satellites. The two ERS satellites each carries a radar altimeter (RA-1) and ENVISAT carries the improved radar altimeter (RA-2). The RA-2 (Resti et al., 1999) has a higher pulse repetition frequency (1800 Hz) than RA-1 (1020 Hz). Both radar altimeters operate in the ku-band (12.5 - 18 GHz), for RA-2 the frequency is 13.575 GHz corresponding to a wavelength of 2.2 cm. RA-2 transmits pulses every 557 μsec (corresponding to 1800 Hz). Averaging of 100 individual pulse waveforms results in an integrated footprint smeared in the along-track direction and corresponds to a resolution of approximately 390 m. The geometric resolution (cross-track) is represented by a nominal footprint area in the order of 2 - 10 km.

In the following subsections the basic principles of laser and radar satellite altimetry are given. The theory for radar altimetry are based on the characteristics of ku-band radars.

3.2 Basic measurement principles

The basic principles of altimetry is very simple. The altimeter transmits an electromagnetic pulse and measures the time it takes for the pulse to reach the Earth's surface at nadir and return to the altimeter. As electromagnetic waves travel with the speed of light (c) in vacuum, the distance from the satellite to the surface (R_0) is, to a first approximation, given by:

$$R_0 = c\,(t_0/2) \tag{3}$$

where t_0 is the two-way travel time measured by the altimeter. The range R_0 has to be corrected for instrument errors and atmospheric refraction (R_i) in order to obtain the true range (R):

$$R = R_0 - \sum_i R_i \tag{4}$$

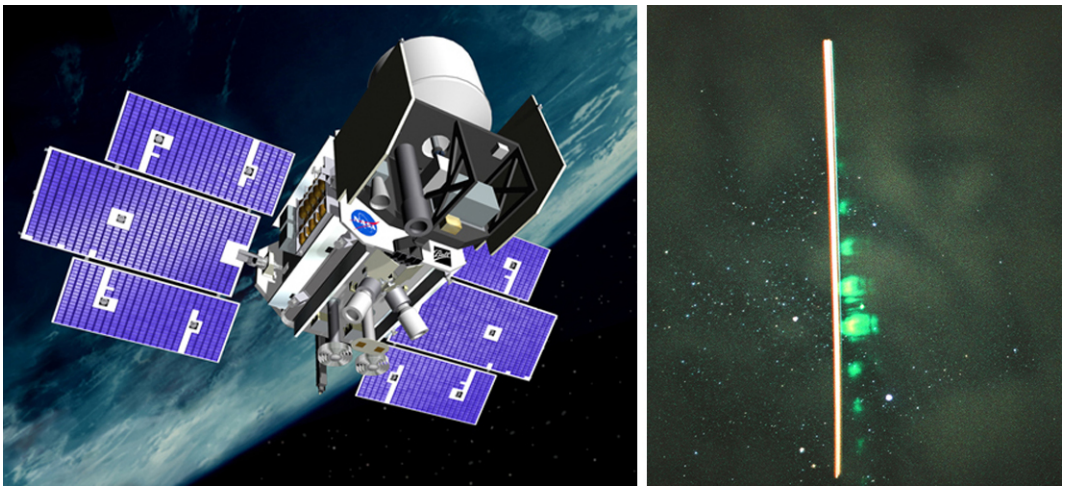

Figure 6: ICESat satellite (left) and laser spots from green laser pulse (right). Photos by courtesy of NASA.

An outline of the various correction terms is given in figure 7 and a more detailed description on this topic can be found in Fu and Cazenave (2001).

The elevation of the surface observed at nadir above a reference ellipsoid[2], known as the ellipsoidal height (h) is given by:

$$h = H - R \tag{5}$$

where H is the altitude (or orbital distance) of the satellite above the reference ellipsoid.

The altitude (H) is determined by *precise orbit determination* (POD) and for narrow beam altimeters (e.g. lasers), where off-nadir pointing becomes an issue by *precise attitude determination* (PAD). Today the orbits and attitude are determined with very high precision by various techniques combining instrument measurements with high quality post-processing. For ICESat an onboard GPS system measures the post-processed orbit to better than 5 cm and a star camera in combination with gyroscopes estimate the attitude $\sim$ 7.5 cm radial (Zwally et al., 2002). ENVISAT on the other hand only needs POD for estimation of the altitude, as the pulse-limited type radar altimeter is independent of attitude (see chapter 3.3). The ENVISAT orbit is determined with $\sim$ 3 cm accuracy (Resti et al., 1999) from ground to satellite measurements by use of *doppler orbitography and radiopositioning integrated by satellite* (DORIS).

In the Arctic Ocean, the altimeter measures the height of the sea ice cover. By combining equation 1 and 2, the ellipsoidal height (h) is given as the sum of sea ice freeboard (h_f) and sea surface height (h_{ssh}):

$$h = h_f + h_{ssh} = h_f + (h_{geoid} + h_{DT} + h_{IB} + h_{tides} + h_{errors}) \tag{6}$$

where the sea surface height (h_{ssh}) is comprised of contributions from the geoid (h_{geoid}), dynamic topography (h_{DT}) associated with large scale ocean circulation, inverse

[2]The reference ellipsoid is defined as the ellipsoidal surface approximating the mean sea level

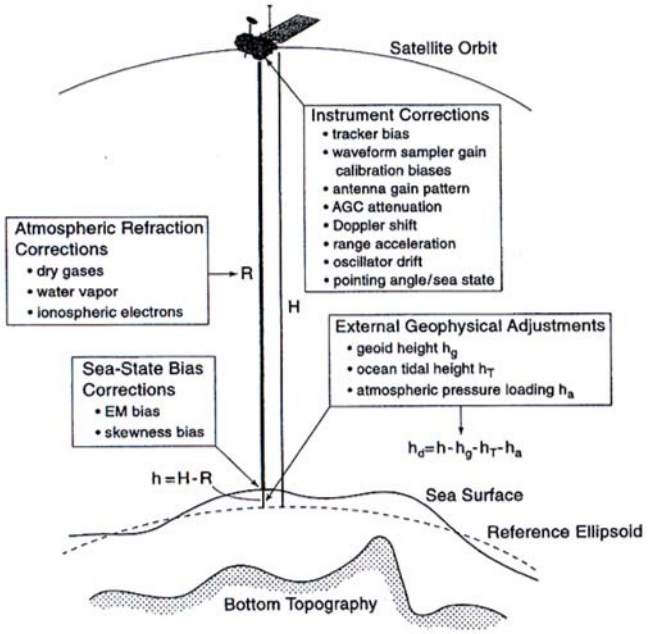

Figure 7: Definition of heights and corrections relevant to satellite altimetry over open ocean (Fu and Cazenave, 2001).

barometric effect caused by atmospheric loading (h_{IB}), tides (h_{tides}) and height corrections from instrument and model inaccuracies (h_{errors}). The dynamic range of the geoid are two orders of magnitude larger than the variations in freeboard heights, dynamic topography, atmospheric pressure loading and tides. Thus, the sea surface height is dominated by the time-invariant long wavelength geoid variations.

If all the geophysical contributions were known with sub-decimeter accuracy the sea surface height could in principle be modelled and sea ice freeboard heights extracted accordingly. This method, has so far been subject to errors on the same scale as the freeboard heights due to poor models (Kwok et al., 2006). Characteristics and existing Arctic Ocean models of the geophysical height contributions in equation 6 are discussed in more detail in section 3.4.

It is, however, possible to determine a reference for the local sea surface heights in ice covered waters from altimetry based on location of leads (open water or thin ice) in the ice cover. The methods used for lead detection are different for radar and laser altimetry and both methods are discussed in the next section.

3.3 Determination of sea surface heights over ice covered waters

Physically, the altimeter measures the strength and shape of the return signal from which the two-way travel time can be extracted. The shape of the return signal from one pulse as a function of time is called the waveform. It is to a large extent defined by the

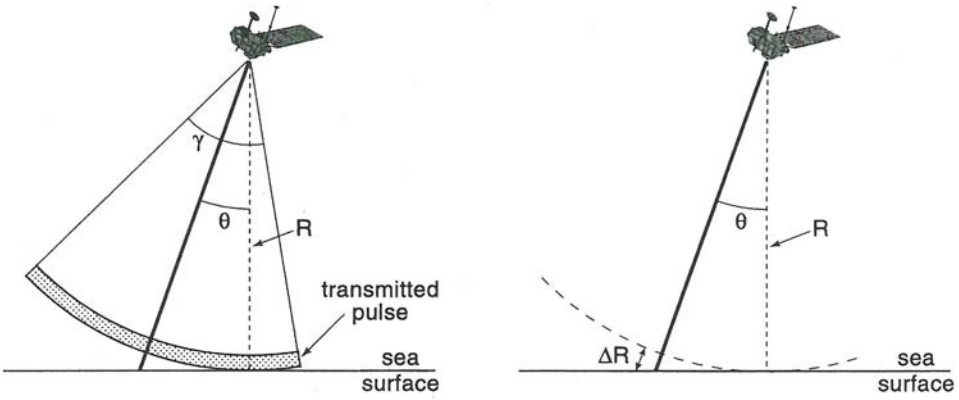

Figure 8: Measurement geometry for a pulse-limited radar altimeter (left) and a narrow beam-limited laser altimeter (right). In both cases the boresight of the antenna views the surface at off-nadir angle (θ), but only the range measured by the beam-limited altimeter is sensitive to the off-nadir pointing by Δ R (Fu and Cazenave, 2001).

characteristics of the footprint area[3], but also the transmitted pulse shape, the surface height and reflectivity distribution within the footprint, forward scattering in the atmosphere (clouds and aerosols) and the receiver characteristics.

Radar and laser altimeters have different beam and footprint geometries (see figure 8) and as a consequence they show large differences in waveforms. Conventional radar altimeters have a broad beam width (larger than 10^{-2} rad), resulting in a large footprint area (in the order of 2 - 10 km nominally for ENVISAT and ERS-1/2). At this scale, the footprint area is much wider than most of the open leads in the Arctic, but the waveforms dependency on surface roughness can be used to identify returns from leads, see section 3.3.1. Lasers are in general characterized by a very narrow beam width, resulting in a relative small footprint area ($\sim$ 65 meter in diameter for ICESat) and is believed to better detect the larger open leads directly by relative changes in the elevation, see section 3.3.2.

3.3.1 Radar altimetry

Normal incidence radar reflection strongly depends on the surface roughness on scales similar to the wavelength of the operating radar (ERS-1/2 and ENVISAT operate at wavelength 2.2 cm).

Radar altimeter waveforms scattered from a rough surface are highly assymmetrical and characterized by a low backscatter coefficient at nadir with a slowly trailing edge, see figure 9 (left). In the case of a flat smooth surface the radar returns are characterized by large nadir peak power followed by a rapid fall-of, see figure 9 (right). The Rayleigh criterion (see for example Ulaby et al. (1982) chapter 11 - 2), which is dependent on the radar wavelength and angle of incidence, must apply for a surface to be considered smooth. As an example, a radar operating at wavelength 2.2 cm at normal incidence, fulfils the criteria if the surface roughness[4] are less than 3 mm througout the footprint (Fetterer et al., 1992). Most naturally occuring surfaces are not smooth on the milimeter

[3]The footprint area is defined as the area illuminated by the altimeter at the Earth's surface at a given time
[4]The surface roughness is here defined in terms of the standard deviation of the surface height variation

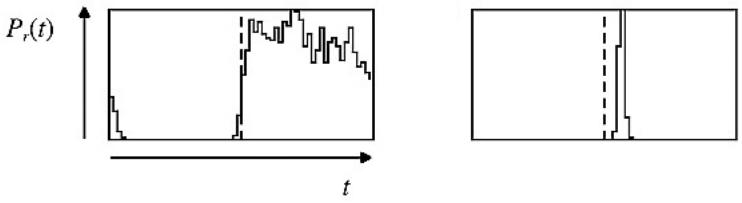

Figure 9: Diffuse waveform from a rough surface (left) and specular waveform from a smooth surface (right) from Peacock and Laxon (2004). The waveforms are given as reflected power (P_r) as a function of time (t).

scales, at least not for very large areas, however, Drinkwater (1991) has shown that if only a small fraction (less than 1%) of the surface originate from coherent reflections, they can dominate the return echo entirely. In the following, radar returns from rough surfaces are termed diffuse and returns from flat surfaces are termed specular. The peak power of specular returns can be up to 3 orders of magnitude greater than that for diffuse waveforms, thus the waveforms presented in the figure are not to scale.

Typical waveforms over open ocean are of the diffuse type with a peak power at about 8 - 15 dB (Chelton and McGabe, 1985). As the sea surface characteristics, e.g. heights and reflectivity, are slowly varying from successive radar returns, the waveforms are very similar in shape. To the contrary, waveforms over sea ice exhibit large fluctuations from one waveform to another, both in shape and peak power, reflecting the large variations in ice types and settings. This was first reported by Ulander (1987), Ulander and Carlström (1991) and Laxon (1994a). Over sea ice covered waters both waveforms of specular (or quasi-specular) and diffuse scattering are observed.

The likely source of specular echoes in sea ice reflections are from calm water or new ice between floes (Drinkwater, 1991). These surfaces contribute as plane surfaces, which has a higher reflection coefficient than most snow covered sea ice surfaces. The reflection coefficient for water is typically 11 dB higher than for most snow covered sea ice surfaces (Drinkwater, 1991). Many scientists have contributed to the study of the specular signals. To mention a few, Ulander and Carlström (1991) have registered high backscatter over new and young ice in between 15 - 40 dB and Ulander (1987) has registered 12 - 40 dB in peak power over new ice.

Diffuse waveforms with peak power comparable to those of open water have been observed and investigated by Laxon (1994b) and Drinkwater (1991). By comparing altimeter data to additional remote sensing products (infrared AVHRR images and aerial photography), they have found the diffuse waveforms to originate from fast ice and vast floes, where the altimeter footprint is entirely filled with consolidated ice. The diffuse return is a consequence of the less reflective and rougher sea ice floe surface. Ulander (1987) estimated the peak power to be 12 - 30 dB for multiyear ice.

The above information can be used to discriminate between reflections from local sea surface heights (specular returns) and from ice covered surfaces (diffuse returns). Many scientists have proposed and used different criterias to distinguish specular waveforms from diffuse, either to mask out the sea ice or to find the returns from sea ice surfaces (see appendix E.1). The procedure to estimate sea surface elevations in the ice pack is hampered by large biases, as the specular echoes from smooth water or refrozen leads

tend to dominate the signal even if it is off-nadir by several (1 - 10) kilometers. This phenomenon, known as snagging, occurs in areas of mixed small floes and leads, or where the radar reflective surface becomes inhomogenuous on the scale of the altimeter footprint. Due to snagging events, estimation of a local reference sea surface demands careful processing and retracking of data. When neither ice nor water dominates the radar return it results in a distorted echo shape and data are rejected.

3.3.2 Laser altimetry

Laser altimetry waveforms are nearly Gaussian distributed for most surface reflections in absence of forward scattering (Brenner et al., 2003) and do not show the same distinct differences between leads and consolidated ice as obtained by radar altimetry. Typical waveforms from level first- and multiyear ice floes covered with snow are shown in figure 10 (a) and 10 (b), respectively. Thus, there is some degree of variation in waveforms depending on the surface height distribution and reflectivity properties within the footprint.

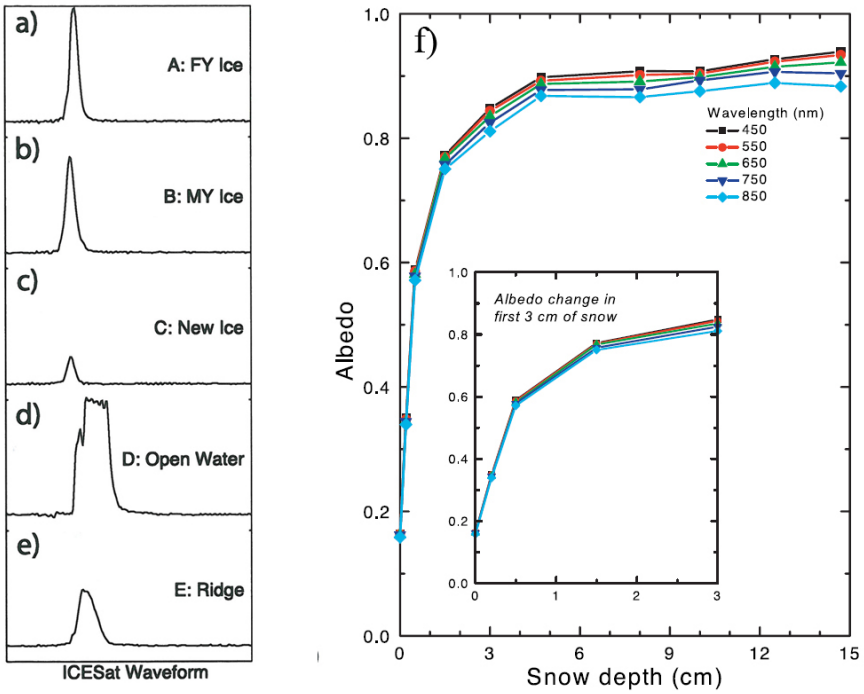

Figure 10: ICESat waveforms (a - e) and albedo of snow (f) given for five different wavelengths in the visual spectrum (Kwok et al., 2006).

Large height variations within the footprint, caused for example by ridges, hummocks and ice rafts, tend to broaden the waveforms, see figure 10 (e). An estimate of the height variations is determined by the root-mean-square (rms) width of the Gaussian fit of the return waveform (for a defintion of the retracking procedure see section 3.3.3). Unfortunately, sloping surfaces and forward scattering in the atmosphere, also result in broadening of the waveform and the various contributions can not be separated

independently based only on the width of the waveform. Knowledge on the surface characteristics and the atmospheric conditions are necessary in order to solve the problem. Most sea ice covered surfaces can be regarded as nearly horizontal and the slope can be neglected. Further, if forward scattering in the atmosphere is negligible, the width of the waveform is a statistical estimate of the surface height distribution within the footprint, representing its deviation from a smooth reference surface.

The reflectivity (R) is calculated as the ratio of the received energy, after it has been scaled for range and the transmitted energy. The reflectivity is highly dependent on the surface albedo, such that a high albedo results in a high reflectivity.

In terms of laser returns in the visual and near-infrared spectrum, smooth open water, e.g. a newly opened lead, acts as a specular (non-diffuse) reflector and tends to saturate the waveform. Figure 10 (d) shows a saturated waveform from open water, where the top of the waveform is truncated leading to unphysical reflectivities ($R > 1$). The returns from open water are very important as they provide the user with the unbiased height of the local sea surface for reference. Unfortunately, the ICESat tracking procedure underestimates the elevations of the saturated waveforms by unrealistic high biases (more than 1 meter) and these have to be filtered out, see chapter 4.1.2. The fractional coverage of the specular saturated waveforms are found to be larger in the fall than the winter periods (Kwok et al., 2006), in accordance with the larger fractional coverage of leads in the fall (see section 2.4).

Most sea ice is covered by a snow layer, unless it is newly formed ice or bare ice where the snow was removed by the wind. Lasers in the visual and near-infrared spectrum is reflected by the snow surface (see section 3.5) and thus the return signal is mostly defined by the snow properties. Figure 10 (f) shows the evolution of the albedo with increasing snow depth for a few wavelengths in the visual spectrum. At snow depths deeper than 3 cm the albedos are almost constant and explains the almost identical waveforms from first- and multiyear sea ice.

Sea ice has a lower albedo than snow and becomes dominant for snow depths less than 3 cm. This property has proven to be an indicator of newly refrozen leads in ICESat profiles. An extensive analysis of coincident SAR images and ICESat measurements made by Kwok et al. (2006) and Kwok et al. (2004) show, that thin ice-filled leads with no snow on top do have a lower reflectivity, when compared to thicker snow covered ice, as seen in figure 10 (f). It takes only 1 - 2 cm snow cover to remove the low value in reflectivity, corresponding to few days (2 - 3) after opening of the lead. ICESat waveforms of thin ice look like level ice floes of thicker ice but with lower reflectivity, see figure 10 (c). The analysis finds the low reflectivities to be coincident with a relative minimum in ICESat elevations and it is concluded that simultaneous dips in elevation and reflectivity are an indication of ice types thinner than 10 cm.

The above also indicate that ICESat directly detect leads as lower elevation values taken relative to the surrounding heights from thicker ice, as expected from the narrow footprint area. There is a possibility that some thin ice covered leads might be masked out by the constraint on low reflectivity and thus selection of minimum values in elevation could potentially provide the information needed to detect leads.

3.3.3 Tracking procedure

Different tracking procedures are used to estimate the range, depending on the shape of the waveform.

The assymetric radar altimetry waveforms reflected from a diffuse sea ice surface, are best retracked by the Offset Centre of Gravity (OCOG) retracking scheme and a Gaussian function is best fitted to the peaked signals from smooth ice surfaces (Peacock and Laxon, 2004).

For ICESat the elevation over sea ice covered surfaces (or open water) will be represented by the time between the center of the transmitted pulse and the centroid of the Gaussian fitted to the last peak of the received pulse (Brenner et al., 2003), see figure 11. The elevation obtained by this tracking procedure is a mean surface averaged over the footprint area assuming the surface is Lambertian[5]. As snow covered surfaces are nearly Lambertian surfaces this is a realistic assumption.

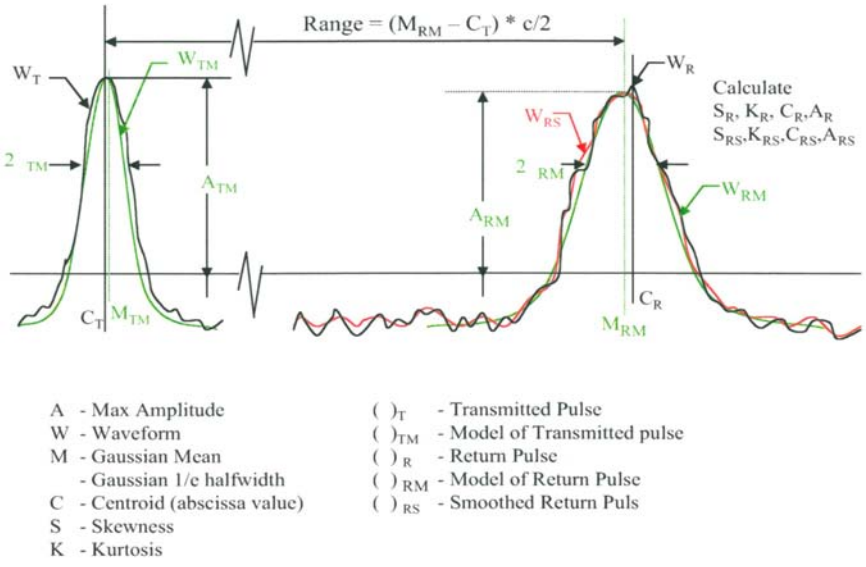

Figure 11: Characterization of transmitted and received pulse waveforms from Brenner et al. (2003) page 40.

[5]A diffuse surface for which the reflectance is constant for any angle of reflection

3.4 Geophysical effects on the sea surface topography

In this section, the various geophysical contributions to the sea surface topography are briefly presented (figure 7 and equation 6). The physics, the expected variabilities and the implications for the Arctic Ocean are described.

3.4.1 Marine geoid undulations

The *marine geoid* is defined as the equipotential surface, which coincides with the sea surface, in the absence of all forces other than the gravity and the centrifugal force. The geoid determined by the spatial variations of the earth's gravity field, is related to the distribution of mass within the Earth and at shorter wavelengths ($\lambda < 250$ km) bathymetry and inhomogenities in the density of the oceanic crust and mantle.

The geoid undulations[6] are by far the largest contribution to the sea surface topography and varies globally from -105 m South of India to 85 m off the north east coast of New Guinea. Low geoid values are related to low subsurface densities, submarine canyons and trenches at the bottom of the sea. High geoid values are accordingly related to high subsurface densities, sea mounts and ocean ridges.

Geoid models over the ocean can be derived from gravity measurements, or more directly from altimetry. The variations in gravity are expressed in mGal (1 mGal = 10^{-5} m/s^2) and 1 mGal changes in gravity corresponds roughly to a change of 15 m bathymetry in the free air anomalies. The short wavelength variations are obtained from terrestrial gravity measurements from e.g. ship, airplane, or submarine. Ocean medium wavelength variations are measured by satellite altimetry (e.g. GeoSat, TOPEX/Poseidon or ERS) and the long wavelength variations from dedicated satellite gravity missions (CHAMP or GRACE).

Altimetry measurements of the sea surface heights can be used to estimate the marine gravity field with rms accuracy 3 - 7 mGal and resolution 10 - 15 km (see for example Sandwell and Smith (1997) or Knudsen et al. (1992)). The sea surface heights, corrected for tides and atmospheric pressure loading, represent the marine geoid, if the dynamic topography is neglected (see equation 6). The marine geoid is inverted to gravity anomalies, e.g. by use of Fast Fourier Techniques (Schwartz et al., 1990). In the sea ice covered Arctic Ocean the sea surface heights from satellite altimetry can be found by using the techniques described in chapter 3.3. First results of gravity anomalies in sea ice covered regions were obtained from ERS-1 radar altimetry data by Laxon and McAdoo (1994) with an accuracy of 8 mGal and half-wavelength resolution of 35 km, which revealed an extinct spreading zone in the Canadian Basin. More recently, Forsberg and Skourup (2005) published gravity anomalies retrieved from ICESat laser altimetry of accuracy 6 mGal, and McAdoo et al. (2008) published a gravity field based on a combination of ICESat and ERS-2 data with 6 mGal rms accuracy and resolution down to 18 km.

3.4.2 Dynamic topography

Variations in the sea surface height due to density changes in the oceans are associated with horizontal pressure gradients. In the *geostrophic approximation* the horizontal pressure gradient force and the Coriolis force are in balance and can be expressed by:

[6] Geoid undulations are the variations of the geoid relative to a reference ellipsoid

$$fv = \frac{1}{\rho_w}\frac{\partial p}{\partial x} \tag{7}$$

$$fu = -\frac{1}{\rho_w}\frac{\partial p}{\partial y} \tag{8}$$

where v and u are the meridional and zonal velocity components, $f = 2\Omega\, sin\varphi$ is the coriolis parameter, Ω = 7,292 $\times 10^{-5}$ s^{-1} the frequency of the earth rotation, φ latitude and ρ_w density of the water.

Assuming *hydrostatic balance*,

$$\frac{dp}{dz} = \rho_w g \tag{9}$$

the horizontal velocities given in equation 7 and 8 are an expression of the slope of the sea surface. In the northern hemisphere, the larger sea surface heights are to the right of the flow direction, and in the southern hemisphere they are to the left.

In the open ocean, the large-scale oceanic flows are nearly in geostrophic balance and the variations in dynamic topography (h_{DT}) are basically an estimate of the general large-scale ocean circulation. Globally, the amplitude of the dynamic topography relative to the geoid is in the order of 2.5 m (Fu and Cazenave, 2001). In the Arctic Ocean the amplitude is about 1 m, with minimum located south of Greenland and maximum in the Canadian Basin caused by the anticyclonic Beaufort Gyre (Forsberg et al., 2007).

Information on the dynamic topography is collected by measurements of density changes from salinity and temperature profiles of the ocean. In addition, various oceanographic models of the dynamic topography exist, but they are very diverse and often the differences in models exceed the signal of the dynamic topography (see section 4.2.2).

Satellite altimeters are also used to measure the dynamic topography. Due to the relatively small amplitudes of the dynamic topography the altimetry measurements of the sea surface height need to be of high precision, and highly accurate geoid models are required. Today the high precision in altimetry measurements are achievable and relatively good geoid models exist. GRACE geoid models are estimated to have an accuracy in the order of 2 - 3 mm at a spatial resolution down to 400 km (Tapley et al., 2004). Thus, it is possible to obtain large-scale ocean circulations on similar scales. For a detailed description of altimetry derived dynamic topography over open ocean, see Fu and Cazenave (2001) section 2.2.

Peacock and Laxon (2004) found only a centimeter level reduction in the quality of altimetry derived sea surface heights, when moving from ice covered to ice free oceans. These residual errors are small enough to make the data useful for geophysical applications. A nearly complete Arctic Ocean mean (1995 - 2005) dynamic topography was developed from a combination of ERS-2 and ICESat mean sea surfaces in combination with a geoid model (Skourup and Forsberg, 2008).

3.4.3 Atmospheric pressure loading

Atmospheric loading exerts a pressure force on the sea surface. As the ocean compressibility is small, the spatial and temporal atmospheric pressure variations are

compensated by changes in the sea surface heights. This response is known as the *inverse barometer effect* (IBE).

To estimate the surface height variations due to atmospheric pressure loading the criteria for hydrostatic balance is used (see equation 9). In addition, assuming the ocean response to variations in atmospheric pressure to be in isostatic equilibrium the height (h_a) corrections originating from the inverse barometer effect is given by:

$$h_a = \frac{1}{\rho_w g}(p_0 - \bar{p}) = \alpha(p_0 - \bar{p}) \tag{10}$$

where g is the standard gravity acceleration (g = 980.6 cm/s^2), ρ_w the density of the ocean, p_0 the atmospheric pressure at sea level and $\bar{p}$ is the global mean pressure of the atmosphere taken at sea level. $\bar{p}$ is 1013.25 mbar for a standard atmosphere. The sea level pressure (p_0) fields are obtained from meteorological models. For a more detailed deduction of equation 10, see for example Fu and Cazenave (2001) section 5.3.

In case of an ideal inverted barometer effect the proportionality constant is set to α = -1 cm/mbar. Using standard density values for the ocean (ρ_w = 1.025 g/cm^3 and α = -0.995 cm/mbar) near-ideal conditions are found. Non-ideal behaviour occurs for example, from the dynamic responce of the sea level to wind stress.

The presence of sea ice is expected to have an impact on the IBE. In a study made by Kwok et al. (2006) the response of ICESat elevations in the Arctic Ocean to sea level pressure resulted in a proportionality constant α = -1.12 cm/mbar. Again near-ideal conditions are found. The deviation from ideal IBE are expected to be caused by the effect of sea ice, wind stress, residuals in the observed elevations and errors in the atmospheric pressure data set. The corrections due to atmospheric pressure variations improves the standard deviation of the elevation differences of repeat tracks from 10 cm to 1.5 cm and emphasize the importance of applying IBE corrections to altimetry data.

The dynamic range of atmospheric sea level pressure is from 985 to 1020 mbar. Thus, the spatial and temporal differences due to the IBE are on the order of a few decimeters.

3.4.4 Ocean tides

The tidal variations are primarily determined by the gravitational attraction of the moon and the sun. The amplitudes are 10 - 60 cm in open ocean with larger values near the coastal regions and marginal seas.

Ocean tide models can be separated into two classes, i) hydrodynamic models and ii) observation models. While the first class uses hydrodynamic equations and the knowledge of astronomical tide generating forces, the latter assimilates observations of the instantaneous sea surface for the estimation of ocean tide parameters. Today, most ocean tide models are hybrid models using both approaches to improve the model. Observations which can be assimilated in tide models predominantly come from satellite altimetry and tide gauges.

The best altimetry data set assimilated for ocean tide models comes from the TOPEX/Poseidon mission launched in 1992 with global accuracies in the order of $\sim$ 2 - 3 cm (Fu and Cazenave, 2001). Due to the sun-synchronous orbit of ERS-1/2 and ENVISAT, their contribution is rather limited, since estimation of tidal solar components will be biased.

Padman and Erofeeva (2004) conclude from the Arctic Ocean tide model (AOTIM-5), that the main constituents are the semi-diurnal constituent M_2 making a total of 79% of the tidal amplitude signal and S_2 representing 10%. Of less importance are the diurnal constituents K_1 contributing only 5% of the tide signal and O_1 with only 1%. Arctic tide height variability is thus dominated by M_2, with amplitudes exceeding 1 m in the southern Barents Sea, the Labrador Sea and the northern area of Baffin Bay (see figure 12). Based on intercomparison of three tide models Peacock and Laxon (2004) estimates the dynamic range in the central Arctic to be $\sim$ 6 - 8 cm for the main tidal constituents.

The presence of sea ice cover changes the dynamics of ocean tides by having a damping effect on the ocean tide amplitudes. It can also lead to a phase lag of cotidal lines. The effect of sea ice cover tends to change tidal amplitudes by up to 10% and phases by 1 - 2 hours Padman and Erofeeva (2004). The comparison of individual constituents with sea ice concentration from observations in Hudson Bay, demonstrates that all constituents are affected by sea ice cover, although the magnitude varies (A. Braun, pers. comm.).

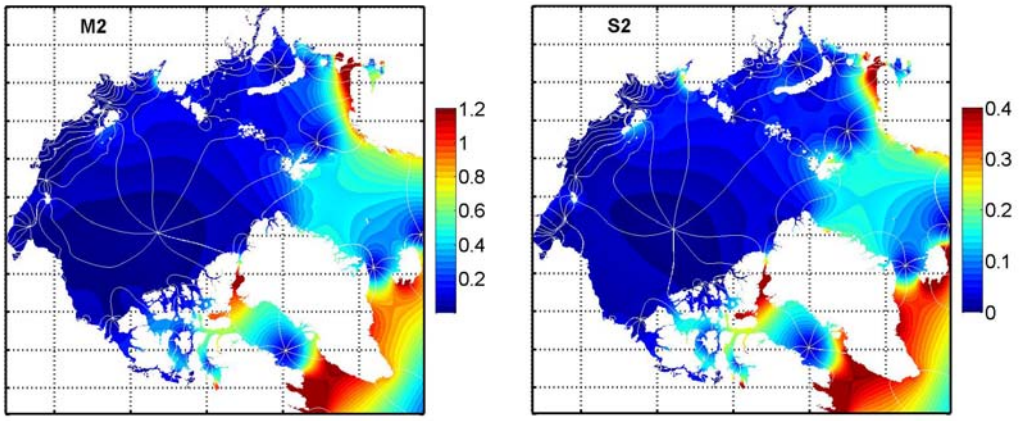

Figure 12: The amplitude and phases of the Arctic Ocean tide constituents (left) M_2 and (right) S_2 (Padman and Erofeeva, 2004). Note the colour scales are not the to scale and given in meters.

3.5 Freeboard heights and snow

In this thesis most of the data is from laser altimetry (ICESat) and the freeboard heights (h_f) are defined to include the snow layer, unless otherwise stated.

The penetration depth of the radar signal depends on the snow density. If sea ice is covered by dry, cold snow, Beaven et al. (1995) concludes from laboratory experiments, that a ku-band radar signal at normal incidence, reflects from the snow-ice interface. In the case of wet snow the radar signal does not penetrate into the snow layer, but reflects from the air-snow interface (Hallikainen, 1992). Multiyear sea ice is more complex than first year ice due to the presence of air pockets, which increases the volume scattering within the ice column and ice lenses confined in the snow layer from previous years melt. In addition the penetration depth of the radar signal, also depends on grain size of the snow and the presence of frost flowers on the surface. A theoretical model of the snow depths influence on the radar waveform over multiyear sea ice, is presented in Tonboe et al. (2006).

Results from recent comparisons of airborne laser measurements and radar altimetry over sea ice find that the laser signal is reflected from a higher surface than the radar signal and the elevation differences are comparable to expected snow depths from Warren et al. (1999). Connor et al. (2008) compared ENVISAT to airborne laser altimetry north of Canada. They find differences in the mean elevations over leads, where no snow is expected, to be 1 cm. The mean difference over smooth level sea ice is found to be 36 cm. Giles et al. (2007) find differences of airborne laser and ku-band radar elevations in the Fram Strait to be 22 cm. Another study made in the Fram Strait by Giles and Hvidegaard (2006) compares ERS-2 freeboard heights to airborne laser altimetry. The differences in measured freeboard heights are found to be within the range of -10 to 40 cm. The magnitude of the difference decreases with increasing temperatures. At the lowest temperatures the differences compares well with expected snow depth. For the highest temperatures the differences are lower than the expected snow depths, confirming that the penetration depth of the radar signal into the snow varies with temperature.

These results are very encouraging for estimation of snow depths from a combination of laser and radar measurements. However, the snow observations from Warren et al. (1999) are based on measurements from Soviet drifting ice stations in 1954 - 1991. The observations are very sparse and might not be representative for today. None of the above surveys are compared to *in situ* measurements.

In the spring of 2006 and 2008 the National Space Institute (DTU Space) as part of ESA's CryoSat Validation Experiment (CryoVEx) carried out an airborne survey with both laser scanner and a ku-band radar (ASIRAS [7]). An extensive airborne and *in situ* program was performed over both multiyear and first year sea ice to determine the performance of the radar. Preliminary results from the comparison of the airborne ASIRAS to *in situ* measurements of snow depth, sea ice freeboard height and ice thickness was presented by Hanson et al. (2007). The elevations of the radar reflection is coincident with the snow-ice surface over smooth level first year ice. The radar signal over multiyear sea ice is much more complex and it was found that the morphology of the buried summer surface of the sea ice adversely manipulates the signal.

Snow depths on sea ice are retrieved from satellite microwave radiometry (Comiso et al. (2003), Markus and Cavalieri (1998)). This method is limited to seasonal sea ice, as the signal from multiyear sea ice is similar to that of snow. A combination of laser and radar

[7] ASIRAS is the airborne version of the SIRAL altimeter to be flown on CryoSat-2

altimetry from satellite is interesting, as in principle, it could provide information on snow depths in the Arctic Ocean. This might be an opportunity made possible by the launch of CryoSat-2 and ICESat-II.

Improved knowledge on snow depths and properties would result in more accurate sea ice thicknesses obtained from freeboard measurements, as this conversion is dependent on the snow depth, as explained in the next section.

3.5.1 Freeboard to thickness conversion

Existing satellite missions only measures the top layer of the surface (the freeboard) and do not measure the bottom of the ice. Comiso et al. (1991) and Wadhams et al. (1992) have found from coincident measurements by laser and upward looking sonar that freeboard heights (h_f) can be converted to sea ice thicknesses (t_{ice}) simply by multiplying by a factor, k:

$$t_{ice} = k * h_f \tag{11}$$

Assuming isostatic equilibrium between sea ice including snow and water, k is given by

$$k = 1 + \frac{\rho_i h_i + \rho_s h_s}{h_i(\rho_w - \rho_i) + h_s(\rho_w - \rho_s)} \tag{12}$$

where ρ is the density, h the height and the subscripts (i), (s) and (w) are that of ice, snow and water. The parameters involved are defined in figure 13, where the sea ice thickness in equation 11 is given by $t_{ice} = h_i + h_s$.

The snow depths and the density of ice and snow can be determined from either climatic models, *in situ* measurements (see figure 13) or by other methods, where coincident measurements of draft and surface are known. Uncertainty in snow depth is by far the largest contribution to errors in ice thickness, see for example Giles et al. (2007). For a given freeboard an underestimated snow depth will give an overestimated sea ice thickness and vice versa.

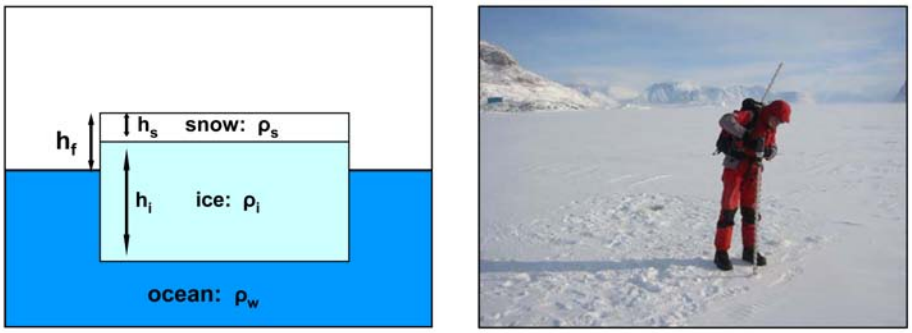

Figure 13: Definition of parameters used in equation 12 (left) and *in situ* drilling (right). Photo by courtesy of F. Dalhoff.

The measurements used in the survey reported by Wadhams et al. (1992) gives an average k-value of 6.89. Using this value, typical Arctic freeboard heights for first year ice is 5 - 30 cm corresponding to 0.30 - 2.0 m in thickness. Level multiyear ice floes are 30 - 60 cm in freeboard heights corresponding to 2 - 4 m thick ice. In this study, the sea ice freeboard heights are not converted into ice thicknesses, as errors in freeboard heights would accordingly increase the errors in thickness by the factor k.

4 Description of data

In the following, the data used in this study is presented. In section 4.1, focus is on ICESat data and section 4.2 introduces the various models used either directly in the processing or for a comparison of the results.

4.1 ICESat data

Unfortunately, the first operational ICESat laser (see chapter 3.1) lasted only 38 days, most likely due to an unexpected failure in the laser system resulting in excessive power degradation. A similar failure was expected to reduce the lifetime of the two other lasers and accordingly a change in the mission plan was recommended by a special selected review board, to fulfill the science objective. In order to obtain intra- and interannual variations the data collection was limited to three months a year (Abshire et al., 2005) representing different seasons: winter (February/March), summer (May/June) and fall (October/November). The second laser lasted almost a year and the third laser stopped working recently on October 22, 2008. Subsequently the second laser was restarted to complete the operation period, but with reduced power (from 80 mJ to 5 mJ). For a complete overview of the operation periods see table 2, where the three lasers are designated laser 1, 2 and 3. There are in total 14 epochs of 33 - 55 days duration. In the last column the laser periods are named after month and year (MMYY), for example laser 1A is named FM03 as it operates in February and March 2003. These names are used throughout this thesis.

Laser ID	Days in Operation	Start Date	End Date	Name
1A	38	2003-02-20	2003-03-29	FM03
2A	55	2003-09-24	2003-11-18	ON03
2B	34	2004-02-17	2004-03-21	FM04
2C	35	2004-05-18	2004-06-21	MJ04
3A	37	2004-10-03	2004-11-08	ON04
3B	36	2005-02-17	2005-03-24	FM05
3C	35	2005-05-20	2005-06-23	MJ05
3D	35	2005-10-21	2005-11-24	ON05
3E	34	2006-02-22	2006-03-27	FM06
3F	33	2006-05-24	2006-06-26	MJ06
3G	34	2006-10-25	2006-11-27	ON06
3H	34	2007-03-12	2007-04-14	MA07
3I	37	2007-10-02	2007-11-05	ON07
3J	34	2008-02-17	2008-03-21	FM08

Table 2: ICESat's operational periods.

During the first mission phases (laser 1 and laser 2A) ICESat repeated ground tracks every eight days for calibration and validation purposes. In the subsequent mission phases, a denser coverage was of priority and an orbit with repeat ground tracks every 91st day with a 33 day sub-cycle was chosen (Schutz et al., 2005). The 8-day and 91-day repeat orbits are composed of 119 and 1,354 orbit tracks, respectively. With these orbit parameters the separation of tracks at equator is approximately 30 km with denser tracks near the poles.

4.1.1 Data files

ICESat data is downloaded directly from National Snow and Ice Data Center (NSIDC) data pool. This study uses the GLA13 product specially adapted to sea ice covered surfaces.

The data files are provided as direct-access binary files. Each file includes geolocated and time tagged surface elevations, as well as information on data quality and geophysical corrections at each spot location (40 Hz). The surface elevations averaged over the footprint area are given, as the measured range minus the height of the satellite with respect to the TOPEX/Poseidon (T/P) reference ellipsoid. Atmospheric delays and tides have been applied to the elevations in the data product.

Various data releases have become available since the first data was published. Each release has improved the data accuracy, as better models and analysis of actual data give the opportunity for improvements. At the time of writing, release 28 is the most recent version complete for all ICESat epochs. A new release 29 is imminent which will include extensive changes to the atmosphere processing, additional corrections to the waveform and elevation processing, as well as the incorporation of a new tide model.

4.1.2 Corrections and filtering

Corrections and filtering of ICESat data is necessary in order to reduce systematic errors such as saturation effects, forward scattering and large miss-pointing from calibration maneuvers, which might cause uncertainties in the measured ICESat heights.

As discussed in various papers, i.e. Fricker et al. (2005), saturation of the waveforms introduce biases from a few centimeters up to one meter in surface elevation. The cause of the saturation is the limited dynamic range of the receiver, which results in distortion of the waveform, making the Gaussian fitting procedure (see section 3.3.3) less reliable. Saturation will arise either from a high natural reflectivity of the surface, or from a low power of the transmitted laser pulse. Especially quasi-specular returns from very bright, flat surfaces causes severe saturation resulting in unreliable surface elevations. This is a particular problem over open leads. Detector saturation caused by higher than predicted energy returns, occurred frequently and is most pervasive in the early operation periods FM03, ON03, FM04, ON04 and FM05.

ICESat data realease 28 includes height corrections due to saturation effects, which have to be applied by the user. The height corrctions are based on empirical relations and varies with received energy. For energies less than 9 fJ no saturation occurs. For energies larger than 9 fJ the saturation elevation correction term (*i_satElevCorr*) from the data product has to be added to the elevation. The saturation correction flag (*i_satCorrFlg*) indicates whether or not the correction term should be applied.

The reflectivity (*i_reflctUncorr*) is calculated as the ratio of the received energy, after it has been scaled for range and the transmitted energy. The reflectivity is highly dependent on the surface albedo, such that a high albedo results in a high reflectivity. This is especially true in the case of quasi-specular returns which have high reflectivities (values larger than 1) and causes severe saturation of the detector (see section 3.3.2). To avoid unreliable elevations, data with a reflectivity value larger than 1 are rejected.

On the other hand scattering by atmospheric constituents, e.g. clouds and water vapor, result in a reduced surface signal and a wide return waveform. This can be seen as a high gain value (*i_gval_rcv*). In this study a gain value larger than 30 is rejected.

The standard deviation of the sea ice Gaussian fit (*i_SeaIceVar*), is the difference between the Gaussian fit and the received waveform using standard parameters. If the standard deviation is zero the reflected waveform is a perfect Gaussian. Larger deviations make the estimation of elevations less reliable, here values larger than 60 mV are rejected.

Both threshold criterias for the gain and standard deviation of the Gaussian fit are implemented from Kwok et al. (2007) and remove all elevations with gain or standard deviation greater than the variance (1σ) above the mean of their sample distribution over the Arctic Ocean.

Other flags recommended to be taken into account in the product usage guide include the flag (*i_ElvuseFlg*), indicating whether the elevations should be used or not. Deviation of nadir view angles results in underestimation of surface elevations. The ICESat product accounts for off-pointing by post-processing of the data. Large antenna off-pointing of the laser occurs primarily under orbit maneuvers, e.g. ocean sweep, for calibration purposes (Luthcke et al., 2003). The flag (*i_AttFlg1*) in the data product indicate large off-pointing and is excluded in this analysis. The attitude quality indicator (*i_sigmaatt*) classifies data as good or bad depending on how well the Precise Attitude Determination (PAD) performs. Here data given a warning flag or classified as bad is excluded.

In addition, unrealistically high elevations are removed by requiring the absolute elevation (*i_elev*) to be less than 100 m and data with more than two peaks in the waveform (*i_numPk*) are also rejected. In sea ice covered regions multiple peaks typically occur if icebergs are present.

LID	output	G>30	S>60	R>1	SAT	|h|>100	OP	σ	P>1	REJ
FM03	5,817,076	16.18	3.13	0.76	5.21	2.60	0.00	0.00	0.04	**27.93**
ON03	5,895,422	30.83	2.44	1.33	0.75	3.42	1.09	0.16	0.03	**40.04**
FM04	6,448,608	22.62	0.85	1.27	0.70	1.86	1.10	0.01	0.00	**28.41**
MJ04	226,746	84.37	1.61	5.35	0.40	0.41	0.94	0.23	0.00	**93.30**
ON04	3,947,716	31.93	4.69	2.01	0.97	3.09	1.18	0.00	0.01	**43.89**
FM05	6,933,136	18.30	1.41	1.46	0.62	3.30	1.61	0.00	0.00	**26.71**
MJ05	3,002,613	26.25	7.01	5.98	1.47	2.87	1.74	0.02	0.00	**45.36**
ON05	3,753,795	33.73	2.92	2.56	0.50	2.73	1.47	0.00	0.00	**43.92**
FM06	6,607,872	22.30	1.06	1.72	0.36	2.30	2.56	0.04	0.00	**30.35**
MJ06	1,115,246	47.70	6.14	5.53	1.01	2.02	2.78	1.52	0.00	**66.69**
ON06	2,485,942	46.33	2.38	2.75	0.50	1.65	2.59	0.18	0.00	**56.39**
MA07	4,314,549	36.88	0.86	1.87	0.36	1.72	1.85	2.56	0.00	**46.10**
ON07	1,262,368	61.59	2.57	4.56	0.55	1.45	1.26	0.00	0.00	**71.98**
FM08	5,518,599	36.62	0.32	1.96	0.37	1.03	1.53	0.02	0.00	**41.84**

Table 3: Rejected ICESat data in percent (%) based on threshold values described above. Gain (G), Standard deviation of Gaussian fit (S), Reflectivity (R), Saturation (SAT), ICESat elevation (h), Off-pointing (OP), sigma attitude (σ), Number of peaks in waveform (P), Total percentage of rejected data (REJ).

The program to read ICESat data and to perform the filtering and corrections is included in appendix F, and the statistics of the threshold criteria are summarized in table 3.

It is seen that the amount of rejected data due to a high gain by far exceeds the other criterias. A particularly large amount of high gain values are found in the ICESat summer (MJ) and fall (ON) periods. This is expected, as the gain is dependent on the

presence of clouds and water vapor in the atmosphere. Thus, a high gain is expected to be coincident with seasons of low ice concetration (summer and fall), where the atmosphere is warmer and more humid than the cold dry winter atmosphere. In addition, the amount of rejected data from MA07 and FM08 are found to be larger than the other winter periods and is correlated with years of low ice extent and concentration (see section 2.3). The same trend is seen for the reflectivity criteria, where a larger amount of saturated data are found to be present in periods of low sea ice concentration.

In the ICESat period MJ04 93% of the data are rejected and the data will be excluded from further analysis, reducing the data analysis to 13 epochs.

4.2 Models

In this section, the various models used either directly in processing or for comparison of the results, are presented. Table 4 gives an overview of the models to be introduced below.

Physical description	Height	Models	Abbreviation
Geoid	h_g	Arctic Gravity Project	ArcGP
Dynamic Topography	h_d	University of Washington Model	UW
Inverse Barometer Effect	h_a	NCEP/NCAR reanalysis	NCEP
Tide Model	h_t	Arctic Ocean Tidal Inverse Model	AOTIM-5
Sea ice	h_f	Quikscat backscatter fields	QuikSCAT

Table 4: Overview of geophysical models used in this study.

4.2.1 Geoid model - ArcGP

The Arctic Gravity Project (ArcGP) geoid model has an accuracy of 10 cm in the open basin and better than 20 cm in narrow fjord systems (see section 6.5). It is based on gravity data from multiple data sources including ground measurements, airborne, marine and submarine data, each with special error characteristics in terms of both accuracy and resolution. Along with these data types satellite altimetry has been used, where no other data could be released, over some ice free and ice covered areas mainly north of Siberia up to the limits of ERS-1 coverage at 81.5°N. More recently, ICESat derived gravity data have been used to correct some errors caused by a lack of data in earlier releases (Forsberg et al., 2007). GRACE Gravity spherical harmonic Model (GGM02S) is used as reference field. For a more detailed description, see Kenyon et al. (2008).

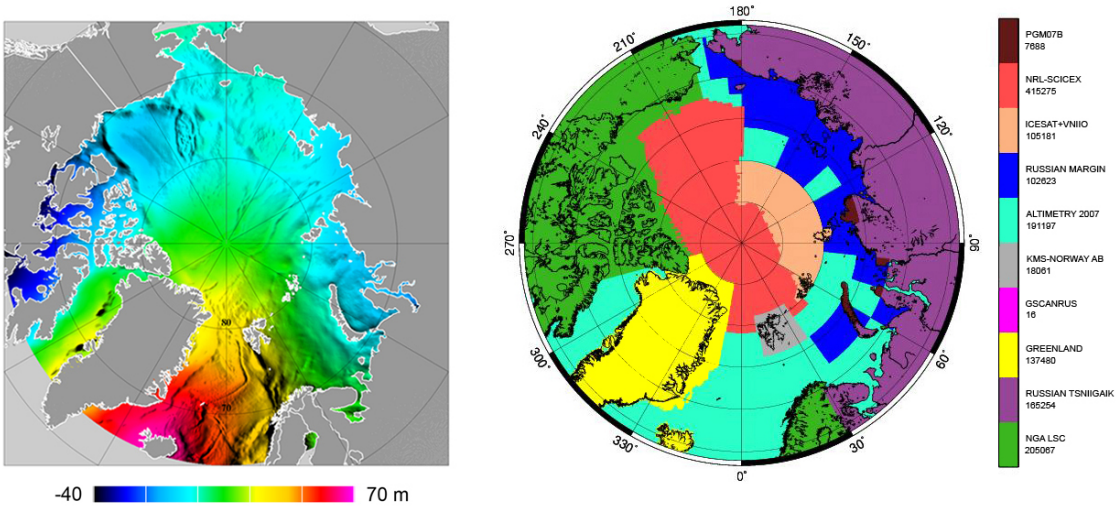

Figure 14: Shaded relief of ArcGP geoid model (left) and colour coded plot of the various data sources used within the ArcGP (right).

The latest released ArcGP 2.0 gravity grid from March 2008 can be downloaded from the U.S. National Geospatial-Intelligence Agency's (NGA) website

http://earth-info.nga.mil/GandG/wgs84/agp/. The grid (5′ x 5′) covers all areas north of 64°N. A plot of the latest released ArcGP geoid model and a plot of the various data sources are shown in figure 14.

4.2.2 Dynamic topography - UW

A combined mean dynamic topography based on satellite altimetry (ERS-2 and ICESat) data has been derived for the Arctic (Skourup and Forsberg, 2008). This mean dynamic topography is compared to the mean dynamic topography derived from three different coupled ice-ocean models; MICOM, PIPS and UW (see figure 15). The oceanographic models show large differences, however, the overall circulation patterns are reproduced with high values towards Canada representing the Beaufort Gyre and low values north of Russia in continuation of the dynamic topography low in the Greenland and Norwegian Seas. It is striking to see the similarities between the altimetry derived mean dynamic topography and that of the UW model. Therefore, in this thesis only the UW model is used for a qualitative comparison of the dynamic topography extracted from ICESat.

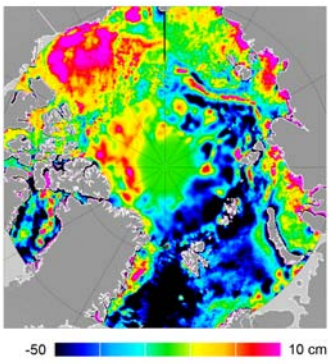

(a) ERS-2/ICESat 1995 - 2005

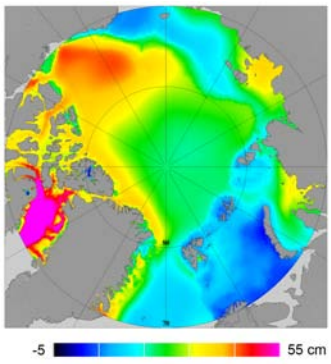

(b) UW 1955 - 2006

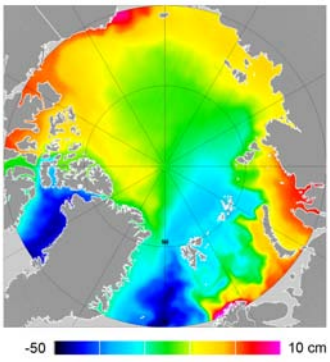

(c) PIPS 1995 - 2003 (March)

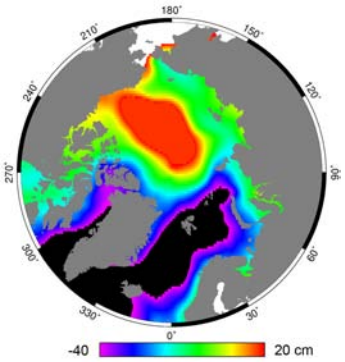

(d) MICOM 1995 - 2003

Figure 15: Dynamic topography from altimetry (a) and coupled ice-ocean models (b - d). The dynamic ranges of the scales are 60 cm, and the offset in mean values is a consequence of inconsistencies in the different reference systems.

The University of Washington (UW) model is a coupled ice-ocean model driven by atmospheric forcing fields from NCEP/NCAR. The resolution of the model is 40 km. A detailed description of the model is not within the scope of this thesis, but can be found in Zhang and Rothrock (2003).

4.2.3 Sea level pressure fields - NCEP/NCAR

To account for the inverse barometer effect (see section 3.4.3) sea level pressure fields are obtained from NCEP/NCAR reanalysis products provided by the NOAA-ESRL PSD Climate Diagnostics Center Branch, Boulder Colorado. The data are available in a gridded format (2.5° x 2.5°) for each 6 hours. The sea level pressure for each ICESat sample is simply linearly interpolated in time and space from the sea level pressure fields and the corresponding height corrections are calculated using equation 10 with a proportionality constant α = -1.12 cm/mbar.

In figure 16 three sea level pressure fields from NCEP/NCAR reanalysis are plotted, showing the development of sea level pressure over three days in March 2003 at 06.00 UTC across the Arctic.

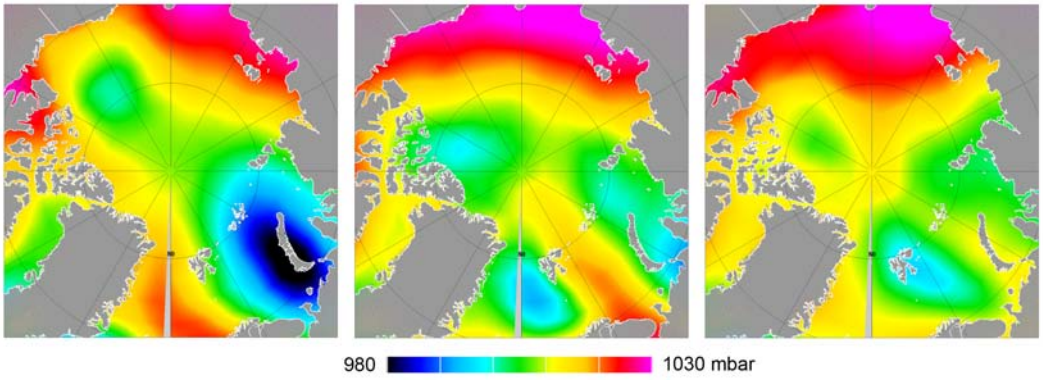

Figure 16: Sea level pressure fields from NCEP/NCAR reanalysis from three successive days in March 2003 at 06.00 UTC.

4.2.4 Tide model - AOTIM-5

ICESat altimeter data have been corrected for tides using the global Goddard/Grenoble Ocean Tide model (GOT99.2), see Ray (1999). This tide model is primarily based on TOPEX/Poseidon altimetry data available south of 66°N, supplemented with several hydrodynamic models in shallow and polar seas.

Here the Arctic Ocean Tidal Inverse Model (AOTIM-5) by Padman and Erofeeva (2004) is used, which uses a combination of TOPEX/Poseidon and ERS altimetry data and assimilates coastal and benthic tide gauges. Accordingly, the AOTIM-5 model is expected to perform better in the Arctic regions. It was concluded in the ArcGICE project (Forsberg et al., 2007) after an intercomparison of various tide models (CSR 4.0, GOT00.2, TPXO6.2, AOTIM-5) that the AOTIM-5 is the best tide model available for the Arctic Ocean.

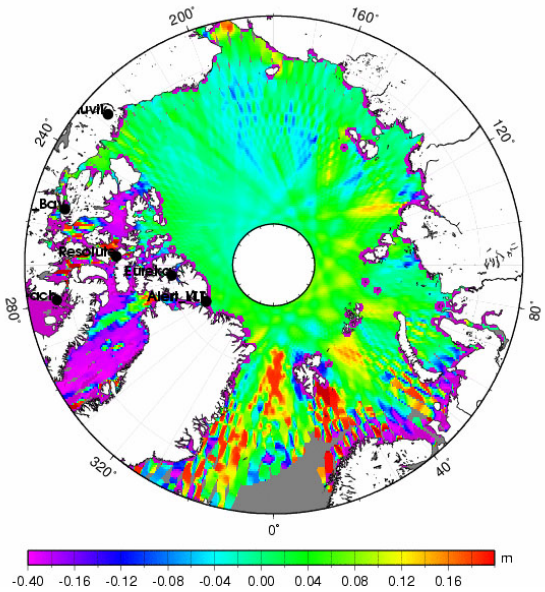

Figure 17: Differences between GOT99.2 and AOTIM-5 tide models applied to ICESat epoch February - March 2003 (Forsberg et al., 2007).

The differences between the two tide models are shown in figure 17 for ICESat epoch February - March 2003. Differences between the two fields are primarily seen in the coastal regions of the Canadian Arctic Archipelago, Nares Strait, the Baffin Bay and Labrador Sea.

4.2.5 Backscatter fields and open ocean mask - QuikSCAT

NASA's scatterometer mission QuikSCAT carries an active ku-band radar. The satellite was launched into a polar orbit in 1999 with a repeat period of 4 days. The outer beam is vertically polarized and covers up to 89.8°N and the inner beam is horizontally polarized and covers up to 88°N. The Polar Sea Ice (PSI) data product is downloaded from CERSAT, at Ifremer, Plouzané (France). Daily grids are available with a spatial resolution of 12.5 x 12.5 km.

Backscatter maps obtained from QuikSCAT PSI product provides information on the distribution of perennial and seasonal ice cover (see section 2.1) and are used in chapter 6.2 to compare to the ICESat derived freeboard maps. The PSI product also comes with an open water mask, which combines backscatter and brightness temperatures to define a 40% sea ice concentration boundary. Thus, surfaces covered by less than 40% sea ice are flagged as open water and are used in this study to mask out returns from open water (see section 6.2.1 and appendix C). For a more detailed description on the system and the PSI data product see Ezraty and Piollé (2001).

5 Method

5.1 Determination of sea surface height

5.1.1 Previous work

In spite of the complicated procedure for radar altimetry (see section 3.3.1), Peacock and Laxon (2004) developed a method to estimate a mean sea surface for the Arctic covering up to 81.5°N based on identification of peaked echoes and retracking, from 4 years of ERS-2 data (1995 - 1999). Cross-over analysis, as well as comparison of colinear tracks (between ERS-1 and ERS-2), show good statistics with only a centimeter level reduction in quality, when moving from ice covered to ice free oceans.

Detection of leads from laser altimetry as reference for the local sea surface height can be done in various ways, dependent on the purpose and quality required. Kwok et al. (2007) compare three methods for lead detection from ICESat observations. They concluded that the highest quality is obtained by comparing leads detected in radarsat images in combination with visual identification of simultaneous low elevations and low reflectivity in ICESat data (see section 3.3.2). The accuracy obtained this way is $\sim$ 2 - 3 cm and within errors of measurement, but the method is unrealistically time consuming for Arctic wide detection of Arctic Ocean sea surface reference points. For comparison, two methods based only on ICESat measurements are presented. The first method requires simultaneous dips in elevations and reflectivity and the second method only requires relative low elevation heights. The accuracies of the two ICESat methods are comparable, but overestimate the local sea surface by up to 4 cm as compared to the visual retrieval method. This is primarily due to presence of thin ice (less than 40 cm) in the leads, corresponding to freeboard heights up to $\sim$ 4 cm. However, the constraint on the low reflectivity limits the number of observations of sea surface heights when compared to the method based on detection of low elevations by approximately 5 times.

McAdoo et al. (2008) use the University College London (UCL) algorithm processing scheme based on specific criteria depending on elevation variations, reflectivity and return pulse shape to estimate the sea surface heights from ICESat. As well, Zwally et al. (2008) use the 2% lowest levels of the ICESat elevations which corresponds 2% lead fraction to find sea surface reference levels in the Weddell Sea in Antarctica.

5.1.2 Processing scheme of this study

In Forsberg and Skourup (2005) a rough estimate of ICESat derived sea surface heights are presented. In this study, the procedure is refined using an improved "lowest-level" filtering procedure to detect the local sea surface heights. The algorithm was originally developed to obtain sea ice freeboard heights for high resolution airborne lidar measurements and used a polynomial fit to the lowest levels (Hvidegaard and Forsberg, 2002). The freeboard accuracy obtained this way, is reported to be $\sim$ 13 cm corresponding to $\sim$ 1 m in thickness (for a discussion on freeboard to ice thickness conversion see chapter 3.5.1). In this study, the filtering method is updated to use a least-square, collocation function estimation, which applies better to satellite laser altimetry data, since the method allow a better control of errors and correlation lengths.

The processing is done in various steps (see figure 18). In the following, each step of the processing is presented and referenced to the flow diagram by box numbers.

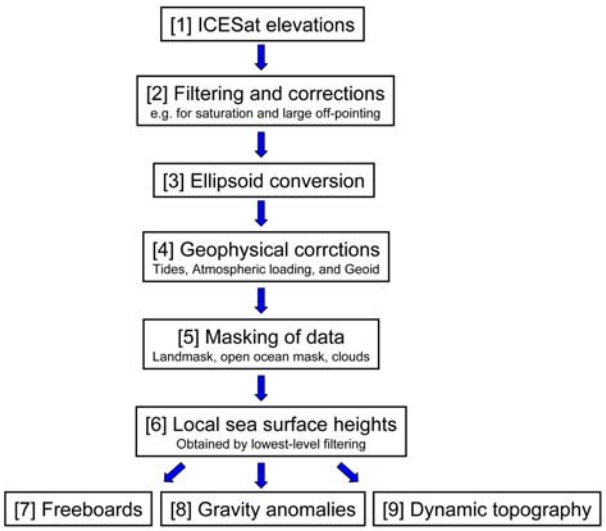

Figure 18: Flow diagram of data processing.

[1] The geolocation, time and elevation are read from the ICESat files for each laser shot.
[2] To remove unreliable ICESat data and to apply corrections to measurements due to e.g. saturation and large off-pointing, filtering are done according to the procedures described in chapter 4.1.2.

[3] The ICESat surface elevations are referenced to the TOPEX/Poseidon (T/P) ellipsoid. However, in this study some of the geophysical models are referenced to the WGS-84 ellipsoid and thus an ellipsoid conversion is necessary. The two ellipsoids have almost identical shapes with T/P smaller than WGS-84. The horizontal positions (geolocation) in the two reference systems will produce a horizontal displacement of only a few centimeters, which is well below the ICESat accuracy estimated pre-launch by Zwally et al. (2002) of less than 6 m. Thus, the horizontal coordinates are assumed to be the same in the two ellipsoid systems. The T/P ellipsoid is approximately 70 cm smaller than the WGS-84 ellipsoid, making the conversion straight forward. At equator the radial difference of the ellipsoids is 70.0 cm and at the poles the difference is 71.4 cm. Here the elevations are referenced to the T/P ellipsoid and data referenced to WGS-84 are converted by adding 70 cm to the elevations to account for the effect of ellipsoid differences.

[4] Geophysical models of the tides, atmospheric pressure loading and geoid are removed from the measured elevations. The AOTIM-5 model is used to correct for tide effects (see section 3.4.4) and atmospheric pressure loading is obtained from NCEP/NCAR sea level pressure fields (see section 3.4.3). The geoid is removed to mask out long-wavelength variations in the sea surface height and for this purpose the geoid representation from the Arctic Gravity Project (ArcGP) is used (see chapter 3.4.1).

Figure 19 shows the various steps of processing for one ICESat track on February 20, 2004. The track is located north of Greenland across the Arctic from Svalbard to the Canadian islands in the Northwest Territories, see inset (a). The transect is approximately 2,700 km long corresponding to $\sim$ 16,000 ICESat measurements.

The upper plot shows ICESat elevations (green) after filtering out poor data and correcting for tides and atmospheric pressure loading. For each ICESat measurement, the corresponding geoid height (black) is estimated by bilinear interpolation of ICESat data to the ArcGP geoid grid. The two curves illustrates the large contribution of the geoid to the sea surface topography. Near the beginning of the plot (2,700 - 2,850 sec) large outliers are detected primarily caused by land effects when ICESat overflies the Canadian islands and to a lesser extent by clouds.

[5] Most of the outliers are removed by applying a landmask. Here, a combined topography and bathymetry model (Andersen and Knudsen, 2008) is used gridded in 0.025° x 0.025°, where ICESat data points corresponding to topography/bathymetry values higher than -2 m are removed.

In the lower plot of figure 19 the residual heights ($h_r = h - h_{tides} - h_{IB} - h_{geoid}$) of ICESat elevations after removal of geoid heights are plotted, revealing the nature of the measured surface at shorter wavelengths. In a perfectly described system, the residual heights are a combination of dynamic topography and sea ice freeboard heights (see equation 6). However, errors in the geophysical models utilized here (tide, atmospheric pressure loading and geoid), as well as instrument and measurement errors from ICESat, all contribute to the residual heights.

Histograms of the residuals are plotted for each ICESat period, see inset (b) in figure 19. The histograms seem to be normally distributed. To remove the rest of the outliers (which were not removed by the landmask) from the measurements, an upper and lower threshold are defined for the residual heights. The threshold values are selected by visual inspection of the histograms. The lower limit selected here is -1.5 m and the upper limit used is 2.0 m, which leaves a 3.5 meter wide window for acceptable data. The statistics for data rejected by the threshold is summarized in table 5. The percentage of rejected data is relatively low for both limits, with more data rejected by the upper limit (0.07 - 0.20%) compared to the lower limit (0.01 - 0.06%). The limits seem to be reasonable, as they do not mask out much data and the 3.5 m window is within the expected values of sea ice freeboard heights (typically in the range 30 - 80 cm) and the amplitude of dynamic topography (ranges by up to $\sim$ 1 m across the Arctic).

Laser ID	h_r **> -1.5 m** [%]	h_r **< 2.0 m** [%]	**Total measurements in file**
FM03	0.01	0.11	5,593,885
ON03	0.03	0.14	5,630,209
FM04	0.01	0.09	6,202,518
ON04	0.02	0.14	3,770,617
FM05	0.02	0.13	6,606,772
MJ05	0.01	0.18	2,888,691
ON05	0.02	0.12	3,583,615
FM06	0.02	0.10	6,348,995
MJ06	0.06	0.16	1,057,145
ON06	0.02	0.10	2,365,791
MA07	0.05	0.10	4,122,017
ON07	0.02	0.20	1,186,326
FM08	0.02	0.07	5,325,294

Table 5: Rejected data based on threshold values applied to the residual heights (h_r).

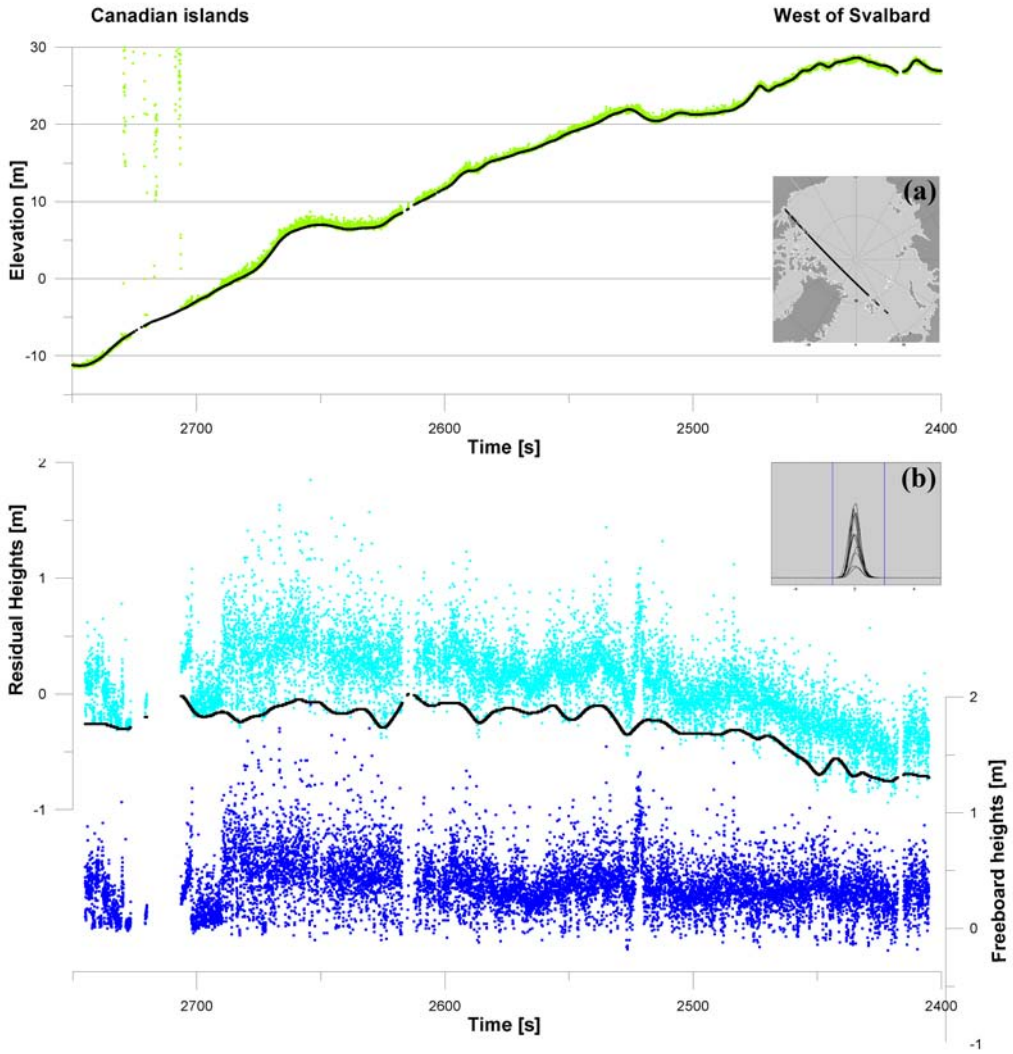

Figure 19: Presention of data from one ICESat track to illustrate the processing procedure. The upper plot represents ICESat elevations (green) and ArcGP geoid heights (black), both referenced to the T/P ellipsoid. The lower plot shows residual heights (cyan) and estimated local sea surface heights (black). The sea ice freeboard heights (blue) are found by subtracting the residual heights from the sea surface heights. The time scales are reversed to match the track plot in inset (a). The histograms in inset (b) are representations of the residual heights, one for each ICESat period.

[6] In order to locate the local sea surface from the residual heights (h_r), a "lowest-level" filtering procedure is applied. First, the average of the three lowest values of h_r is found for each along-track interval of 20 km ($\sim$ 115 ICESat measurements). By averaging the three lowest levels the procedure becomes more robust to outliers. The lowest levels selected this way represents leads of either open water or thin ice. The selection criteria assumes the lead fraction to be $\sim$ 2.5%, which are representative for winter conditions (see section 2.4). Next, a smooth curve determined by least-squares collocation, is computed between the lowest levels represented by the black curve in the lower plot of figure 19. For collocation a second order Markov model is used with correlation length 40 km and root-mean-square noise of 0.2 m. The curve obtained this way represents an estimate of the local sea surface height ($\tilde{h}_{ssh}$) including dynamic topography and errors related to the geoid, tides and atmospheric pressure loading. The program to perform the "lowest-level" filtering algorithm is included in appendix F.

5.1.3 Sea ice freeboard heights

[7] The freeboard heights in figure 19 (blue) are estimated by subtracting the residual heights from the estimated sea surface heights, $\tilde{h}_f = h_r - \tilde{h}_{ssh}$. The method basically filters out long wavelength variations. Sea ice freeboard heights are calculated for each ICESat track and averaged over 1 second corresponding to 40 measurements. Freeboard data from each campaign period are gridded using weighted means into a grid with resolution of 0.1° x 0.2°.

5.1.4 Dynamic topography

[9] The local sea surface height ($\tilde{h}_{ssh}$) estimated by collocation (the black line in figure 19 lower plot), is basically the dynamic topography (see equation 6) if model inaccuracies and measurement errors are neglected. In this study the large-scale dynamic topography is estimated for each ICESat period from the sea surface heights found in section 5.1.2. To reduce some of the noise, the sea surface heights are averaged along-track for each second (40 ICESat measurements). The averaged tracks are cross-over adjusted, gridded using the same gridding procedure as used in the freeboard calculations and filtered. The filter is a Gaussian filter in the space domain with full-width resolution taken to be 2°.

5.1.5 Mean sea surface and gravity anomalies

[8] The gravity field is stationary on the timescales of this study (2003-2008) and the sea surface heights (averaged and cross-over adjusted) for each of the ICESat epochs are merged and draped into one combined mean sea surface. Only data north of 77.5°N is included, as the track spacing increases at the more southern latitudes. The combined mean sea surface is approximated to be the geoid by neglecting the dynamic topography according to equation 6. The geoid is inverted into gravity anomalies by techniques equivalent to the derivation of marine gravity anomalies from satellite radar altimetry over open ocean. Here is used a Fast Fourier Transform (FFT). Only long wavelengths are taken into account in the computations and a Wiener filtering method is used to suppress short-wavelength noise. In the Fourier domain it is expressed as

$$F(\Delta g) = G\frac{k}{1+ck^4}F(N) \tag{13}$$

where F is the two-dimensional Fourier transform, k is the wave number and c is a resolution constant described by Forsberg and Solheim (1998) and also by Andersen and Knudsen (1998). The above technique is used in combination with a remove-restore technique, to keep longer wavelength information from the global GRACE model GGM02S. The gravity computations are performed using the GRAVSOFT program package (Forsberg and Tscherning, 2008).

6 Results and discussion

In this chapter, the ICESat results based on the method described in chapter 5, are presented and discussed. Section 6.1 includes the results from the airbone underflights of satellites with high resolution laser scanner to investigate the reliability of the "lowest-level" filtering method. Results of the Arctic Ocean sea ice freeboard heights and a comparison to QuikSCAT backscatter maps, are presented in section 6.2, togehter with trends in the seasonal and year-to-year variations of the sea ice freeboard distributions.

In section 6.3 the dynamic topography found for each ICESat periods are compared to the oceanographic model from University of Washington, and the coupling to large scale atmospheric circulation are investigated. In section 6.4 the ICESat gravity anomalies from the combined mean sea surface is compared to existing Arctic Gravity Project, as well as high resolution airborne gravimetry measurements. Section 6.5 presents a regional study of geoid accuracy from geoid models and the ICESat geoid based on GPS measurements along a profile in a west Greenland fiord system. Finally, section 6.6 includes a comparison of sea ice freeboard heights obtained by the "lowest-level" filtering method used in this study to a method, where the sea surface height has been found from models.

6.1 Comparison of freeboard heights from satellite altimetry and airborne laser scanner measurements

As part of this study, three underflights of satellites were carried out with high resolution airborne laser scanner. A more detailed description of the laser scanner system is given in Hvidegaard and Forsberg (2002). This was done, to evaluate the sea ice freeboard heights obtained from satellite altimetry (see section 1.2.2). The locations of the various surveys are illustrated in figure 20.

A near-coincident underflight of ICESat was performed on May 25, 2004. Two lines, each of length $\sim$ 50 km, were flown north of Greenland under heavy ice conditions dominated by 70 - 100 cm high freeboard heights. The results of the survey are presented and discussed below (section 6.1.1). Another attempt was made on April 12, 2007, north of Alaska to investigate an area of primarily thinner ice types with freeboard heights in the order 40 - 70 cm. Unfortunately the flight track did not match the ICESat track, see appendix D.

Figure 20: Location of airborne underflights (left) of ICESat; blue stars May 2004, red triangle March 2006 (Kurtz et al., 2008), yellow dot April 2007 and of ENVISAT green square May 2006. Twin - Otter used for the survey, April 2007 (right).

An attempt to compare airborne laser altimetry to ENVISAT radar altimetry was carried out in the Fram Strait on May 2, 2006. The intention was to investigate penetration depth of the radar satellite altimeter (see section 3.5). Individual echoes (IE) of the ENVISAT altimeter was requested from ESA over the study area to achieve the highest along-track resolution. Unfortunately, ENVISAT never acquired the IE waveforms for the particular track. Analysis of the averaged waveforms was carried out, but results were hampered by snagging effects, see appendix E.

6.1.1 ICESat versus airborne laser scanner

In the heavy ice conditions north of Greenland with only a few open leads the two tracks of ICESat freeboard heights are underestimated by 36 cm and 37 cm, respectively, when they are compared to the airborne freeboard heights (Skourup and Forsberg, 2006). This is also apparent in the freeboard distributions, where there are fewer freeboard heights of the thinnest and thickest ice classes in the ICESat freeeboard distributions than in the freeboard distributions from the airborne laser scanner data (see figure 5 in Skourup and Forsberg (2006)).

A similar study of ICESat freeboard heights were measured over thinner ice by Kurtz et al. (2008) on March 24, 2006, north of Point Barrow, Alaska (see figure 20). Kurtz et al. (2008) found less than 2 cm of bias in areas with open leads and relative flat level ice. However, the thicker ice classes ($h_f \sim$ 55 - 70 cm) with fewer open leads resulted in an underestimation of ICESat freeboard heights by up to 9 cm.

It is concluded, that the "lowest-level" filtering technique for ICESat underestimates the sea ice freeboard heights by up to 37 cm in heavy ice conditions where only a few open leads are present. The bias is a consequence of the lower spatial sampling of ICESat and also due to averaging the freeboard across the footprint area (see section 3.3.3). The bias increases with increasing ice thickness with few open water leads.

Prior knowledge of the expected ice thickness and concentration could in principle be used to correct the sea ice freeboard heights by adding a bias. However, this procedure would require a detailed knowledge of the relationship between the bias and ice conditions.

Another attempt to solve the problem is based on the fact that low reflectivity in the ICESat data is correlated with newly refrozen leads (see section 3.3.2). Only very few cases of low reflectivity are found in the two ICESat subtracks (Skourup and Forsberg, 2006), indicating that ICESat picks up very few open or thin-ice leads to represent the lowest levels. In concert, Kurtz et al. (2008) found the characteristic low dips in areas with thin ice, where the bias was small. Different attempts to estimate the sea surface heights from elevations and reflectivity threshold criterias, were investigated by Kwok et al. (2007) and discussed in section 5.1.1. The most robust method resulted in a small bias, but in a significant reduction in data, as well as a time consuming processing.

6.2 Sea ice freeboard heights

The left column of figure 21 displays a seasonal cycle of ICESat derived Arctic Ocean sea ice freeboard maps covering October - November 2005 [ON05],
February - March 2006 [FM06] and May - June 2006 [MJ06]. The QuikSCAT backscatter maps for the corresponding periods are shown in the right column next to the freeboard maps. An overview of the sea ice extent is shown in appendix C.

All periods in figure 21 show geographic variations typical for the Arctic with thick perennial sea ice north of Greenland with freeboard heights up to 1 m (corresponding to a sea ice thickness of 6 m) forced towards the coast by the Beaufort Gyre. Thin seasonal ice is found in the Russian Arctic with 5 - 30 cm freeboard heights (corresponding to 0.3 - 2.0 m ice thickness).

The ICESat freeboard maps show seasonal variations. [ON05] represents fall conditions during the freeze up season. The area north of Greenland and eastern Canada is covered by thick multiyear and deformed ice with freeboard heights larger than 35 cm. In the Siberian Arctic (Chukchi Sea) seasonal ice has started to form. The freeboard heights of the seasonal ice depends on the number of days since first day of freeze up and on temperature. In this example it consists of open water and thin sea ice of only a few centimeter freeboard heigths (5 - 15 cm). [FM06] The FM06 data set represents winter conditions. This time a year the sea ice has almost reached its maximum thickness. The Siberian Arctic is fully covered by seasonal ice grown to its maximum thickness corresponding to freeboard heights of 20 - 30 cm. [MJ06] The beginning of May is the onset of the melt season. The freeboard map of MJ06 shows ice freeboard heights comparable to FM06, however, the extent of the perennial ice cover has decreased due to the accelerated outflow of sea ice through the Fram Strait and to a less extent by redistribution due to rafting and ridging (see section 2.3.2).

There is a clear spatial correlation between the ICESat freeboard maps and the QuikSCAT backscatter maps, where large sea ice freeboard heights (> 35 cm) are correlated with high backscatter (> -14.5 dB) from thick multiyear sea ice (Kwok, 2004).

Similar freeboard and backscatter maps for the rest of the ICESat periods are presented in appendix A. In all of the sea ice freeboard maps, there is an anomaly covering approximately 86°N, 80°E to 82°N, 120°E, which is not a characteristic sea ice feature. If the anomaly is compared to a bathymetry map (see figure 1), it is found to coincide with the Gakkel Ridge. Thus, the signal is identified as an potential error in the modelled gravity field (ArcGP). A further discussion of this issue is given in section 6.4.

Preliminary results from earlier ICESat data release 18 are enclosed in appendix B. The data in release 18 freeboard maps are much noisier than compared to release 28. The improvements can primarily be explained by the applied saturation effects in release 28. Some of the residual tracks seen in data release 18, e.g. north of Russia, are removed when using the updated data by removing data flagged as large off-pointing (see section 4.1.2).

6.2.1 Freeboard distribution, mean and standard deviation

In the calculation of the sea ice freeboard distribution, mean and standard deviation, data over open ocean are masked out using the QuikSCAT sea ice/open ocean masks presented in appendix 4.2.5. This is done to remove false freeboard heights over the open ocean, originating from the "lowest-level" algorithm favoring the trough of the waves. In addition, the Baffin Bay area is masked out, as the ICESat tracks are very sparsely distributed in this region.

Histograms of freeboard distributions

ICESat freeboard distributions are plotted in figure 22 with freeboard resolution of 0.1 m. Each histogram represents one ICESat period. In order to see the interannual variations, the winter and fall periods are plotted separately in figure 22 and are discussed further in section 6.2.2.

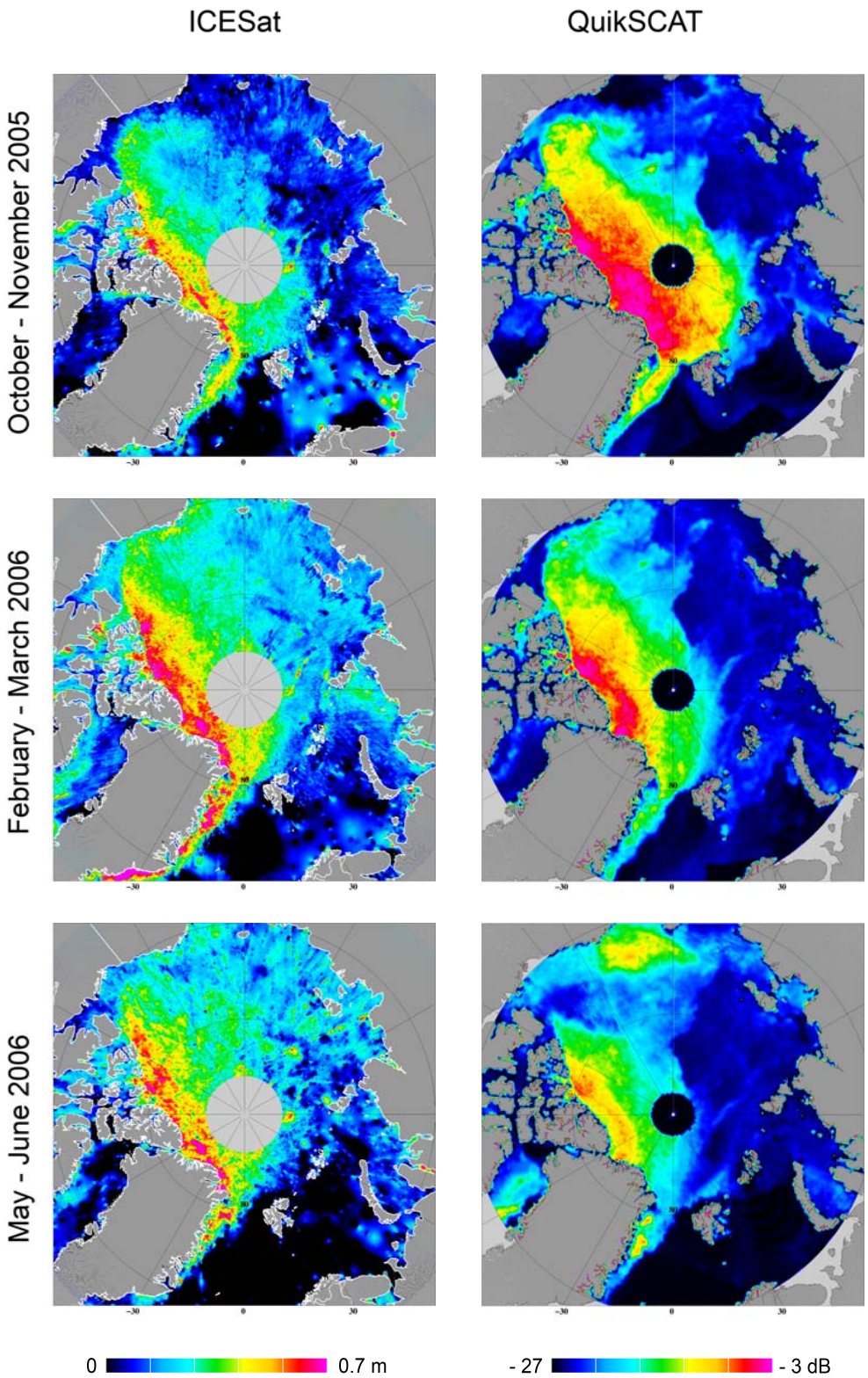

Figure 21: Sea ice freeboard maps from ICESat (left column) and QuikSCAT backscatter maps (right column).

In general, the freeboard distributions have an assymetrical shape with a sharp increase in the leading edge and a long tail. This shape is characteristic for sea ice freeboard heights, drafts and thicknesses, where the long tail represent the presence of thick multiyear ice and deformed ice due to ridging and rafting processes.

Mean and Standard deviation

The mean and standard deviation of the freeboard heights for all 13 ICESat periods are given in table 6.

MMYY	# points	h_f < 0 cm [%]	mean [cm]	std [cm]
FM03	4,586,098	2.2	34.3	20.0
ON03	4,081,973	3.6	34.3	19.5
FM04	5,033,872	3.9	29.8	19.8
ON04	2,951,666	4.2	33.3	22.1
FM05	5,365,088	3.9	37.6	26.9
MJ05	2,312,373	3.7	37.0	24.7
ON05	2,834,733	5.9	27.4	20.5
FM06	5,189,913	4.0	33.2	23.8
MJ06	803,436	5.8	36.6	24.5
ON06	1,840,521	7.0	27.7	20.4
MA07	3,234,920	4.0	30.4	20.7
ON07	776,353	8.3	24.8	17.2
FM08	4,197,072	4.3	22.4	16.9

Table 6: Freeboard statistics with ICESat period (MMYY), total number of data points (# points), percentage of negative freeboard heights (h_f < 0 cm) removed from the statistics, mean and standard deviation (std).

The mean and standard deviation ranges from a minimum (mean 22.4 cm, std 16.9 cm) in FM08 to a maximum (mean 37.6 cm, std 26.9 cm) in FM05. The standard deviation reflects the variability of the freeboard heights. Thus, FM05 includes a wider range of freeboard heights than FM08.

To model the reference sea surface heights the mean of the lowest 2.5% of the elevations is used (see section 5.1.2). This method will lead to a minor part of the freeboard heights being negative. To account for the unphysical conditions caused by model inconsistencies, where the return is from scattering within the water column, negative freeboard heights are removed from the statistics. The percentage of the discarded negative freeboard heights are presented in the third column of table 6.

As the freeboard distributions are not normal distributed, it can be discussed if the mean and standard deviation are representative parameters to describe the freeboard heights. In the following interpretation of the seasonal and interannual trends the mean values and the corresponding freeboard distributions are analyzed together.

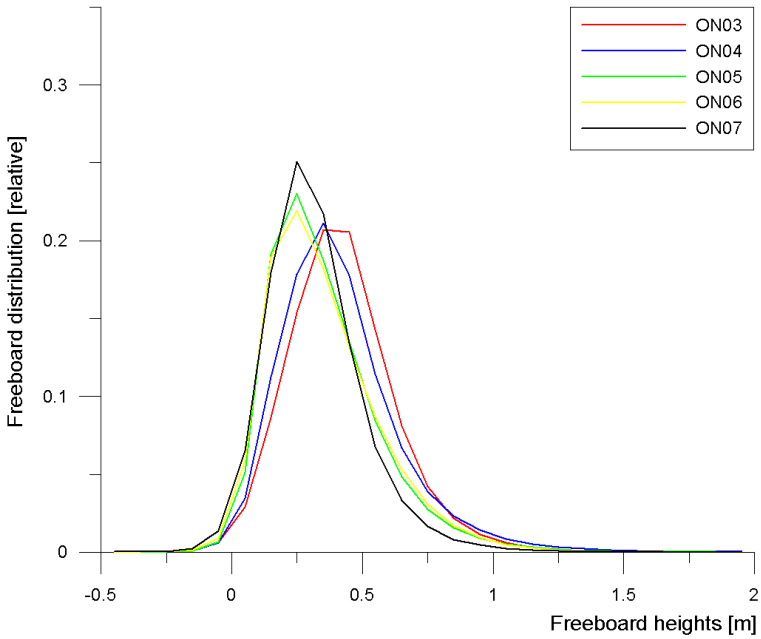

(a) October - November (ON)

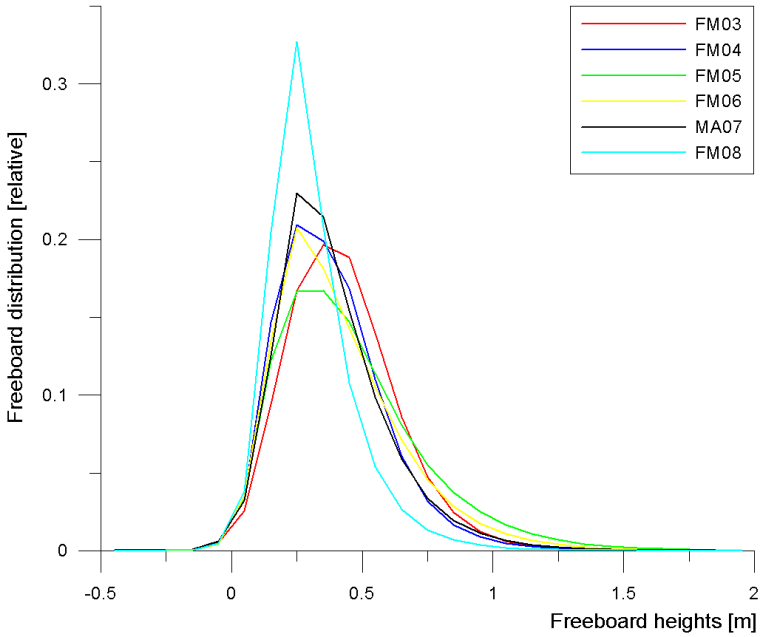

(b) February - March (FM)

Figure 22: Distribution of sea ice freeboard heights from all the ICESat periods.

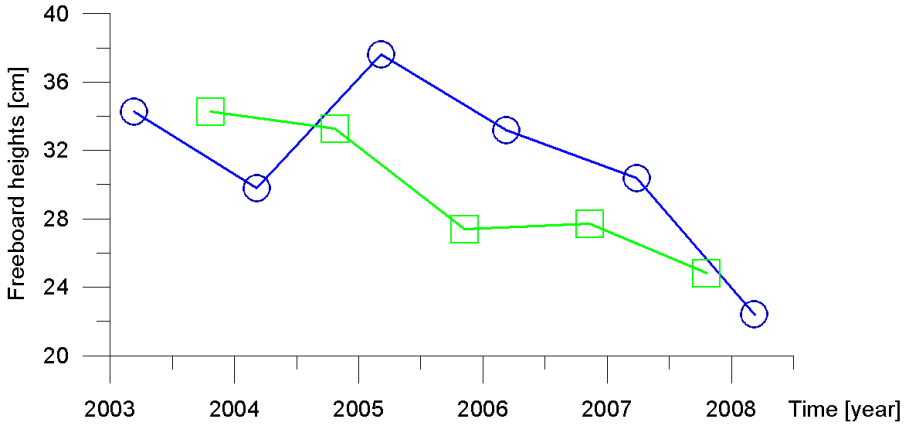

Figure 23: Mean sea ice freeboard heights in the Arctic. Blue circles February - March (FM) and green rectangles October - November (ON).

6.2.2 Interannual and seasonal variations of sea ice freeboard heights 2003 - 2008

Figure 23 shows the October - November (ON) and February-March (FM) mean sea ice freeboard heights listed in table 6. There are only mean sea ice freeboard heights available for two May - June (MJ) ICESat periods. These are not shown in the figures, but are discussed briefly, later in this section.

Interannual variations

There is a decrease of 9.5 cm or 27% in the ON mean freeboard heights (green) during the ICESat periods 2003 - 2007. This trend is supported by the freeboard distributions presented in figure 22 (a), where the histograms shift towards thinner ice types through the years. In addition, there is less sea ice with freeboard heights larger than 50 cm in ON07, than in the previous years.

The ON decrease of 27% is consistent with the decrease observed by Haas et al. (2008), who found a decrease of 20% for multiyear sea ice and 28% for first year sea ice from September 2001 to September 2007.

The FM freeboard heights (blue) show a maximum in 2005 and decrease by 15.2 cm to a minimum in 2008. The mean values of 2003 and 2004 are lower than the maximum value in 2005. However, as seen in figure 22 (b) the freeboard distribution of 2003 is shifted towards thicker ice than the subsequent years. In the years 2004 - 2007 the histograms are almost identical with more deformed ice (freeboard heights larger than 60 cm) in the 2005 and 2006 freeboard distributions. Clearly, the ice freeboard heights in 2008 are shifted towards thinner ice types with almost no ice freeboard larger than 1 m. Based on the freeboard distributions, the mean values for FM03 and FM04 might not be representative for the sea ice thickness trends.

As described in section 2.3.2 the partial extent of perennial and seasonal ice cover has changed. The perennial ice extent representing the thicker ice classes is decreasing and is replaced by seasonal ice, causing a decrease in the overall mean freeboard in the Arctic Ocean. What follows, is an estimate of the changes in mean freeboard heights originating from the partial changes of perennial and seasonal sea ice extents. This is done, to

investigate whether or not the values found from ICESat, are realistic. The estimate is made for March only, as there are no such observations available for October - November.

In 2004 the perennial sea ice extent was 5.0 million km^2 (Nghiem et al., 2006)[8] and in 2008 it is 2.6 million km^2 (Nghiem and Neumann, 2009). There is a group of mixed ice classes consisting of compressed first year sea ice, which has similar backscatter signatures as multiyear ice. The extent of the mixed ice classes covers $\sim$ 3.0 million km^2 and is assumed to be constant. The total sea ice extent of all ice types is relatively stable through 2004 - 2008 and here taken to be 14 million km^2 (Nghiem et al., 2006). Even though the total ice extent changes it does not affect the mean values, as long as the partial coverage is taken relative to the total extent. Using these numbers, approximately 60% of the total ice extent consists of perennial and mixed ice classes in 2004, which is a realistic value supported by the result found in Kwok (2004) (see section 2.3.2). The value decreases to 40% in 2008. At the end of the growth season, the freeboard heights of the seasonal ice is assumed to be 20 cm (corresponding to 1.4 m thick ice) and the perennial and mixed ice classes 50 cm (corresponding to 3.4 m thick ice).

This estimate results in a mean sea ice freeboard of 38 cm in 2004 and 32 cm in 2008, correponding to a decrease of 6 cm (or 16%). The changes in the observed ICESat mean freeboard heights for the same time period is 7.4 cm, which is close to the estimated value. Actually, the maximum freeboard height (37.6 cm) obtained in FM05 might be more representative (as observed in the freeboard distribution). This would result in a decrease of 15.2 cm in mean freeboard heights and is much larger than the estimated value. However, it is a very rough estimate and a decrease in the various ice types as a response to a warmer atmosphere, are not included. If the response to increased temperatures in FM is about the same value (27%) as in ON, the decrease in ice freeboard heights is $\sim$ 10 cm. Thus, a combination of the general decrease of the various ice types and a decrease due to the reduction of the perennial ice extent, in total 16 cm, make the ICESat observations realistic.

Seasonal variations

The mean freeboard heights in FM are expected to be higher than ON freeboard heights, as ON is in the beginning of the freeze up season, whereas FM is just before maximum ice thickness is reached. The expected changes in freeboard heights for first year ice between ON and FM is primarily from thermodynamic growth and to a less extent from accumulation of snow depth. The total increase in first year ice freeboard heights is approximately 10 - 20 cm. In the same time span the growth of multiyear sea ice is mainly from snow accumulation and in the order of 5 - 10 cm (see section 2.1).

Through 2003 - 2008 the differences between ON and FM mean ice freeboard heights are -4.5 cm, 4.3 cm, 5.8 cm, 2.7 cm and -4.0 cm. Even though most of the differences are positive, the seasonal changes in freeboard heights are smaller than expected. This can partly be explained by a reduction in the spatial coverage of the perennial ice cover, since a larger amount is flushed out through the Fram Strait during the winter. The decrease is estimated by Kwok (2004) to be 15% from January to May, however, this would only explain a reduction of less than 5 cm in mean freeboard.

A more likely cause is due to biases introduced in the freeboard heights from the "lowest-level" filtering procedure used to detect the local sea surface heights, which are

[8]The actual value reported is 5.2 million km^2 for November - December. The corresponding value for November - December 2004 is 4.7 million km^2 and the March value is 4.5 million km^2. A similar decrease in perennial sea ice extent of 0.2 million km^2 between November - December and March is assumed for the 2005.

dependent on freeboard heights and lead fraction (see section 6.1.1). In ON the sea ice is thinner and the lead fraction are larger than in FM (see section 2.1 and 2.4). Consequently, the biases are expected to be smaller in ON than FM. This is supported by comparing results from the ON05 and FM06 from this study with a similar study made by Kwok et al. (2007) (to be referenced KW07 throughout this section), where a different method was used.

KW07 found mean freeboard heights to be 27.5 cm and 35.0 cm, for ICESat periods ON05 and FM06, respectively. In this study, mean freeboard heights for ON05 and FM06 are found to be 27.4 cm and 33.2 cm, respectively (see table 6). The resulting increase between the two epochs is 5.8 cm, which is 1.7 cm less than observed by KW07. The mean freeboard heights for ON05 of thinner sea ice types and larger lead fraction are found to match well with KW07. The FM06 freeboard heights are, however, underestimated in this study compared to KW07.

KW07 uses a 25 km running mean to model the large-scale variations in the sea surface heights and a combination of low elevation and low reflectivity to select the sea surface reference heights (see section 5.1.1). Kurtz et al. (2008) have shown, that the use of running means (25 km and 50 km) perform better in thicker ice types ($h_f \sim 55$ - 70 cm) with few open leads, as compared to a method equivalent to the method used here. Compared to the method presented in this study, Kurtz et al. (2008) use longer intervals (50 km) and assumes less coverage of open water leads (1%). The 1% "lowest-level" method underestimates the ice freeboard by 9 cm when compared to airborne laser measurements, whereas the running mean method only underestimates the ice by 4 cm. For thinner ice types the two methods result in comparable biases, see also discussion in section 6.1.1. Thus, the larger freeboard heights for FM06 found in this study could in princible be underestimated by the a few centimeters, when compared to the study performed by KW07.

Both ICESat summer periods (MJ05 and MJ06) have mean freeboard heights of about 37 cm (see table 6), which are almost the same as the corresponding winter periods (FM05 and FM06). In general, the sea ice freeboard heights are growing due to a moderate snow accumulation (about 5 cm) between FM and MJ. Thermodynamic growth and melt are almost absent in the intervening period, and a small decrease in the mean thickness is expected due to an increased outflow of multiyear ice through the Fram Strait. The ON freeboard heights are $\sim$ 10 cm lower when compared to MJ. After the melt season the freeze up has begun and thus, the ON mean sea ice freeboard heights are expected to be lower than MJ. Based on the above it is diffucult to give a reasonable estimate of the expected growth and melt of the sea ice between FM, MJ and ON, due to the many processes involved. Thus, it is difficult to conclude if there are any biases introduced from the "lowest-level" technique.

As a conclusion, intercomparison of sea ice freeboard heights between seasons should not be performed based on ICESat observations due to the biases introduced in the results from the "lowest-level" filtering method. Interannual variations from a given season are expected to be more reliable, as the lead fraction is more stable within a given month when compared to inter-seasonal variations. Since the beginning of the ICESat observations in 2003, a decrease in the mean freeboard heights of approximately 10 - 15 cm (corresponding to $\sim$ 70 - 75 cm in thickness) is observed. These are realistic values and can be explained by a combination of a decrease in the perennial sea ice extent, together with a general decrease in the ice thickness due to an increased heating of the atmosphere and ocean.

6.3 Dynamic topography

In this section, the results of the dynamic topography ($\tilde{h}_{ssh}$) obtained by the method described in section 5.1.4 are presented.

ICESat periods of less than 2.5 million measurements (see table 5) are excluded from the analysis due to limitations in the cross-over adjustment program. This excludes the periods MJ06, ON06 and ON07 leaving 10 of the original 13 ICESat periods. The mean and standard deviation of the dynamic topography for each ICESat period is presented in table 7 before and after cross-over adjustment. Results from ICESat release 18 and data from the ERS satellite, are also included in the table for the periods FM03 - MJ05.

Biases between the different ICESat epochs are apparent, but are smaller for the ICESat data release 28 than for release 18. This is primarily due to improvements in the release 28 data, where the measured altimeter heights have been corrected for saturation effects (see section 4.1.2). As outlined in section 6.1.1 the "lowest-level" filtering procedure applies additional biases, and errors related to the geoid, tides and atmospheric pressure loading. However, the ICESat dynamic topography results are comparable to results obtained from the ERS satellite

	ICESat						**ERS**	
	Release 28				**Release 18**			
	before x-adj		**after x-adj**					
	mean	**std**	**mean**	**std**	**mean**	**std**	**mean**	**std**
FM03	-24.6	20.0	-25.3	18.2	-48	21	-21	35
ON03	-30.4	17.1	-31.2	13.9	-57	17	-30	34
FM04	-21.6	17.5	-22.5	14.7	-29	19	-3	34
ON04	-28.5	16.4	-28.8	14.8	-60	20	-32	35
FM05	-40.1	21.2	-41.3	17.5	-66	21	-37	35
MJ05	-14.0	17.6	-12.8	15.7	-24	23	-24	38
ON05	-24.1	18.8	-25.1	16.3	-	-	-	-
FM06	-26.6	20.8	-28.4	17.8	-	-	-	-
MA07	-24.9	23.2	-26.4	20.9	-	-	-	-
FM08	-22.5	22.1	-23.5	20.7	-	-	-	-

Table 7: Statistics of the dynamic topography from ICESat data release 28 before and after cross-over adjustment covering 70 - 86°N, ICESat data release 18 and ERS data in the overlap band 79 - 81°N. Mean and standard deviation (std) are both given in cm.

The dynamic topography derived from ICESat data is prestented in figure 24. The main surface ocean circulation is mapped with the high values in the Canadian Basin, representing the anticyclonic circulation of the Beaufort Gyre (BG), and the lower values in the Greenland and Norwegian Seas extending all the way north of Russia.

The University of Washington (UW) coupled ice-ocean model of the dynamic topography (see section 4.2.2) is shown in figure 25. The UW model is provided as monthly averages and here is used weighted means to match the ICESat periods. The dynamic topography observed from ICESat and the UW model have different reference levels, but the scales are given within the same interval (60 cm).

Interannual variations are seen in both the ICESat and the UW dynamic topography. The

February - March BG is strongest in 2007 and weakest in 2005. A weak BG is associated with positive Arctic Oscillation (AO) index, whereas a strong BG is associated with negative AO index (see section 2.5.1). The December - March AO index in 2007 is relative high and positive (+1.2), whereas the lowest negative AO index (-0.75) is found in 2006 (see figure 5). The AO indicies in the intervening period (2003 - 2005) are relatively small (less than 0.5) and fluctuate around zero. Thus, the strong BG in 2007 and the weak BG in 2005 can in this case not be explained by changes in the AO index. However, the variations of the BG are identical in both the ICESat and the UW dynamic topography. Further analysis of the relationship between the strength of the BG from the AO index and the dynamic topography is without the scope of this study.

The BG in October - November is stronger in 2005 than the BG in 2003 for both the ICESat and the UW dynamic topography. However, the inter-seasonal variations of the dynamic topography between February - March and October - November are not identical. These discrepancies can, in principle, be caused by the biases introduced by the "lowest-level" filtering method, where special precaution has to be taken when comparing inter-seasonal results (see section 6.2.2).

In general, the dynamic topography from ICESat shows reasonable comparison with the UW modelled dynamic topography and the potential of determination of dynamic topography from satellites are therefore highlighted. The ability to map changes in the dynamic topography from satellite altimetry and thus the underlying ocean circulation, provides new constraints on oceanographic models in the Arctic, especially with improved dynamic topography from future satellite missions like CryoSat-2. This could again provide insight into the basal melting process of the sea ice, since the changing inflow of Atlantic and Pacific waters is believed to be a major source of currently observed sea ice thickness changes (see section 2.5).

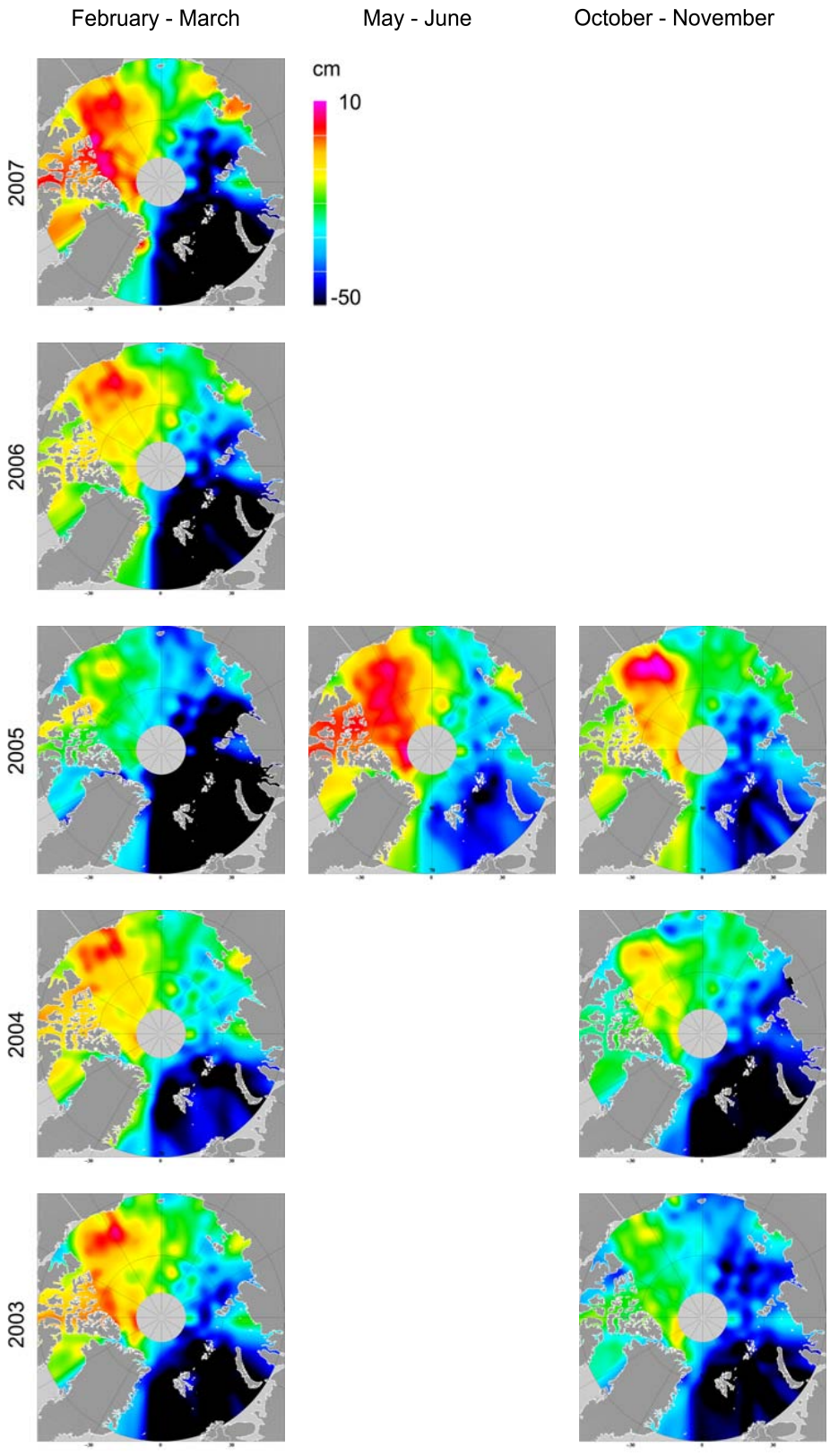

Figure 24: Ocean dynamic topography from ICESat altimetry data.

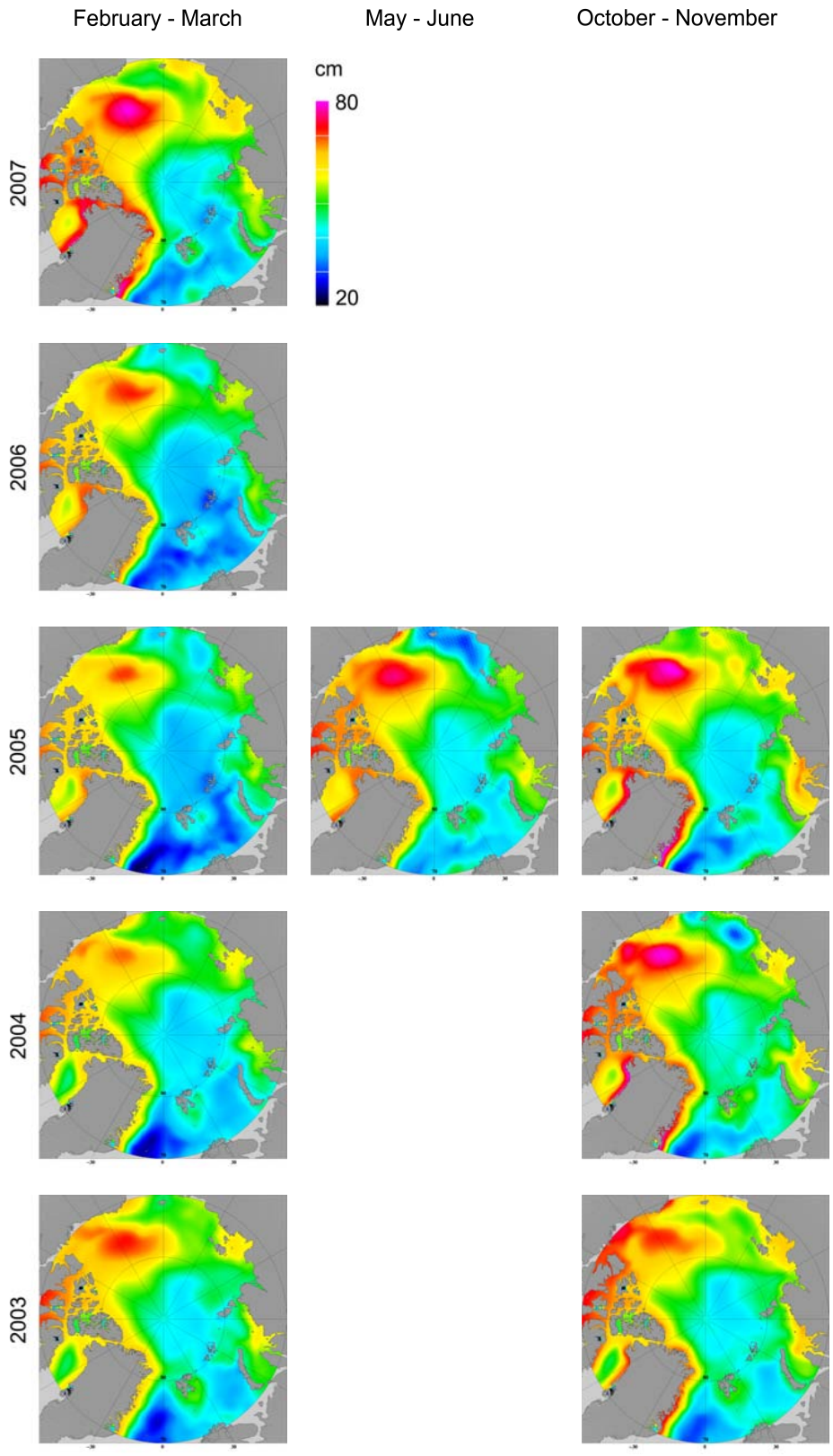

Figure 25: Ocean dynamic topography from coupled ocean-ice model from University of Washington.

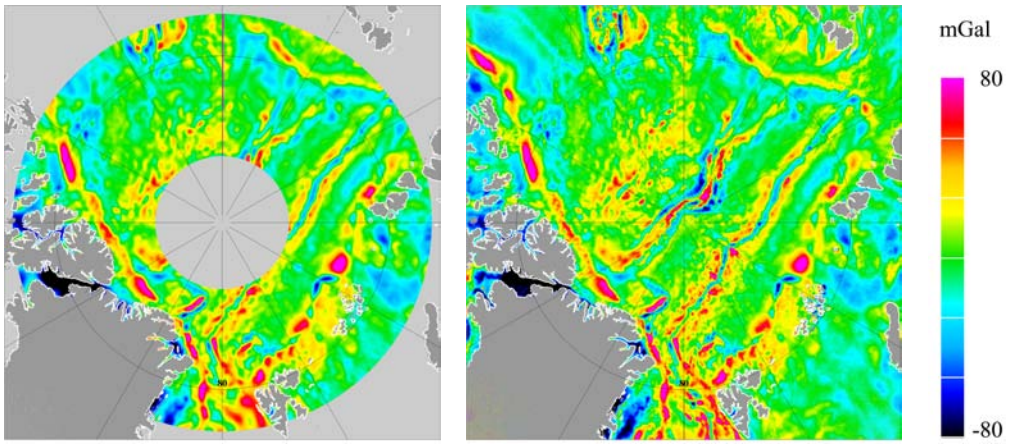

(a) ICESat 2003 - 2008 (b) ArcGP 2.0

Figure 26: Gravity free air anomalies in the Arctic Ocean.

6.4 Gravity anomalies

The gravity anomaly grid based on the ICESat data covering the period 2003 - 2008, is shown in figure 26 (a). The inverted mean sea surface height is corrected for sea ice freeboard heights (see section 5.1). It is in good agreement with the Arctic Gravity Projects (ArcGP) gravity anomalies presented in figure 26 (b) and maps the major tectonic features such as the Gakkel and Lomonosov Ridges, the deep Canadian Basin and the Arctic Margin Gravity High's (AMGHs) at the borders of the continental shelves (McAdoo et al., 2008). See also the bathymetry map of the Arctic figure 1.

6.4.1 Comparison to ArcGP gravity anomalies

Differences between the ICESat and the ArcGP gravity anomalies from three different areas (FA-1, FA-2 and FA-3), is shown in figure 27. FA-3 includes the Gakkel Ridge area, where anomalously large freeboard heights are identified and interpreted as a potential error in the ArcGP gravity field (see section 6.2). The standard deviation (std) is $\sim$ 4 mGal for FA-1 and FA-2, whereas FA-3 is noisier with a standard deviation of 5.4 mGal. However, gravity anomialies in the area FA-3 also have a larger varibility of 20 mGal than the areas FA-1 and FA-2 which have a variability of 13 - 14 mGal.

The ArcGP is primarily based on high precission airborne and submarine gravity measurements of low error statistics (a few mGal) in area FA-1, whereas the areas FA-2 and FA-3 primarily are based on russian on-the-ice gravity measurements associated with larger uncertainties (see figure 14), as there are no information on the actual density of the measurements underlying the ArcGP in these two areas due to Russian data classification.

The larger standard deviation of the differences between the ICESat and ArcGP gravity anomalies for FA-3, together with the less precise data source of the ArcGP indicate, that ICESat data can be used to improve the ArcGP gravity field in this area. However, the differences between the ICESat and the ArcGP gravity anomalies in the area are also a consequence of the different resolutions of the two gravity anomaly data sets. Further

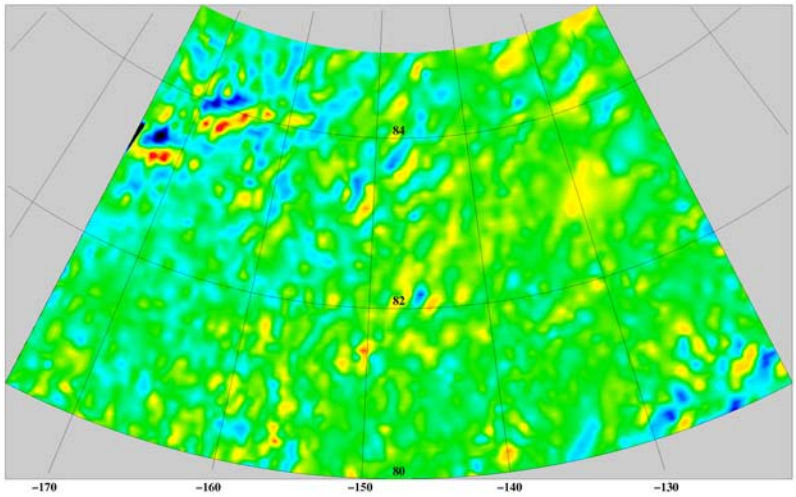

FA-1

Mean: -0.8 mGal
Std: 4.1 mGal

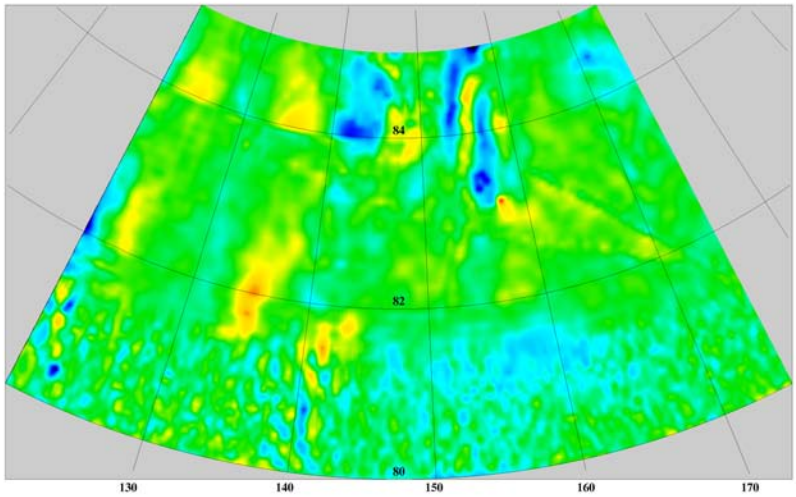

FA-2

Mean: -1.2 mGal
Std: 3.9 mGal

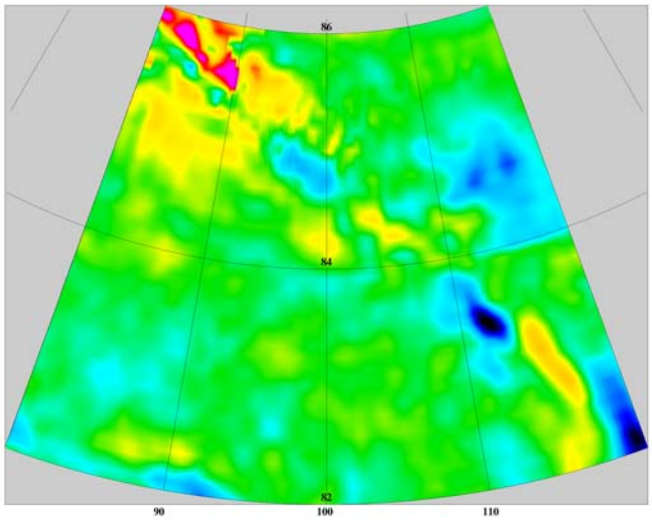

FA-3

Mean: -0.5 mGal
Std: 5.4 mGal

Figure 27: Differences between ICESat and ArcGP gravity anomalies in selected areas.

investigation is needed to conclude whether or not the ICESat gravity anomalies found here perform better than the ArcGP. Such an investigation is, however, beyond the scope of this study.

Overall the accuracy of the ICESat gravity anomalies have improved since the study by McAdoo et al. (2008), in which a comparison of ICESat gravity anomalies from 2003 - 2005 and ArcGP, showed a 12 mGal difference. The better accuracy found in this study, is primarily due to a reduction in the noise from the larger data set used, and is comparable to the 6 - 7 mGal accuracy based on 8 years ERS-2 data (McAdoo et al., 2008).

6.4.2 Comparison to airborne gravity campaigns

A preliminary gravity anomaly field based on ICESat data (release 18) is published in Forsberg and Skourup (2005) including data from 2003 (2 epochs). A more recent gravity field is presented in Skourup et al. (2007a) including data from 2003 - 2005 (7 epochs). The effect of the presence of sea ice is also investigated by comparing the gravity anomaly fields, derived from the mean sea surface not corrected for sea ice freeboard heights (the raw altimeter measurements), to a field corrected for sea ice.

In Skourup et al. (2007a) the three different gravity fields (release 18) are compared to those from high accuracy ($\sim$ 1.5 - 2 mGal) airborne gravity campaigns. The airborne campaigns were carried out by the US Naval Research Laboratory (NRL) in the Arctic Ocean during the years 1992 - 1999 and by the National Space Institute (DTU Space) in the period 1998 - 2003. Four subregions have been selected for the comparison, which are shown in figure 28 by different colours. There are found biases between the 1994 and 1995 survey from NRL data and therefore the data are divided into two subregions.

It is concluded that by including more ICESat epochs the gravity anomalies improve the estimated gravity field, as a consequence of the reduction in noise where most ICESat data is used. In all, but one case north of Greenland (DTU Space 1998 - 2003), the gravity field is improved by correcting the sea surface heights for sea ice freeboard. The area north of Greenland is characterized by very compact thick sea ice with few open leads, introducing biases in the modelled sea surface as discussed in section 6.1.1. These model inaccuracies are believed to introduce the increased errors which are seen in the gravity field north of Greenland. However, the ICESat derived gravity anomalies, including data from 2003 - 2005 and sea ice correction, are comparable to gravity anomalies based on 7 years of ERS data (S. Laxon, pers. comm.).

Table 8 lists the mean and standard deviation of the differences between the ICESat gravity fields and the airborne gravimetry. It is an update of table 2 in Skourup et al. (2007a) to include the newest updated gravity field including ICESat data (release 28) from 2003 - 2008. The bias in the 1994 NRL file is adjusted to match the other NRL data sets. In the 2003 - 2008 gravity field, the ICESat data are corrected for saturation effects and sea ice freeboard heights. Again the accuracy of the fields are improved, except for the area north of Greenland.

The accuracy of the gravity anomalies are related to inaccuracies in the modelled sea surface, especially in heavy ice conditions. The influence of the dynamic topography on the gravity field needs to be investigated, but are hampered by poor models of the oceanographic sea surface (see section 4.2.2). However, the resulting accuracy is comparable to other studies of the gravity fields based on altimetry, found to be 6 - 8 mGal in the Arctic and 3 - 7 mGal over open ocean (see section 3.4.1).

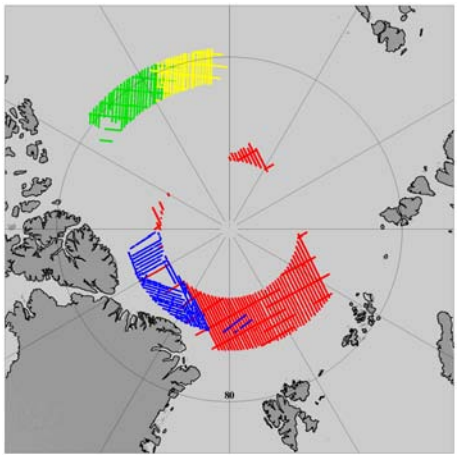

Figure 28: Flight Lines from airborne gravity surveys used for evaluation of the ICESat gravity. The NRL survey 1998 - 1999 north of Svalbard is marked with (red), the DTU Space survey north of Greenland with (blue) and the NRL surveys of 1995 (yellow) and 1994 (green) in the Canadian Arctic.

		NRL 1998 - 1999 red		**DTU Space 1998 - 2003 blue**		**NRL 1995 yellow**		**NRL 1994 green**	
	Epochs	**mean**	**std**	**mean**	**std**	**mean**	**std**	**mean**	**std**
ICESat 2003 - 2007 ice corrected	10	-0.5	4.6	0.5	8.7	3.3	2.8	1.3	9.0
ICESat 2003 - 2005 ice corrected	7	-0.7	4.9	0.7	7.5	3.5	3.8	1.2	9.3
ICESat 2003 - 2005	7	-0.6	5.2	0.5	6.6	3.4	4.2	1.2	9.4
ICESat 2003	2	-1.3	6.4	0.3	7.5	2.4	7.2	0.5	10.9
ERS (Laxon)	-	-	-	-	-	-0.2	3.5	-2.3	9.1

Table 8: Comparison of gravity anomalies derived from ICESat and ERS to airborne gravity campaigns. Units of mean and standard deviation (std) are given in mGal.

6.5 Regional study of geoid accuracy

As discussed in the introduction (section 1.2.2) on-the-ice measurements with geodetic Global Positioning System (GPS) directly measure a combination of the ice surface height, geoid, tides and dynamic topography. Here are included results from an experiment of *in situ* height measurements with GPS done in April 2005 in a fiord system in west Greenland (Skourup and Forsberg, 2008). The results are used to validate geoid models, as well as geoid estimates from ICESat.

The GPS heights were measured on-the-ice. To estimate the geoid height, the sea ice freeboard height, tide and dynamic topography have to be removed from the measurements. The sea ice freeboard height was obtained by drilling at each of the GPS sites and the tide signal was obtained from tide gauge measurements together with long-time (12 - 24 hrs) logging of kinematic GPS. The dynamic topography in the area is assumed to be constant and thus the variations of the sea surface height is an estimate of the geoid undulations according to equation 1 and 2.

In figure 29 the GPS measured sea surface height is compared to two geoid models, the Arctic Gravity Project (ArcGP) and the more regional GOCINA model, as well as the sea surface height derived from ICESat observations.

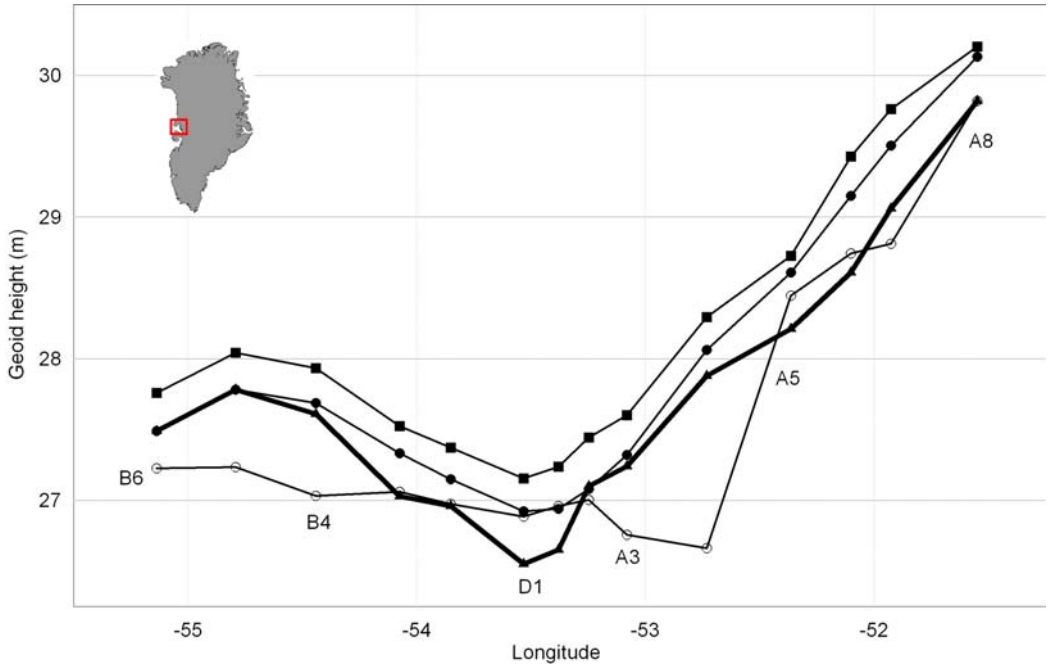

Figure 29: The two lower graphs map the measured sea surface height profile from GPS (thick line) and ICESat (open circles), and the two upper graphs map two geoid models: GOCINA (filled squares) and ArcGP (filled circles). Both geoid models as well as ICESat are converted to WGS-84, allowing comparison to GPS.

The results confirm that it is possible to obtain geoid accuracies of 10 - 20 cm in narrow fiords (Skourup and Forsberg, 2008). The GOCINA geoid model shows better results than the ArcGP geoid model, which is partly explained by the higher resolution of the GOCINA model. In addition, the GOCINA geoid model has a high weighting of surface

data, whereas the ArcGP has a relative high weight to airborne data, which are associated with potential geoid errors related to data biases between different surveys, as well as biases from unknown terrain reductions and downward reduction. The bias of -40 cm between the GPS measurements and the GOCINA geoid model is of the same sign and magnitude, as the dynamic topography from PIPS oceanographic model (see figure 15 (c)).

The ICESat sea surface height shows generally the same trend as the GPS measured values with high values in the east-end of the profile and low values in the west-end, but with large variations along the profile. This can first of all be explained by the limited ICESat tracks available in the area. Second the sea surface height is not corrected for sea ice freeboard heights, due to the lack of open leads in the fast ice covering this area. Last but not the least, the global tide model (GOT99.2) applied to ICESat is based on TOPEX/Poseidon altimetry data, which is not expected to perform well in coastal areas and deep fiord systems (see section 4.2.4).

The GPS measurements can be used to directly measure the tide signal *in situ*, see example in figure 30 (a), where comparison to tide gauge measurements shows that the similarity of tidal phase and amplitudes holds in the fiord system. Figure 30 (b) is an example Arctic Ocean tides measured by a GPS prototype buoy from the GreenArc drifting ice camp north of Greenland, April 2009 (P. Elosegui, pers. comm.). This demonstrate the feasibility of estimating Arctic Ocean tides by drifting GPS buoys to improve existing tide models.

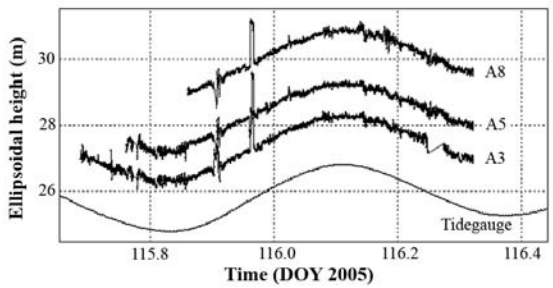

(a) Tide variations from three kinematic GPS points (A3, A5 and A8) along the fiord profile compared to tide gauge measurement.

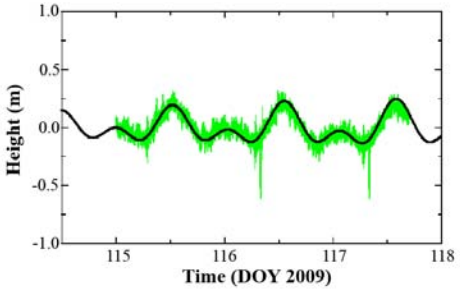

(b) Arctic Ocean tides mesured by GPS (green) and model (black) from the GreenArc drifting ice camp, April 2009 (By courtesy: P. Elosegui).

Figure 30: Tide observations from GPS, tidegauge and model.

6.6 Comparison of freeboard heights from "lowest-level" filtering method and modelled sea surface height

Overall, it has been shown, that it is possible to separate the various height contributions according to equation 6 with reasonable results based on estimation of the sea surface heights from the "lowest-level" filtering method.

The major problem with the method used here, is an underestimation of the sea ice freeboard heights in areas of heavy ice conditions. In addition, there are biases between the different ICESat periods (see section 6.3). These are smaller after the saturation corrections have been applied in the ICESat data release 28, and are expected to become even smaller with the upcomming ICESat data release 29. Last but not the least, there are errors related to the geoid, dynamic topography, atmospheric pressure loading and tide models. In this study, it has not been possible to reach accuracies better than the 20 cm level in freeboard heights, which is, however, a first step in the right direction.

The problem with identification of open water for sea surface reference would be completely overcome if the accuracy of the geoid, tide, atmospheric pressure loading and dynamic topography models were all known with high accuracy. Thus, the sea surface height could simply be modelled according to equation 6. In the following is an example of a comparison of ICESat sea ice freeboard heights estimated by the "lowest-level" filtering method used in this study and sea ice freeboard heights estimated by a sea surface height compiled by models (Renganathan et al., 2009).

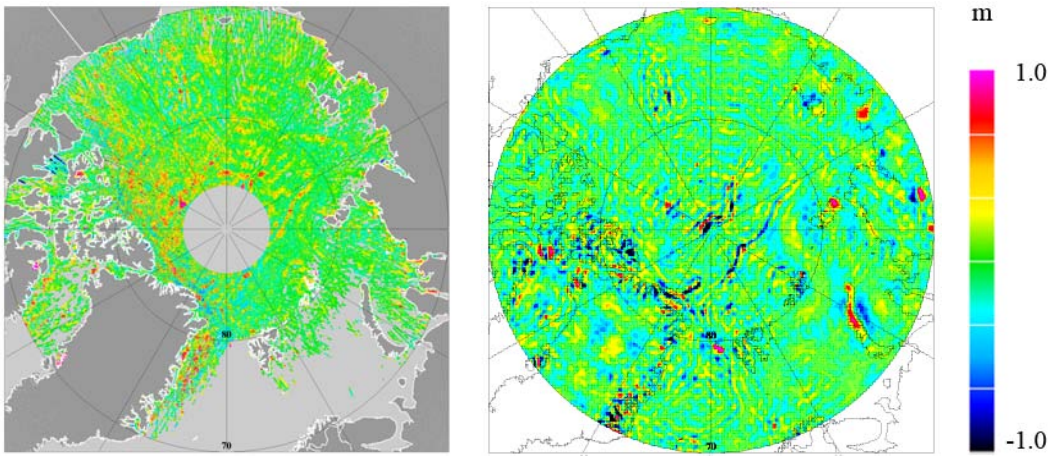

(a) "lowest-level" filtering method versus sea surface height from models

(b) ArcGP 2.0 geoid versus EIGEN-GL04C

Figure 31: Differences between sea ice freeboard heights from different methods and geoid models.

The models used by Renganathan et al. (2009) to model the sea surface height are a combination of the GRACE EIGEN-GL04C geoid model, the UW oceanographic model for the dynamic topography, the AOTIM-5 tide model and the NCEP/NCAR sea level pressure to model the contribution from the atmospheric pressure loading. The differences between the sea ice freeboard heights from ICESat period FM06 by using the "lowest-level" filtering method and by using the geophysical models to model the sea

surface heights, are presented in figure 31 (a). Most of the variations originate from the differences in the geoid models as seen in figure 31 (b). However, in the thicker ice regime north of Greenland, the differences seem to be larger, and could be related to underestimation of the sea ice freeboard heights using the "lowest-level" filtering method.

There is a fundamental problem in defining a cm-level consistent, common reference system for the different quantities in the modelled sea surface height, such as handling of the permanent polar tide systems in the geoid models. The various models of the dynamic topography also need to have a the same zero-level, which are not the case at the time of writing, see section 4.2.2.

There is a bias of 6.6 cm between the mean freeboard heights, with the modelled sea surface height larger (39.8 cm) than the mean freeboard heights found from the "lowest-level" filtering method (33.2 cm). For the same ICESat period Kwok et al. (2007) found mean freeboard heights of 35.0 cm. Whether or not, the differences are a consequence of the "lowest-level" filtering method underestimating the sea ice freeboards, or it is due to inconsistencies in the models, would need a further investigation. This is, however, without the scope of this study. The results based on the modelled sea surface height are promising, and the accuracy of the models will improve in the future, e.g. with the launch of CryoSat-2, see chapter 8.

7 Conclusion

A "lowest-level" filtering method has been applied to ICESat altimetry data from the period 2003 - 2008 to estimate the sea surface heights in the Arctic Ocean. Freeboard heights, dynamic topography and gravity anomalies have been found and presented.

An airborne underflight with high resolution laser scanner of two ICESat ground tracks show, that the "lowest-level" filtering technique applied to ICESat data underestimates the sea ice freeboard heights by up to 37 cm in heavy ice conditions with only a few open leads. The bias is a result of the lower spatial sampling of ICESat and of the averaging of the freeboard across the footprint. This is consistent with results from a similar study made by Kurtz et al. (2008), who found a bias of less than 2 cm, between ICESat freeboard heights and airborne laser freeboard heights, in areas of relative flat ice with many open leads. In areas of thicker ice with fewer open leads they found that the ICESat freeboard heights were underestimated by up to 9 cm. Thus, the biases introduced from the "lowest-level" filtering technique are dependent on sea ice concentration and ice thickness.

The ICESat freeboard heights show geographic variations, which are typical for the Arctic, with thick perennial sea ice north of Greenland forced towards the coast by the Beaufort Gyre and thin seasonal ice in the Russian Arctic. It is shown, that there is a clear spatial correlation between the ICESat freeboard maps and the QuikSCAT backscatter maps, where large sea ice freeboard heights (> 35 cm) are correlated with high backscatter (> -14.5 dB) from thick multiyear sea ice. A decrease in the mean freeboard heights of approximately 10 - 15 cm (corresponding to $\sim$ 70 - 75 cm in thickness) is observed, since the beginning of the ICESat observations in 2003. These are realistic values and can be explained by a combination of a decrease in the perennial sea ice extent together with a general decrease in the ice thickness due to an increased heating of the atmosphere and ocean. Interseasonal comparison should not be performed using the "lowest-level" filtering technique, due the biases introduced in the results from the large interannual variations in sea ice concentration and thickness.

In spite of the freeboard biases, the dynamic topography observed by satellite altimetry shows the main surface circulation in the Arctic with the high values in the Canadian Basin, representing the anticyclonic Beaufort Gyre (BG), and the lower values in the Greenland and Norwegian Seas. A comparison to the oceanographic model from University of Washington show good qualitative agreement with the interannual signal, but not the interseasonal. The variations in the strength of the BG can in this case not be explained by the variation in the Arctic Oscillation index. The direct mapping of ocean dynamic topography by ICESat altimetry and a geoid model can potentially provide validation data for oceanographic models and will improve after the launch of CryoSat-2.

The ICESat laser altimeter provide excellent gravity anomalies comparable to open ocean altimetry even over the most heavy ice conditions. The ICESat derived gravity anomalies compare well to the Arctic Gravity Projects (ArcGP) gravity anomalies and it shows all the major tectonic features. Comparison to airborne gravity surveys of high precision (1.5 - 2 mGal) result in a rms accuracy of 3 - 9 mGal, which are comparable to other altimetry studies of the gravity field in the Arctic and over open ocean. The results of the ICESat derived gravity anomalies can be used to improve existing gravity models in regions with sparse data coverage or data of poor quality. The improved gravity field or geoid can then be used to estimate better sea ice freeboard heights.

8 Future research and altimetry missions

The results presented in this thesis, demonstrates the possibilities to obtain realistic sea ice freeboard heights by use of satellite altimetry. The method also opens up for the possibility to estimate the dynamic topography in ice covered oceans, and thus the underlying geostrophic ocean circulation is mapped. Improved estimates of the dynamic topography could provide insight into the basal melting process of the sea ice, since the changing of Atlantic and Pacific waters is believed to be a major source of currently observed sea ice thickness changes. The ability to map the changes of both sea ice freeboard heights and dynamic topography potentially provide new input to climate- and oceanographic models of the Arctic. This also implies, the importance of long-term monitoring of the changes in the thickness of the sea ice freeboard and ocean heights.

Unfortunately, the end of the ICESat satellite mission will probably occur this year. However, CryoSat-2 is already scheduled to be launched in February, 2010, and a follow-on to ICESat is planned in the 2014 - 2015 time window. To cover the time gap between ICESat and the launch of ICESAT-II, NASA's operation "ICE Bridge" is using aircraft equipped with laser altimetry to monitor height changes in glaciers and ice sheets in the coastal areas of Greenland and Antarctica, as well as the Arctic and Antarctic sea ice cover.

CryoSat-2 will minimize the polar gap to a radius of about 200 km. The satellite will carry a high resolution radar altimeter (SIRAL) with along-track resolution of 100 - 200 m and cross-track resolution of about 1 km. This is much smaller than the resolution of classical altimeters (2 - 10 km) and of dimension smaller than most open leads and ice floes in the Arctic Ocean (Wingham, 1999) .

(a) CryoSat-2 (b) GOCE

Figure 32: ESA's altimetry and gravity satellite missions. Images by courtesy of European Space Agency.

These missions will also improve the models of the geoid and dynamic topography.

Even though the geoid models in the Arctic are known with 10 - 20 cm accuracy, there are still room for improvement of the gravity field, especially in Russian sector of Arctic Ocean. This will be possible by the European Space Agency's (ESA) Gravity field and steady-state Ocean Explorer (GOCE) satellite (launched in March 2009) and by the launch of CryoSat-2. Both missions are expected to determine the geoid with an accuracy of 1 - 2 cm at spatial resolution of 100 - 200 km. However, GOCE is limited by a relative low inclination and only covers to up to 82°N leaving a polar gap of 700 km in radius. The

improved geoid will improve the estimates of the dynamic topography from satellite altimetry, as well as the sea ice freeboard heights.

The upcoming project "Arctic Ocean sea ice and ocean circulation changes using satellite methods" (SATICE) funded by the European Science Foundation (ESF), will deploy a network of GPS buoys in the Arctic. A combination of the GPS- and satellite measurements from CryoSat-2, will provide high precision information on tides, icedrift, as well as the sea surface height. These data are invaluable to validate and improve the accuracy of existing tide models to an order of 1 - 2 cm and the models of the ocean dynamic topography to better than a few cm.

Thus, in the near future it is expected to obtain an accuracy of sea ice freeboard heights from satellite altimetry in the order of $\sim$ 5 cm, corresponding to 30 - 40 cm ice thickness.

References

Abshire, J. B., Sun, X., Riris, H., Sirota, J. M., McGarry, J. F., Palm, S., Yi, D., and Liiva, P. (2005). Geoscience Laser Altimeter System (GLAS) on the ICESat mission: On-orbit measurement performance. *Geophysical Research Letters*, 32(L21S02).

Andersen, O. B. and Knudsen, P. (1998). Global marine gravity field from the ERS-1 and GEOSAT geodetic mission altimetry. *Journal of Geophysical Research*, 103:8129–8137.

Andersen, O. B. and Knudsen, P. (2008). The DNSC08 global mean sea surface and bathymetry. In *EGU-2008*.

Babko, O., Rothrock, A., and Maykut, G. A. (2002). Role of rafting in the mechanical redistribution of sea ice thickness. *Journal of Geophysical Research*, 107(C8):3113.

Beaven, S. G., Lockhart, G., Gogineni, S., Hosseinmostafa, A., Jezek, K., Gow, A., Perovich, D., Fung, A., and Tjuatja, S. (1995). Laboratory measurements of radar backscatter from bare and snow-covered saline ice sheets. *Int. J. Remote Sensing*, 16(5):851–876.

Brenner, A. C., Zwally, H. J., Bentley, C. R., Csatho, B. M., Harding, D. J., Hofton, M. A., Minster, J.-B., Roberts, L., Saba, J. L., Thomas, R. H., and Yi, D. (2003). Geoscience Laser Altimeter System (GLAS) - Derivation of range and range distributions from laser pulse waveform analysis for surface elevations, roughness, slope, and vegetation heights. Algorithm Theoretical Basis Document 4.1.

Chelton, D. B. and McGabe, P. (1985). A review of satellite altimeter measurement of sea surface wind speed: with a proposed new algorithm. *Journal of Geophysical Research*, 90:4707–4720.

Comiso, J., Cavalieri, D. J., and Markus, T. (2003). Sea ice concentration, ice temperature, and snow depth using AMSR-E data. *IEEE Transactions on geoscience and remote sensing*, 41(2):243–252.

Comiso, J., Whadams, P., Krabill, W., Swift, R., Crawford, J., and III, W. T. (1991). Top/bottom multisensor remote sensing of arctic sea ice. *Journal of Geophysical Research*, 96(C2):2693–2709.

Comiso, J. C., Parkinson, C. L., Gersten, R., and Stock, L. (2008). Accelerated decline in the arctic sea ice cover. *Geophysical Research Letters*, 35(L01703).

Connor, L. N., Laxon, S. W., Ridout, A. L., Krabill, W. B., and McAdoo, D. C. (2008). Comparison of ENVISAT radar and airborne laser altimeter measurements over Arctic sea ice. *Remote Sensing of Environment*.

Drinkwater, M. R. (1991). K_u band airborne radar altimeter observations of marginal sea ice during the 1984 Marginal Ice Zone Experiment. *Journal of Geophysical Research*, 96(C3):4555–4572.

Ezraty, R. and Piollé, J. F. (2001). CONVECTION SeaWinds on QuikSCAT Polar Sea Ice Grids. CONVECTION Report 5, IFREMER, Département d'Océanographie Spatiale.

Fetterer, F., Drinkwater, M., Jezek, K., S.W.C.Laxon, Onstott, R., and Ulander, L. (1992). Sea ice altimetry. *Geophysical Monograph*, 68:111–135.

Forsberg, R. and Skourup, H. (2005). Arctic Ocean gravity, geoid and sea ice freeboard heights from ICESat and GRACE. *Geophysical Research Letters*, 32(L21502).

Forsberg, R., Skourup, H., Andersen, O. B., Knudsen, P., Laxon, S. W., Ridout, A., Johannesen, J., Siegismund, F., Drenge, H., Tscherning, C. C., Arabelos, D., Braun, A., and Renganathan, V. (2007). Combination of spaceborne, airborne and in-situ gravity measurements in support of Arctic sea ice thickness mapping. Technical Report 7, Danish National Space Center.

Forsberg, R. and Solheim, D. (1998). Performance of FFT methods in local gravity field modeling. In *Proceedings of Chapman Conference on Progress in the Determination of the Earths Gravity Field*.

Forsberg, R. and Tscherning, C. C. (2008). GRAVSOFT - Geodetic gravity field modelling programs. An overview manual, National Space Institute and University of Copenhagen.

Fricker, H. A., Borsa, A., Minster, B., Carabajal, C., Quinn, K., and Bills, B. (2005). Assesment of ICESat performance at the Salar de Uyuni, Bolivia. *Geophysical Research Letters*, 32(L21S06).

Fu, L. L. and Cazenave, A. (2001). *Satellite Altimetry and Earth Sciences: A Handbook of Techniques and Applications*. Academic Press.

Gascard, J.-C., Festy, J., le Goff, H., Weber, M., Bruemmer, B., Offermann, M., Doble, M., Wadhams, P., Forsberg, R., Hanson, S., Skourup, H., Gerland, S., Nicolaus, M., Metaxian, J.-P., Grangeon, J., Haapala, J., Rinne, E., Haas, C., Heygster, G., , Jakobson, E., Palo, T., Wilkinson, J., Kaleschke, L., Claffey, K., Elder, B., and Bottenheim, J. (2008). Exploring Arctic Transpolar Drift during dramatic sea ice retreat. *EOS, Transactions, American Geophysical Unions*, 89(3).

Giles, K. A. and Hvidegaard, S. M. (2006). Comparison of space borne radar altimetry and airborne laser altimetry over sea ice in the Fram Strait. *Int. J. Remote Sensing*, 27(15):3105–3113.

Giles, K. A., Laxon, S. W., Wingham, D. J., Wallis, D. W., Krabill, W. B., Leuschen, C. J., McAdoo, D., Manizade, S. S., and Raney, R. K. (2007). Combined airborne laser and radar altimeter measurements over the Fram Strait in May 2002. *Remote Sensing of Environment*, 111:182–194.

Haas, C., Pfaffling, A., Hendricks, S., Rabenstein, L., Etienne, J.-L., and Rigor, I. (2008). Reduced ice thickness in arctic transpolar drift favors rapid ice retreat. *Geophysical Research Letters*, 35(L17501).

Hallikainen, M. (1992). Review of the microwave dielectric and extinction properties of sea ice and snow. In *Geoscience and Remote Sensing Symposium, IGARSS '92, International*, volume 2, pages 961–965.

Hanson, S., Stenseng, L., Forsberg, R., Hvidegaard, S. M., and Skourup, H. (2007). A study of snow thickness on first- and multiyear sea ice using laser and radar altimetry. In *EOS Trans. AGU, 88(52), Fall Meeting Suppl., Abstract C11B-0453*.

Hutchings, J., Geiger, C., Roberts, A., Richter-Menge, J., Doble, M., Forsberg, R., Giles, K., Haas, C., Hendricks, S., Khambhamettu, C., Laxon, S., Martin, T., Pruis, M., Thomas, M., Wadhams, P., and Zwally, H. J. (2008). Role of Ice Dynamics in the Sea Ice Mass Balance. *EOS Transactions*, 89:515–516.

Hutchings, J. K. (2007). The Sea ice Experiment: Dynamic Nature of the Arctic (SEDNA). Field Report.

Hvidegaard, S. M. and Forsberg, R. (2002). Sea-ice thickness from airborne laser altimetry over the Arctic Ocean north of Greenland. *Geophysical Research Letters*, 29(20):1952.

Jakobsson, M., Macnab, R., Mayer, L., Anderson, R., Edwards, M., Hatzky, J., Schenke, H. W., and Johnson, P. (2008). An improved bathymetric portrayal of the Arctic Ocean: Implications for ocean modeling and geological, geophysical and oceanographic analyses. *Geophysical Research Letters*, 35(L07602).

Kenyon, S., Forsberg, R., and Coakley, B. (2008). New gravity field for the arctic. *EOS, Transactions, American Geophysical Unions*, 89(32).

Knudsen, P., Andersen, O. B., and Tscherning, C. C. (1992). Altimetric gravity anomalies in the Norwegian-Greenland Sea - Preliminary results form the ERS-1 35 days repeat mission. *Geophysical Research Letters*, 19(17):1795–1798.

Krabill, W. B., Thomas, R. H., Martin, C. F., Swift, R. N., and Frederick, E. B. (1995). Accuracy of airborne laser altimetry over the Greenland icesheet. *Int. J. Remote Sensing*, 16(7):1211–1222.

Kurtz, N. T., Markus, T. M., Cavalieri, D. J., Krabill, W., Sonntag, J. G., and Miller, J. (2008). Comparison of ICESat data with airborne laser altimeter measurements over Arctic sea ice. *IEEE Transaction on Geoscience and Remote Sensing*, 46(7):1913–1924.

Kwok, R. (2004). Annual cycles of multiyear sea ice coverage of the Arctic Ocean: 1999-2003. *Journal of Geophysical Research*, 109(C11004).

Kwok, R., Cunningham, C. F., and Yueh, S. (1999). Area balance of the Arctic Ocean perennial ice zone: October 1996 to April 1997. *Journal of Geophysical Research*, 104(C11):25,747–25,759.

Kwok, R., Cunningham, G. F., Zwally, H. J., and Yi, D. (2006). ICESat over Arctic sea ice: Interpretation of altimetric and reflectivity profiles. *Journal of Geophysical Research*, 111(C06006).

Kwok, R., Cunningham, G. F., Zwally, H. J., and Yi, D. (2007). Ice, Cloud, and land Elevation Satellite (ICESat) over Arctic sea ice: Retrieval of freeboard. *Journal of Geophysical Research*, 112(C12013).

Kwok, R., Zwally, H. J., and Yi, D. (2004). ICESat observations of Arctic sea ice: A first look. *Geophysical Research Letters*, 31(L16401).

Laxon, S. (1994a). Sea ice altimeter processing scheme at the EODC. *Int. J. Remote Sensing*, 15(4):915–924.

Laxon, S. (1994b). Sea ice extent mapping using the ERS-1 radar altimeter. *EARSel Advances in Remote Sensing*, 3(2 - XII):112–116.

Laxon, S. and McAdoo, D. (1994). Arctic Ocean gravity field derived from ERS-1 satellite altimetry. 265(5172):621–624.

Laxon, S., Peacock, N., and Smith, D. (2003). High interannual variability of sea ice thickness in the Arctic region. *Nature*, 425:947–950.

Laxon, S. and Rapley, C. (1987). Radar altimeter data quality flagging. *Advances in Space Research*, 7(11):315–318.

Lindsay, R. W. and Rothrock, D. A. (1995). Arctic sea ice leads from advanced very high resolution radiometer images. *Journal of Geophysical Research*, 100:4533–4544.

Luthcke, S. B., Rowlands, D. D., Carabajal, C. C., Harding, D. J., Bufton, J. L., and Williams, T. A. (2003). ICESat laser altimeter pointing, ranging and timing calibration from integrated residual analysis: A summary of early mission results. In *Proceedings of NASA Flight Mechanics Symposium Conference*.

Markus, T. and Cavalieri, D. (1998). Snow depth distribution over sea ice in the southern ocean from satellite passive microwave data. In Jeffries, M. O., editor, *Antarctic Sea Ice Physical Processes, Interactions and Variability*, volume 74, pages 19–40, Washington, D.C. Antarctic Research Series, AGU.

Maykut, G. A. and Untersteiner, N. (1971). Some results from a time-dependent thermodynamic model of sea ice. *Journal of Geophysical Research*, 76(6):1550–1575.

McAdoo, D. C., Farrell, S. L., Laxon, S. W., Zwally, H. J., Yi, D., and Ridout, A. L. (2008). Arctic ocean gravity field derived from icesat and ers-2 altimetry: Tectonic implications. *Journal of Geophysical Research*, 113.

Morison, J., Steele, M., Kikuchi, T., Falkner, K., and Smethie, W. (2006). Relaxation of central Arctic Ocean hydrography to pre-1990s climatology. *Geophysical Research Letters*, 33(L17604).

Mottram, R., Hanson, S., Kristensen, S. S., Ahlstrøm, A. P., Hvidegaard, S. M., Skourup, H., Sørensen, S. L. S., Nielsen, J. E., and Stenseng, L. (2009). Ice sheet surface and basal topography from radar and lidar, west greenland. Contract report, Danmarks og Grønlands Geologiske undersøgelser.

Nghiem, S. and Neumann, G. (2009). Arctic sea ice change. *IOP Conference Series: Earth and Environmental Science*, 6(012012).

Nghiem, S. V., Chao, Y., Neumann, G., Li, P., Perovich, D. K., Street, T., and Clemente-Colón, P. (2006). Depletion of perennial sea ice in the east arctic ocean. *Geophysical Research Letters*, 33(L17501).

Nghiem, S. V., Rigor, I. G., Perovich, D. K., Clemente-Colón, P., and Weatherly, J. W. (2007). Rapid reduction of arctic perennial sea ice. *Geophysical Research Letters*, 34(L19504).

Overland, J., Walsh, J., and Wang, M. (2008). Atmosphere. Arctic report card, NOAA.

Padman, L. and Erofeeva, S. (2004). A barotropic inverse tidal model for the Arctic Ocean. *Geophysical Research Letters*, 31(L02303).

Pavlis, N. K., Holmes, S. A., Kenyon, S. C., and Factor, J. K. (2008). An Earth Gravitational Model to degree 2160: EGM2008. In *EGU general Assembly 2008*.

Peacock, N. R. and Laxon, S. W. (2004). Sea surface height determination in the Arctic Ocean from ERS altimetry. *Journal of Geophysical Research*, 109.

Perovich, D. K., Grenfell, T. C., Light, B., and Hobbs, P. V. (2002). Seasonal evolution of the albedo of multiyear Arctic sea ice. *Journal of Geophysical Research*, 107(10).

Perovich, D. K., Richter-Menge, J. A., Jones, K. F., and Light, B. (2008). Sunlight, water, and ice: Extreme Arctic sea ice melt during the summer of 2007. *Geophysical Research Letters*, 35(L11501).

Proshutinsky, A., Morison, J., Ashik, I., Carmack, E., Frolov, I., Gascard, J. C., Itoh, M., Krishfield, R., McLaughlin, F., Poluakov, I., Rudels, B., Schauer, U., Shimada, K., Sokolov, V., Steele, M., Timmermans, M.-L., and Toole, J. (2008). Ocean. Arctic report card, NOAA.

Ray, R. D. (1999). A global ocean tide model from TOPEX/Poseidon altimetry: GOT99.2. NASA Technical Memo. 209478, Goddard Space Flight Center.

Renganathan, V., Braun, A., Skourup, H., and Forsberg, R. (2009). Arctic sea ice freeboard heights from ICESat laser altimetry. In *EOS Trans. AGI, 90 (22), Jt. Assem. Suppl., Abstract H31C-06*.

Resti, A., Benveniste, J., Roca, M., Levrini, G., and Johannessen, J. (1999). The ENVISAT Radar Altimeter system (RA-2). *ESA Bulletin*, 98:8.

Richter-Menge, J., Comiso, J., Meier, W., Nghiem, S., and Perovich, D. (2008). Sea ice cover. Arctic report card, NOAA.

Rigor, I. G., Wallace, J. M., and Colony, R. L. (2002). Response of sea ice to the Arctic Oscillation. *Journal of Climate*, 15:2648–2663.

Rothrock, D. A., Percival, D. B., and Wensnahan, M. (2008). The decline in arctic sea-ice thickness: Separating the spatial, annual, and interannual variability in a quarter century of submarine data. *Journal of Geophysical Research*, 113(C05003).

Rothrock, D. A., Yu, Y., and Maykut, G. A. (1999). Thinning of the Arctic Sea-Ice cover. *Geophysical Research Letters*, 26(23):3469–3472.

Rothrock, D. A., Zhang, J., and Yu, Y. (2003). The Arctic ice thickness anomaly of the 1990s: A consistent view from observations and models. *Journal of Geophysical Research*, 108(C3):3083.

Sandwell, D. T. and Smith, W. H. F. (1997). Marine gravity anomaly from GEOSAT and ERS-1 satellite altimetry. *Journal of Geophysical Research*, 102(B5):10,039–10,054. er2008

Schäfer, U., Liebsch, G., Schirmer, U., Ihde, J., Olesen, A. V., Skourup, H., Forsberg, R., and Pflug, H. (2008). Improving gravity field modelling in the German-Danish border region by combining airborne, satellite and terrestial gravity data. In *Proceedings of the International Symposium on Gravity, Geoid and Earth Observation GGEO 2008*, page 6.

Schutz, B., Zwally, H. J., Shuman, C. A., Hancock, D., and DiMarzio, J. P. (2005). Overview of the ICESat mission. *Geophysical Research Letters*, 32(L21S01).

Schwartz, K. P., Sideris, M. G., and Forsberg, R. (1990). The use of FFT techniques in physical geodesy. *Geophysical Journal International*, 100(3):485–514.

Serreze, M. C., Holland, M. M., and Stroeve, J. (2007). Perspectives on the Arctic's shrinking sea ice cover. *Science*, 315:1533–1536.

Shimada, K., Kamoshida, T., Itoh, M., Nishino, S., Carmack, E., McLaughlin, F., Zimmermann, S., and Proshutinsky, A. (2006). Pacific Ocean inflow: Influence on catastrophic reduction of sea ice cover in the Arctic Ocean. *Geophysical Research Letters*, 33(L08605).

Skourup, H. and Forsberg, R. (2006). Sea ice freeboards from ICESat - A comparison to airborne lidar measurements. In Wadhams, P. and Amanatidis, G., editors, *Arctic Sea Ice Thickness: Past, Present and Future*, Brussels. Climate Change and Natural Hazards Series.

Skourup, H. and Forsberg, R. (2008). Geoid, sea level and vertical datum of the Arctic - Improved by ICESat and GRACE. *GEOMATICA*, 62(2):287–298.

Skourup, H., Forsberg, R., and Braun, A. (2007a). Gravity anomalies and sea ice thickness in the Arctic Ocean from ICESat. In Dergisi, H., editor, *Proceedings, Gravity Field of the Earth - 1st meeting of the International Gravity Field Service*, volume 73, pages 242–247, Ankara.

Skourup, H., Forsberg, R., Hanson, S., Hvidegaard, S. M., and Stenseng, L. (2007b). Sea ice freeboards and snow depths in the Arctic based on satellite laser and radar altimetry. In *EOS Trans. AGU, 88(52), Fall Meeting Suppl., Abstract C23B-06*.

Skourup, H., Forsberg, R., Sørensen, S. L. S., Andersen, C. J., Schäfer, U., Liebsch, G., Ihde, J., and Schirmer, U. (2008). Strengthening the vertical reference in the southern Baltic Sea by airborne gravimetry. In *Proceedings of the XXIV IUGG General Assembly*.

Steele, M. and Boyd, T. (1998). Retreat of the cold halocline layer in the Arctic Ocean. *Journal of Geophysical Research*, 103(C5):10419–10435.

Steele, M., Ermold, W., and Zhang, J. (2008). Arctic Ocean surface warming trends over the past 100 years. *Geophysical Research Letters*, 35(L02614).

Steele, M., Morison, J., Ermold, W., Rigor, I., Ortmeyer, M., and Shimada, K. (2004). Circulation of summer Pacific halocline water in the Arctic Ocean. *Journal of Geophysical Research*, 109(C02027).

Stenseng, L., Hvidegaard, S. M., Skourup, H., Forsberg, R., Andersen, C. J., Hanson, S., Cullen, R., and Helm, V. (2007). Airborne lidar and radar measurements in and around Greenland, CryoVEx 2006. Technical Report 9, Danish National Space Center.

Strawbridge, F. and Laxon, S. (1994). Ers-1 altimeter fast delivery data quality flagging over land surfaces. *Geophysical Research Letters*, 21(18):1995–1998.

Tapley, B. D., Bettadpur, S., Ries, J. C., Thompson, P. F., and Watkins, M. M. (2004). GRACE Measurements of mass variability in the Earth system. 305:503–505.

Tonboe, R., Andersen, S., and Pedersen, L. T. (2006). Simulation of Ku-band radar altimeter sea ice effective scattering surface. *IEEE Geoscience and Remote Sensing Letters*, 3(2):237–240.

Tucker III, W. B. and Weatherly, J. W. (2001). Evidence for rapid thinning of sea ice in the western Arctic Ocean at the end of the 1980s. *Geophysical Research Letters*, 28(14):2851–2854.

Ulaby, F. T., Moore, R., and Fung, A. (1982). *Microwave Remote Sensing*, volume II: Radar Remote Sensing and Surface Scattering Theory. Artech House Int.

Ulander, L. M. and Carlström, A. (1991). Radar backscatter signatures of Baltic sea ice. In *Proceedings of the IGARSS'91*, pages 1215–1218. European Space Agency.

Ulander, L. M. H. (1987). Interpretation of SEASAT radar-altimeter data over sea ice using near-simultaneous SAR imagery. *Int. J. Remote Sensing*, 8(11):1679–1686.

Wadhams, P. and Davis, N. R. (2000). Further evidence of ice thinning in the Arctic Ocean. *Geophysical Research Letters*, 27(24):3973–3975.

Wadhams, P. and Horne, R. J. (1980). An analysis of ice profiles obtained by submarine sonar in the Beaufort Sea. *Journal of Glaciology*, 25(93):401–424.

Wadhams, P., III, W. T., Krabill, W., Swift, R., Comiso, J., and Davis, N. (1992). Relationship between sea ice freeboard and draft in the Arctic Basin, and implications for ice thickness monitoring. *Journal of Geophysical Research*, 97(C12):20,325–20,334.

Warren, S. G., Rigor, I., Untersteiner, N., Radionov, V. F., Bryazgin, N. N., Alesandrov, Y., and Colony, R. (1999). Snow depth on arctic sea ice. *Journal of Climate*, 12:1814–1829.

Wingham, D. (1999). CryoSat: Science and mission requirements. Technical report, University College London, Department of Space & Climate Physics, 17-19 Gordon St., London WC1H 0AH.

World Meteorological Organization (1970) (1970). WMO Sea-ice nomenclature. TP 145 259, World Meteorological Organization.

Zhang, J. and Rothrock, D. A. (2003). Modeling global sea ice with a thickness and enthalpy distribution model in generalized curvilinear coordinates. *Monthly Weather Review*, 131(5):681–697.

Zhang, J., Rothrock, D. A., and Steele, M. (1998). Warming of the Arctic Ocean by a strengthened Atlantic inflow: Model results. *Geophysical Research Letters*, 25(10):1745–1748.

Zwally, H. J., Schutz, B., Abdalati, W., Abshire, J., Bentley, C., Brenner, A., Bufton, J., Dezio, J., Hancock, D., Harding, D., Herring, T., Minster, B., Quinn, K., Palm, S., Spinhirne, J., and Thomas, R. (2002). ICESat's laser measurements of polar ice, atmosphere, ocean, and land. *Journal of Geodynamics*, 34:405–445.

Zwally, H. J., Yi, D., Kwok, R., and Zhao, Y. (2008). ICESat measurements of sea ice freeboard and estimates of sea ice thickness in the Weddell Sea. *Journal of Geophysical Research*, 113(C02S15).

A ICESat freeboard and QuikSCAT backscatter maps

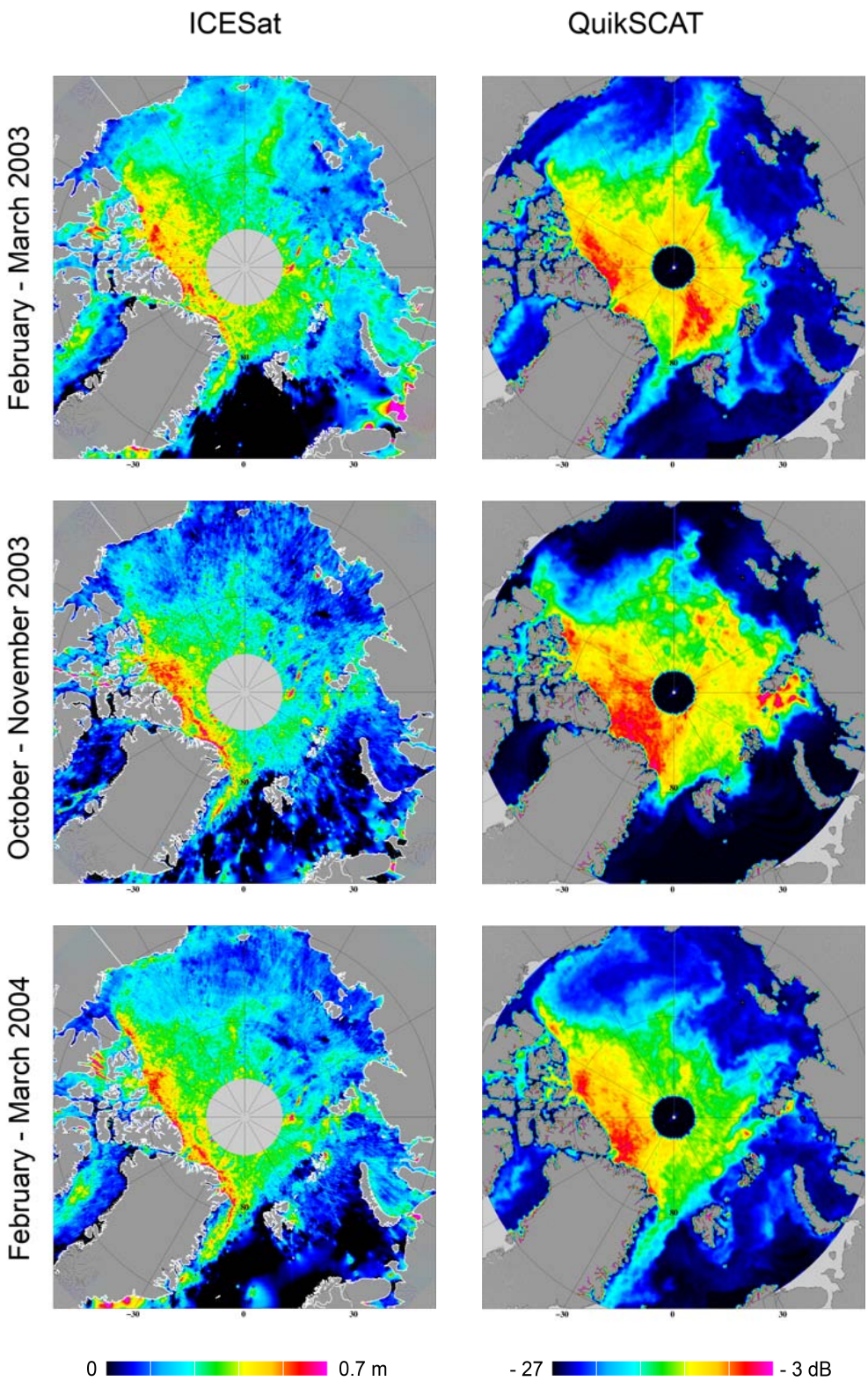

Figure 33: Sea ice freeboard maps from ICESat (left column) and QuikSCAT backscatter maps (right column).

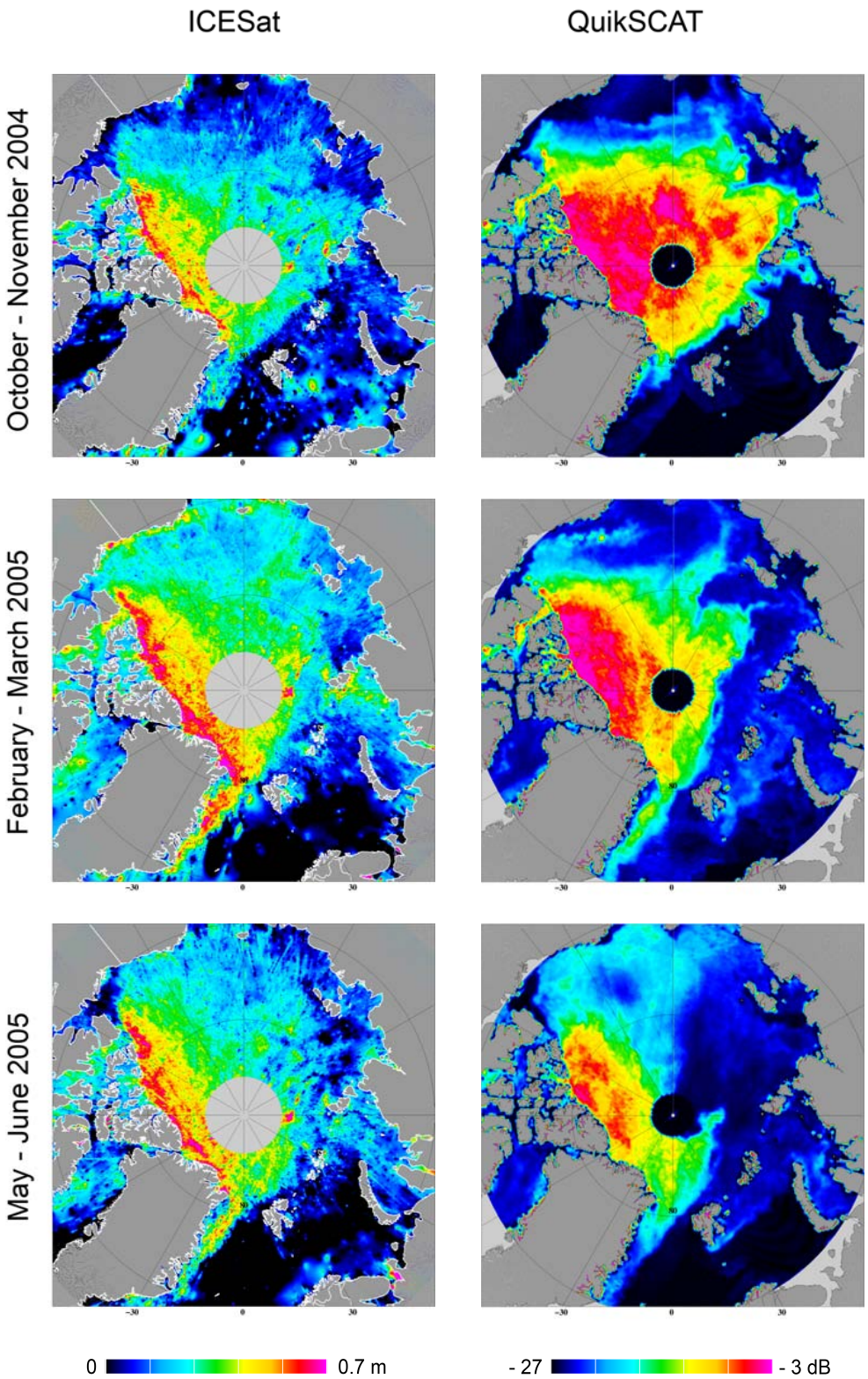

Figure 34: Sea ice freeboard maps from ICESat (left column) and QuikSCAT backscatter maps (right column).

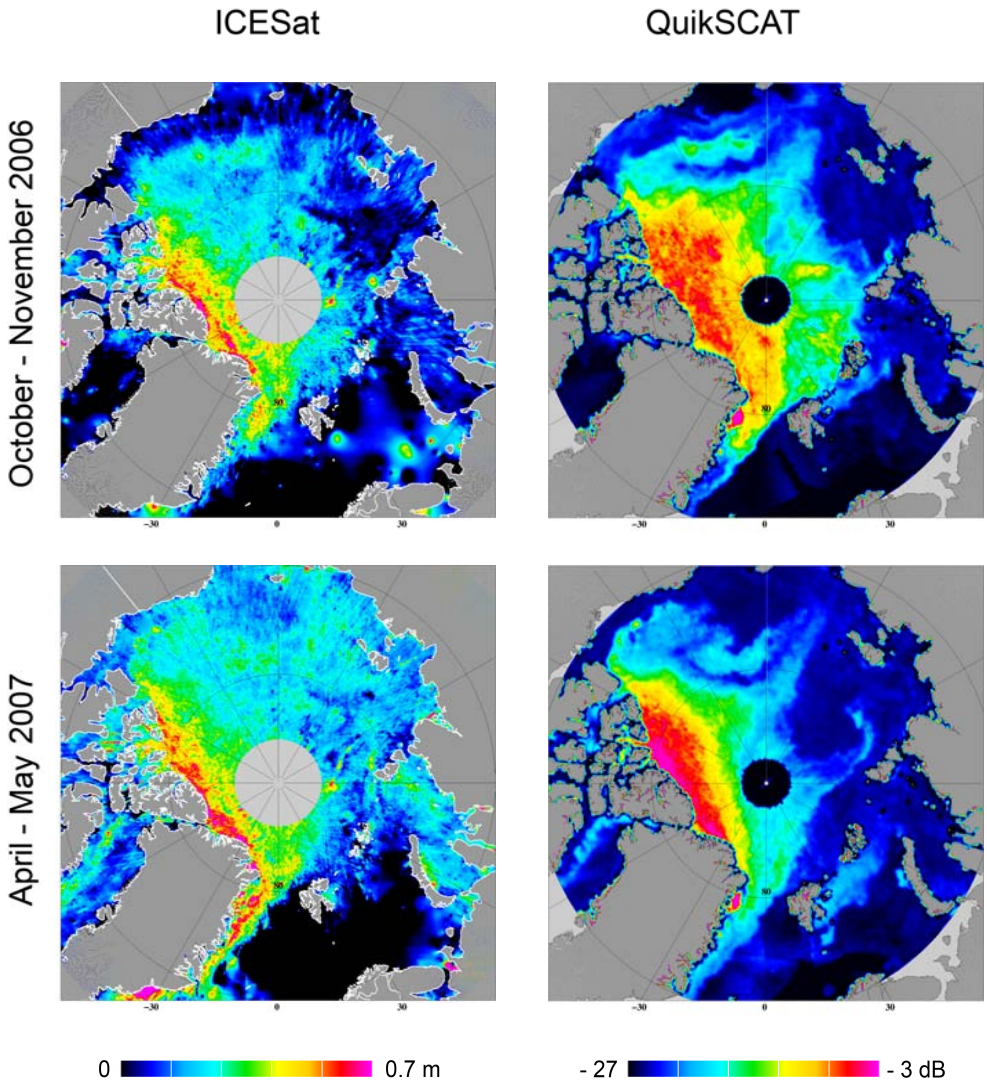

Figure 35: Sea ice freeboard maps from ICESat (left column) and QuikSCAT backscatter maps (right column).

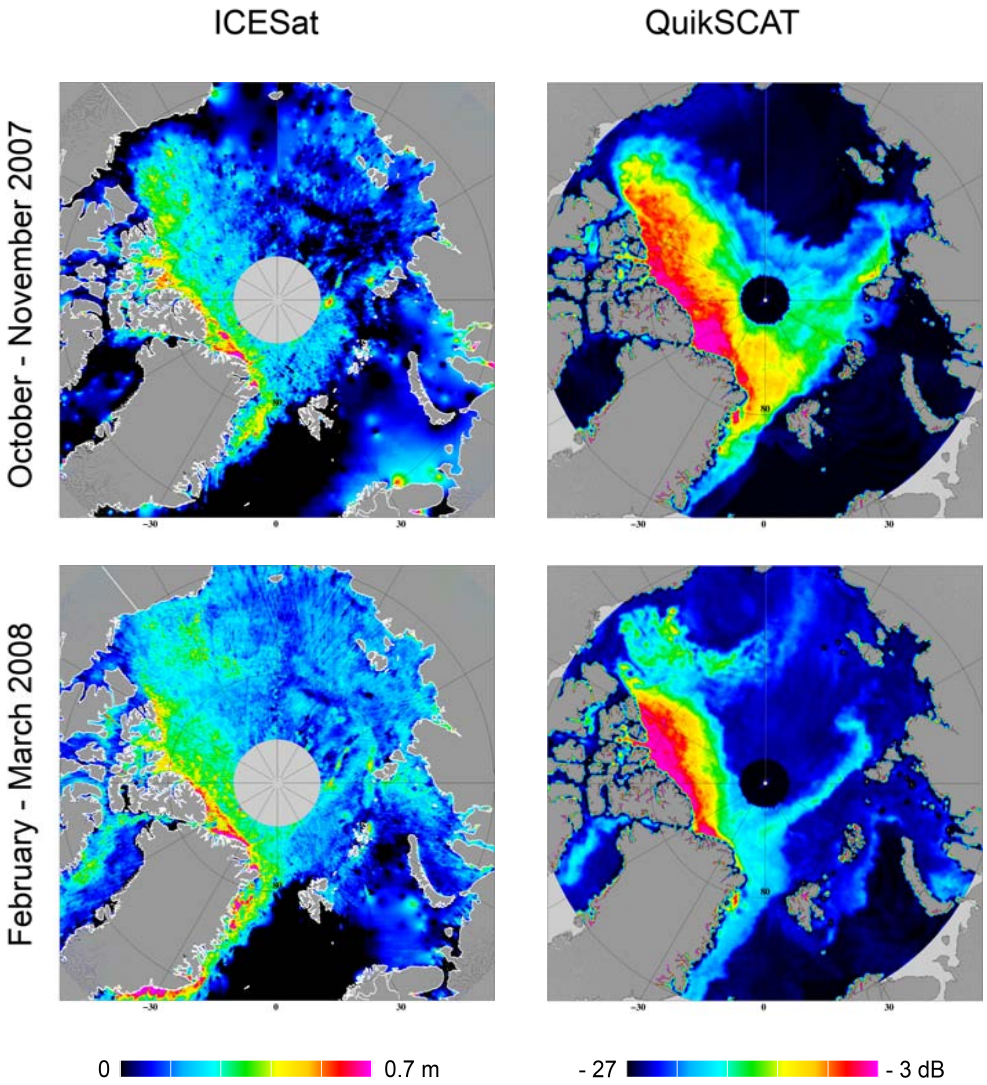

Figure 36: Sea ice freeboard maps from ICESat (left column) and QuikSCAT backscatter maps (right column).

B ICESat freeboard maps - release 18

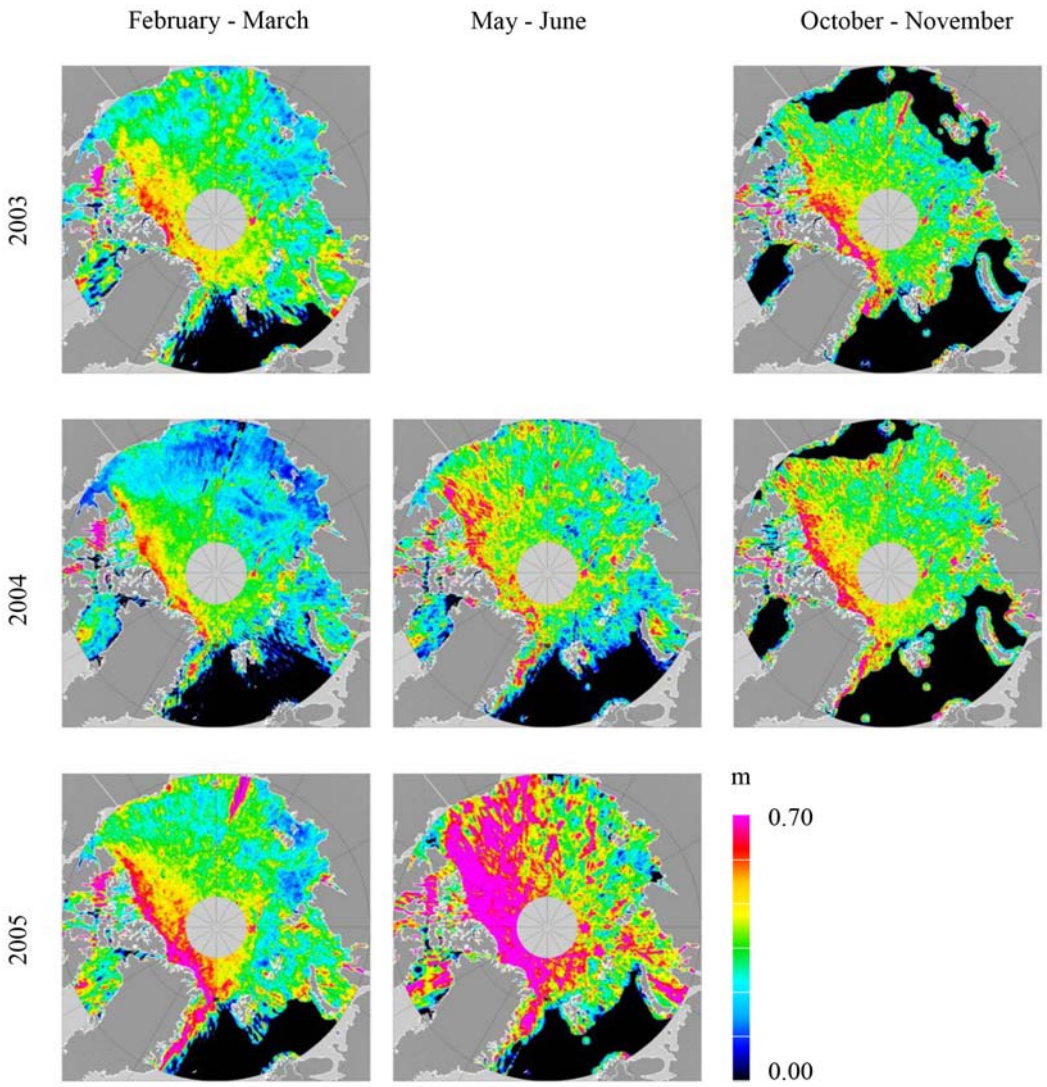

Figure 37: Sea ice freeboard maps from ICESat data release 18.

C QuikSCAT sea ice and open ocean mask

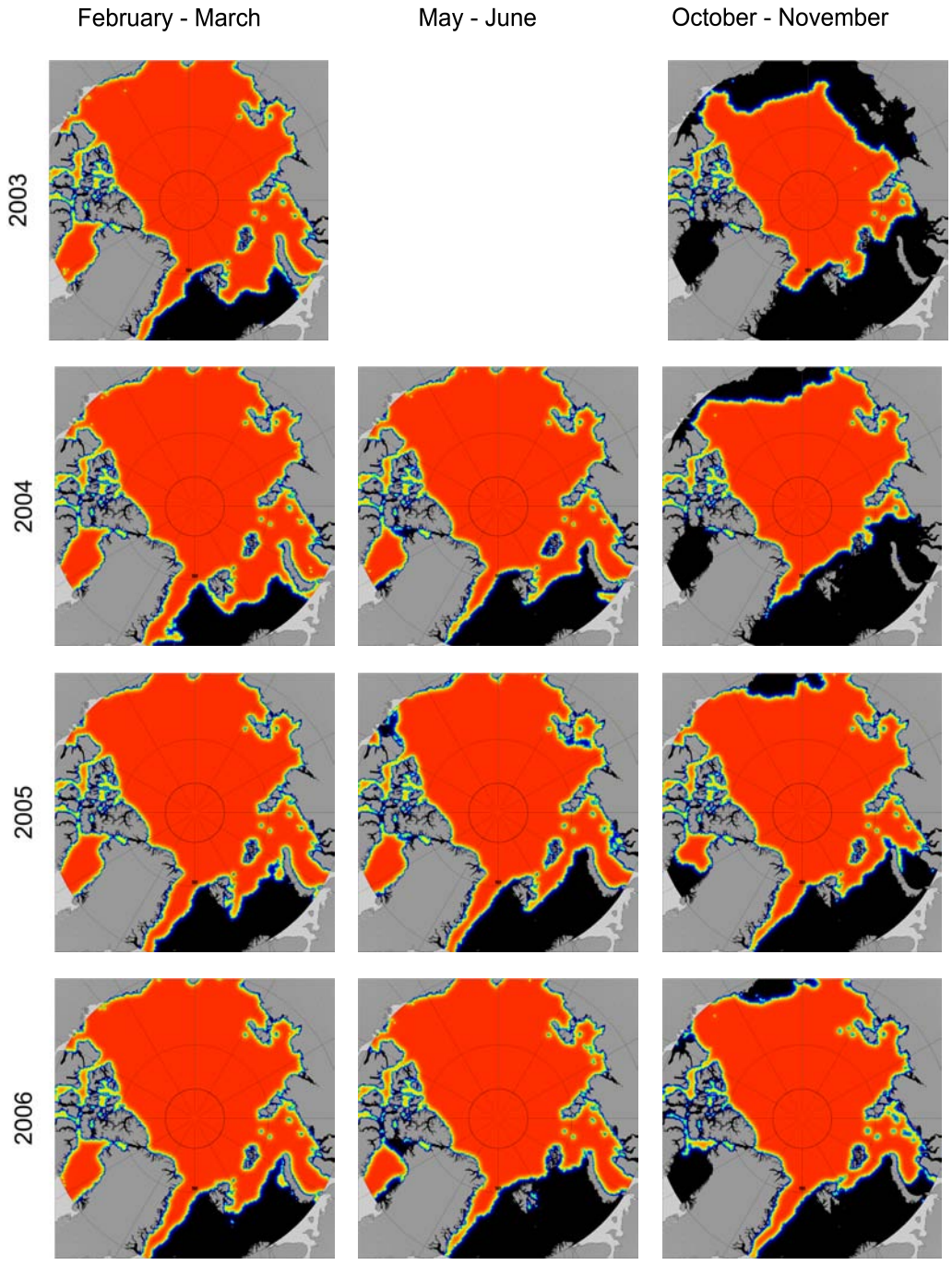

Figure 38: QuikSCAT sea ice (red) and open ocean (black) mask.

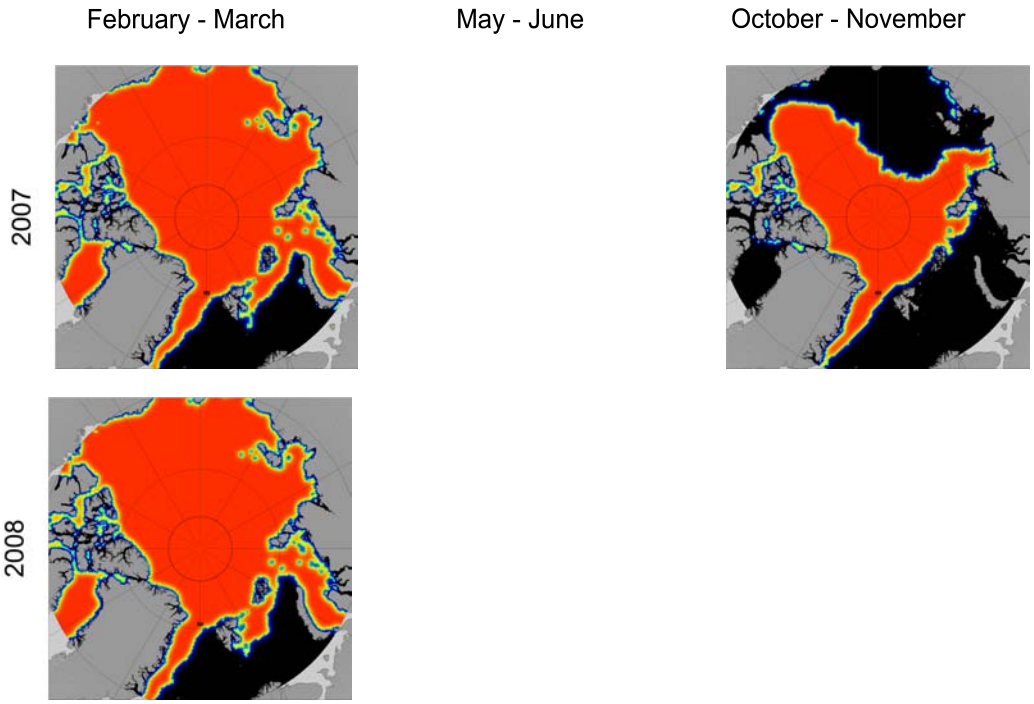

Figure 39: QuikSCAT sea ice (red) and open ocean (black) mask.

D ICESat underflight - Beaufort Sea

As part of the National Space Institute (DTU Space) airborne field campaign in the spring of 2007, an extensive survey was done in the area of the APLIS (Applied Physics Laboratory Ice Station) drifting ice camp located in the Beaufort Sea $\sim$ 190 miles north of Prudhoe Bay, Alaska. The ice camp was established on April 1, and dismantled on April 16.

The overall main objective of the SEDNA (The Sea ice Experiment: Dynamic Nature of the Arctic) project based out of APLIS was to monitor the ice mass balance. This can be done by monitoring the evolution of the thickness distribution of the ice cover through thermodynamic ice growth and melt, as well as dynamic redistribution through formation of leads ridging and rafting (see section 2.1).

The sea ice in the area around APLIS was measured by multiple techniques to get the thickness distribution. *In situ* measurements included ice and snow thickness measurements by drilling and by *electromagnetic induction* (EM). The bottom of the ice was measured by *upward looking sonar* (ULS) from submarine and an autonomous underwater vehicle (AUV), as well as by an EM towed by helicopter. The surface of the ice was monitored by altimetry from airplane and satellite (ICESat and ENVISAT). NASA's ICESat team had specially arranged for the spring 2007 ICESat mission to be shifted 16 days later than planned (MA07) in order to measure during the existence of the ice camp.

Collection of the airborne laser scanner data was chosen to be coincident to other ongoing sea ice activities in order to compare the results, giving the opportunity to obtain a deeper insight into various measurement methods and sea ice processes. Of special interest to this study was the underflight of ICESat. The airborne survey was conducted on April 12, 2007, along a 70 km track. A plot of the along-track airborne laser scanner freeboard heights are shown in figure 40, together with the corresponding freeboard distribution. The freeboard heights are in the order of 40 - 70 cm with mean freeboard heights along the track of 59 cm and standard deviation 26 cm.

On the day of the survey the position of the ice camp was approximately 73.2°N and 146.5°W. The ICESat track (number 76) closest to the ice camp was chosen for surveying (see figure 40). Unfortunately, the track was measured by ICESat about a month earlier on March 14. An intercomparison is impossible due to the drift of the sea ice in the intervening period, adressing the importance of careful planning.

However, the laser scanner flights in the area of the ice camp turned out to be successful in other ways. The work of comparing high resolution AUV measurements to the laser scanner over a ridge is ongoing. This would directly give the conversion factor between freeboard and drafts. For further information on the field work, see the SEDNA field report Hutchings (2007) and Hutchings et al. (2008).

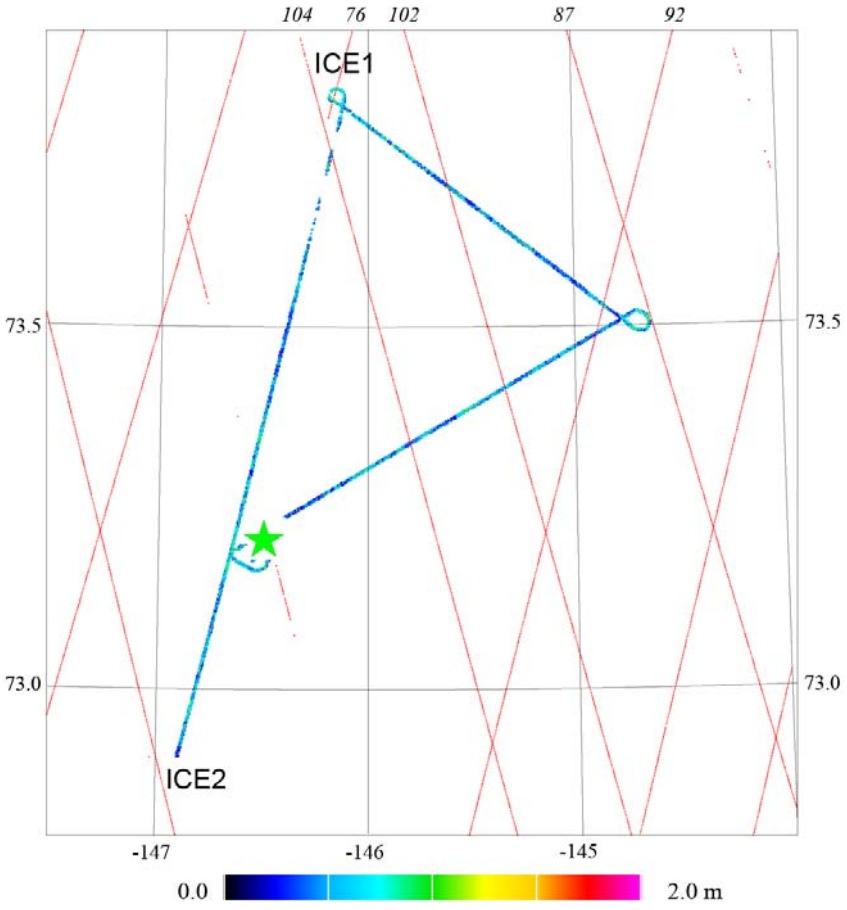

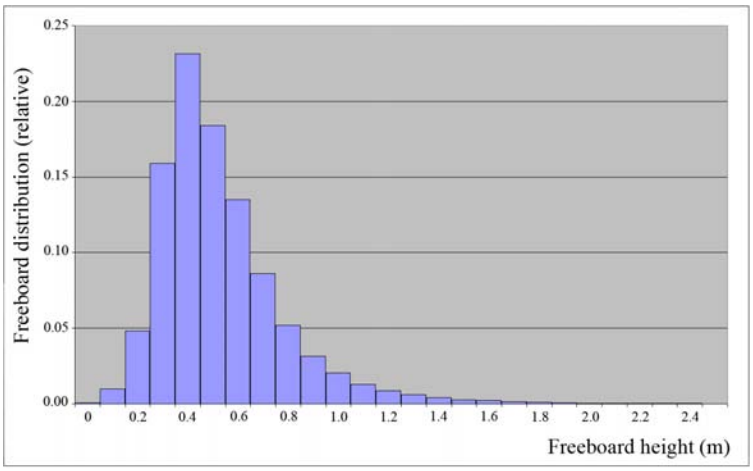

Figure 40: Upper plot: Sea ice freeboard heights measured by airborne laser scanner on April 12, 2007, and the position of APLIS ice camp (green star). ICESat tracks are superimposed (red lines) on the plot with orbit dates labeled along the top of the plot (*italics*) given as number of days since the beginning of the year. Lower plot: Sea ice freeboard distribution from the airborne track ICE1 - ICE2.

E ENVISAT underflight - Fram Strait

In the spring of 2006, as part of the European Space Agency's (ESA) CryoSat Validation Experiment (CryoVEx), the National Space Institute (DTU Space) conducted an airborne survey. The main purpose was to measure the heights of icesheets and glaciers with laser and radar in Greenland, Svalbard and Devon Island, as well as sea ice in the Alert area. For a more detailed description of the field work see Stenseng et al. (2007).

An underflight of ENVISAT (orbit 212, cycle 47) was performed in the Fram Strait on May 2 (Skourup et al., 2007b). For track location see figure 41, where the blue track is the ENVISAT track and the red line the flight track. Usually, the processed ENVISAT waveforms released in the Geophysical Data Record (GDR) are averaged over 100 waveforms to reduce noise and data volume. This results in a smeared along-track resolution of approximately 390 m. On special requests ESA collects the Individual Echoes (IE) giving a higher along-track resolution of 3.9 m, however, the footprint size of each measurement is still in the order of 2 - 10 km nominally. IE of the ENVISAT altimeter was requested from ESA over the study area to achieve the highest along-track resolution. Unfortunately, IE was not recorded along the track of orbit 212, but was provided for small sections along other tracks in the area marked with green stars in figure 41.

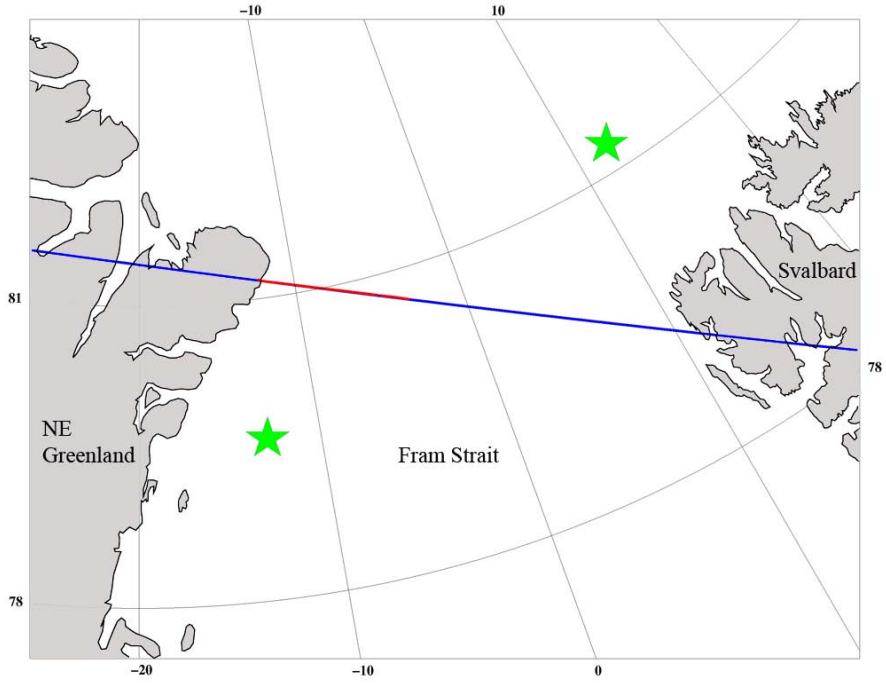

Figure 41: Map of ENVISAT groundtrack (blue) and flight track (red) on May 2, 2006. The positions of available individual echoes (IE) are marked with green stars.

The averaged waveforms along the ENVISAT track are presented in figure 42. Over the ocean is seen the characteristic waveforms from a rough surface. The waveforms from the sea ice covered area show a large variation with typical specular from open leads or very thin ice and the more ocean-like waveforms from ice floes (see section 3.3.1). In order to locate the returns from leads within the ice cover (peaked signals) the Pulse Peakiness (PP)

parameter is defined.

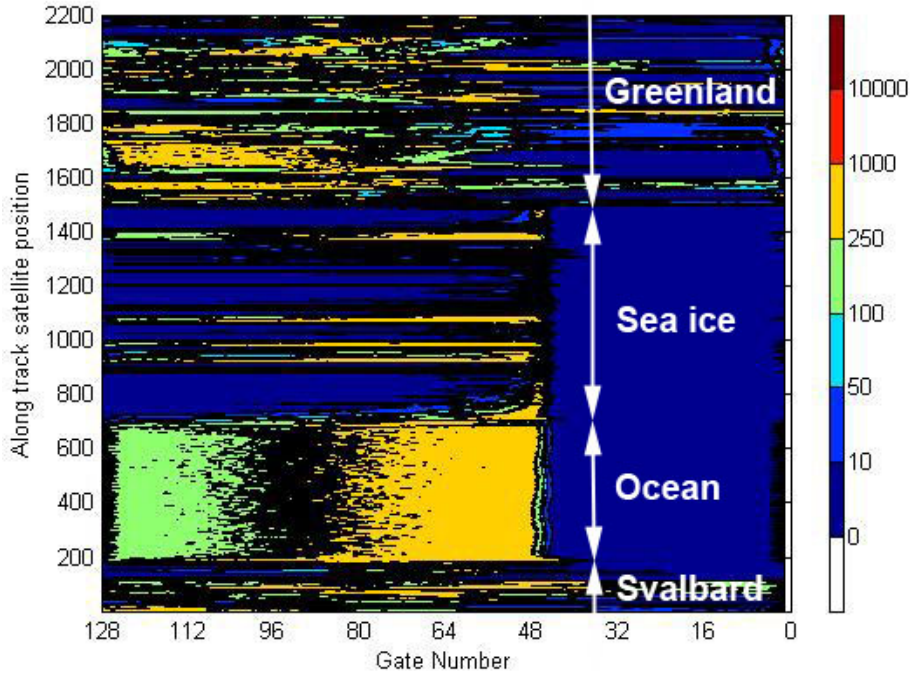

Figure 42: Averaged waveforms along ENVISAT track 212. The color scales represent the strength of the return signal.

E.1 The Pulse Peakiness Parameter

The pulse peakiness (PP) depends only on the waveform and is a estimate of the peakiness of the waveform. It was introduced by Laxon and Rapley (1987) to permit filtering of anomalous data over open ocean, including sea ice. Assuming the waveform is roughly centered at the *tracking point* in the range window (bin 44.5 for ENVISAT), PP is effectively a measure of the ratio of the peak power to the average power in the waveform. Thus, a high PP value represents a specular return and a low PP value represents a diffuse return.

For ENVISAT PP is given by

$$PP = \frac{44.5 \cdot P_{max}}{\sum_{i=10}^{128} P_i} \tag{14}$$

where P_{max} is the peak power and P_i the power in the i'th bin of the range window. The first ten bins are excluded since they contain aliased power.

Originally PP was used to filter data over open ocean using PP=1 as a limit, although noise, resulting from speckle in the altimeter return, results in a value closer to 1.5 (Laxon and Rapley, 1987). Knudsen et al. (1992) used PP less than 1.7 to remove sea ice. Strawbridge and Laxon (1994) use PP for quality flagging over land surfaces, where the altimeter is likely to loose track (keeping the *tracking point* in the range window). By

accepting values of PP $\geq$ 1.1, up to 43% of poorly tracked data is removed, with only 4.3% loss of good data. The first to propose the use of PP for sea ice applications was Laxon (1994a).

In this small study waveforms with a peakiness of less than or equal to 1.8 is processed as diffuse (originating from either open ocean or ice floe surfaces) and those with a peakiness greater than 1.8 is processed as specular (Peacock and Laxon, 2004).

E.2 Results

In figure 43 is presented the ENVISAT residual heights (h_r) after removing effects from tides, atmospheric pressure loading and a geoid model from the ENVISAT measurements (see section 5.1.2). It is seen that most of the ENVISAT observations are classified as peaked signals (black triangles) from leads of open water or very thin ice. This is expected in the Fram Strait, where there are very few ice floes larger than the ENVISAT footprint, due to the dynamic of the area. The whole footprint has to be inside a floe to get a waveform classified as a return from a rough surface, this is because if only 0.1% of the footprint covers a flat surface, the system locks on the flat surface. The anomalous low values in the residual heights are from snagging events, where the waveform locks on the lead. Due to the few measurements from sea ice, further analysis is not performed.

This will most likely be solved with the refined technique onboard CryoSat SIRAL radar altimeter, where the along-track resolution is $\sim$ 250 m, which is less than the size of most ice floes in the Artic Ocean (Wingham, 1999).

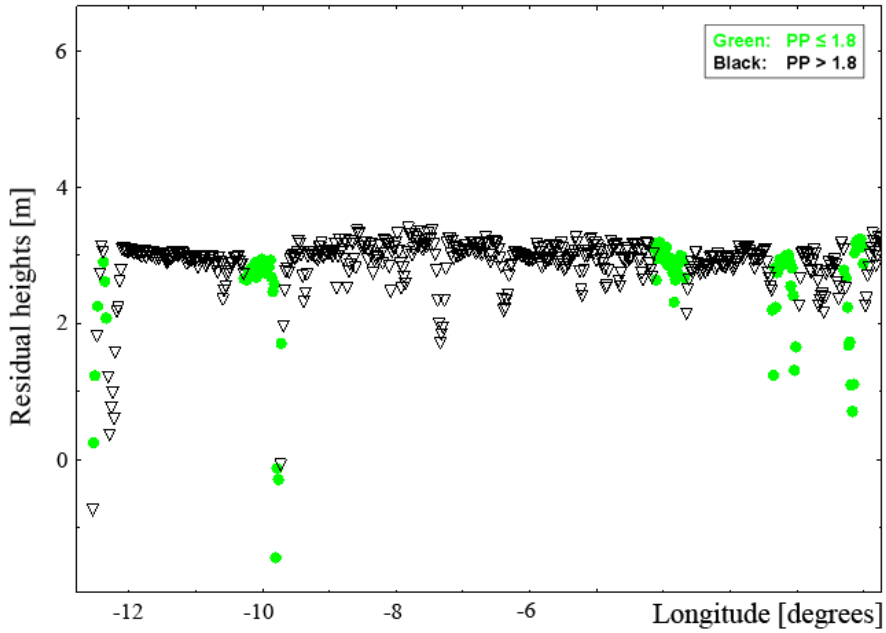

Figure 43: Residual heights (h_r) from ENVISAT observations. Black triangles represent peaked signals (PP > 1.8) from open leads and green dots represent diffuse signals from sea ice (PP $\leq$ 1.8).

F Programs

Here the two main programs, programmed and used in this thesis, are enclosed. These includes:

- The program to read ICESat data and to perform the filtering and corrections according to section 4.1.2 (Readglas 13)
- The program to find the sea surface height using the "lowest-level" filtering algorithm (LLF3Glas)

```
      program readglas
ccccccccccccccccccccccccccccccccccccccccccccccccccccccccccccccccc
c
c                     R E A D G L A S
c
c  Program reads ICESat data records GLA13
c  Input:
c         glas file name
c         outfile
c         tjd1 tjd2 rlat1 rlat2 rlon1 rlon2 lave
c
c  where  tjd1,tjd2 ... time interval in jd
c         rlat1,rlat2,rlon1,rlon2 ... geographic area
c         lave ... true for 1-sec averages
c
c  output in gravsoft format with average h,hmin/geoid,avruf
c  ldos must be set false for unix systems
c
c  (c) Rene Forsberg, KMS/Denmark, dec 2003
c  Henriette Skourup, corrections made to GLA13 Release 28, dec 2008
c
ccccccccccccccccccccccccccccccccccccccccccccccccccccccccccccccccc
      implicit double precision(a-h,o-z)

      character*72 ifile,ofile
      integer*1 b(6760)

      double precision i_lat,i_lon,i_elev,i_gdHt,i_ocElv,
     .          i_satElevCorr,i_reflctUncorr,i_SeaIceVar,i_gval_rcv
     .          ,i_ocElv1,i_ocElv2,ellipsoidHt
      integer   i_rec_ndx,i_satNdx,iday

      integer*2 i_AttFlg1,i_sigmaatt,i_rngCorrFlg

      integer*1 i_ElvuseFlg(5),i_ElvuseFlg_Bits,i_satCorrFlg,i_numPk,
     .          oceansweep0,oceansweep1,oceansweep2,oceansweep3,
     .          oceansweep4,oceansweepIST,oceansweepGYRO,oceansweepLRS

      integer   nrej1,nrej2,nrej3,nrej4,nrej5,nrej6,nrej7,nrej8,nrej9,
     .          nrej10,nrej11,nrej12,nrej13,oc0,oc1

      logical   ldos,lave
      common    /rec/ b,ldos
c  --------------------


      read(*,'(a)') ifile
      read(*,'(a)') ofile
      read(*,*) tjd1,tjd2,rlat1,rlat2,rlon1,rlon2,lave
      open(10,file=ifile,access='direct',form='unformatted',
     .recl=6760)
      open(20,file=ofile,status='unknown')
      write(*,*) 'READGLAS ',ifile

c  ldos: true for windows, reverse byte order
c  gtol: tolerance for rejection by geoid
c  --------------------
      ldos = .true.
      gtol = 9999.0
      ellipsoidHt = 0.7

      radeg = 180.d0/3.1415926536d0
      nrej1 = 0
      nrej2 = 0
      nrej3 = 0
      nrej4 = 0
      nrej5 = 0
      nrej6 = 0
      nrej7 = 0
      nrej8 = 0
      nrej9 = 0
      nrej10 = 0
      nrej11 = 0
      nrej12 = 0
      nrej13 = 0
```



```
      nout = 0

      oc0 = 0
      oc1 = 0


c  loop through records, reading ICESat data into 1D Array b(6760)
c  i1: If ICESat data is used from b directly i1, then 1 has to be applied
c  to the ICESat record, as the b-array starts with 1 and ICESat with 0
c  i2, i4: The ICESat record can be used directly as argument. This is the
c  case as the functions i2, and i4 adds 1 to the argument
c  --------------------

      irec = 4
10    read(10,rec=irec,err=80) b
      i_rec_ndx = i4(0)

c  TIME:
c  tjd is the time given in decimal days of the 1st shot in the 1 second
c  frame referenced to ICESat timesystem (J2000) January 1, 2000 at noon
c  --------------------
      iutc = i4(4)
      rutc = i4(8)*1.d-6
      tjd = (iutc+rutc)/86400.d0

      if (irec.eq.4)
     .write(*,*) 'first rec: no,utc,jd = ',i_rec_ndx,iutc,tjd

c  The geoid (i_gdHT) and oceantides (i_ocElv)  are only given for the first
c  and last shot - the average is taken and used for all 40 shots in the record
c  --------------------
      i_gdHt = 1.d-2*(i2(2676)+i2(2678))/2.
      i_ocElv = 1.d-3*(i2(2700)+i2(2702))/2.
      i_ocElv1 = 1.d-3*i2(2700)
      i_ocElv2 = 1.d-3*i2(2702)
      i_rngCorrFlg = i2(5212)

      i_AttFlg1 = i2(5224)

      j0 = 0
      iave = 0
      sumlat = 0
      sumlon = 0
      sumt = 0
      sumelev = 0
      sumrefl = 0
      sumruf = 0
      elevmin = 999

      do j = 1,40
        t = tjd
        if (j.gt.1) t = tjd + i4(20+(j0-4))*1.d-6/86400.d0

        i_lat = i4(176+j0)*1.d-6
        i_lon = i4(336+j0)*1.d-6
        if (i_lon.gt.180) i_lon = i_lon-360

        i_elev = i4(496+j0)*1.d-3

        i_sigmaatt = i2(2576+j0/2)
        i_reflctUncorr = i4(3752+j0)*1.d-6
        i_numPk = b(4076+1+(j-1))
c       ruf = i2(4276+j0/2)*1.d-2
        i_SeaIceVar = i2(4916+j0/2)
        i_satNdx = b(5348+1+(j-1))
        i_satElevCorr = i2(5388+j0/2)*1.d-3
        i_gval_rcv = i2(5668+j0/2)


c  use elevation flags
c  --------------------
        i_ElvuseFlg(1) = b(4996+1)
        i_ElvuseFlg(2) = b(4996+2)
        i_ElvuseFlg(3) = b(4996+3)
        i_ElvuseFlg(4) = b(4996+4)
        i_ElvuseFlg(5) = b(4996+5)
```

```
        i_ElvuseFlg_Bits = IBITS(i_ElvuseFlg(5-(j-1)/8),mod(j-1,8),1)


c  nadir off-pointing, ocean sweep, etc.
c  ----------------------------
        oceansweep0 = IBITS(i_AttFlg1,0,1)
        oceansweep1 = IBITS(i_AttFlg1,1,1)


c  Saturation correction flags
c  ----------------------------
        i_satCorrFlg = IBITS(b(5468+1+(j-1)),0,4)

        if (i_satCorrFlg.eq.2) then
           i_elev = i_elev + i_satElevCorr
        end if


c  Data rejection criterias
c  ----------------------------
        if (i_ElvuseFlg_Bits.eq.1) then
            nrej1 = nrej1 + 1
        else if (i_lat.lt.rlat1.or.i_lat.gt.rlat2.or
     .  .i_lon.lt.rlon1.or.i_lon.gt.rlon2) then
            nrej2 = nrej2+1
c     .  .or.t.lt.tjd1.or.t.gt.tjd2) then
        else if (oceansweep0.eq.1) then
            nrej3 = nrej3 +1
        else if (oceansweep1.eq.1) then
            nrej4 = nrej4 +1
        else if (i_sigmaatt.ne.0) then
            nrej5 = nrej5 +1
        else if (i_reflctUncorr.gt.1.or.i_reflctUncorr.lt.0) then
            nrej6 = nrej6 + 1
        else if (i_satCorrFlg.gt.2) then
            nrej7 = nrej7 + 1
        else if (i_satNdx.eq.126) then
            nrej8 = nrej8+ 1
        else if (i_SeaIceVar.gt.60) then
            nrej9 = nrej9 +1
        else if (i_gval_rcv.gt.30) then
            nrej10 = nrej10 + 1
        else if (i_numPk.gt.1) then
           nrej11 = nrej11+1
        else if (abs(i_elev-i_gdHt).gt.gtol) then
           nrej12 = nrej12+1
        else if (abs(i_elev).gt.100) then
           nrej13 = nrej13+1
        else
          nout = nout+1
          iday = t

c  output all recs
c  ----------------------------
         write(20,20) iday,i_lat,i_lon,(t-iday)*86400.d0,i_elev
20       format(i16,2f15.7,f16.4,f10.3)
c        end if
        end if
        j0 = j0+4
      end do

      irec = irec+1
      goto 10
80    continue


c  Output statistics to screen
c  ----------------------------
      write(*,*) 'last rec: no,utc,jd = ',i_rec_ndx,iutc,tjd
      write(*,*) 'output recs: ',nout

      write(*,*) 'rejected by elevation flag: ',nrej1
      write(*,*) 'rejected by area: ', nrej2
      write(*,*) 'rejected by off pointing: ', nrej3
      write(*,*) 'rejected by ocean sweep: ', nrej4
```



```
      write(*,*) 'rejected by sigma attitude: ', nrej5
      write(*,*) 'rejected by refl (0<R<1): ', nrej6
      write(*,*) 'rejected saturation corrections: ', nrej7
      write(*,*) 'rejected if saturation index = 126: ', nrej8
      write(*,*) 'deviation from gaussian fit (S < 60): ',nrej9
      write(*,*) 'rejected if gain > 30: ', nrej10
      write(*,*) 'rejected if more than 1 peak in wvf: ', nrej11
      write(*,*) 'rejected by geoid: ', nrej12
      write(*,*) 'rejected if elevation > 100: ', nrej13

      write(*,*) 'Rejected records: ',nrej3+nrej4+nrej5
     . +nrej6+nrej7+nrej8+nrej9+nrej10+nrej11+nrej12+nrej13
        write(*,*)

        write(*,*) '..............'
      end

ccccccccccccccccccccccccccccccccccccccccccccccccccccccccccccc
      integer*4 function i4(i0)
c     ----------------------------
c  reads integer*4 at adress i0
c
      integer*1 b(6760),b1(4)
      logical ldos
      equivalence(b1,k)
      common /rec/ b,ldos
      if (ldos) then
        b1(4) = b(i0+1)
        b1(3) = b(i0+2)
        b1(2) = b(i0+3)
        b1(1) = b(i0+4)
      else
        b1(1) = b(i0+1)
        b1(2) = b(i0+2)
        b1(3) = b(i0+3)
        b1(4) = b(i0+4)
      endif
      i4 = k
      return
      end
ccccccccccccccccccccccccccccccccccccccccccccccccccccccccccccc
      integer*2 function i2(i0)
c     ----------------------------
c  reads integer*2 at adress i0
c
      integer*1 b(6760),b1(2)
      logical ldos
      integer*2 k
      equivalence(b1,k)
      common /rec/ b,ldos
      if (ldos) then
        b1(2) = b(i0+1)
        b1(1) = b(i0+2)
      else
        b1(1) = b(i0+1)
        b1(2) = b(i0+2)
      endif
      i2 = k
      return
      end
```

```
      program LLF3glas
ccccccccccccccccccccccccccccccccccccccccccccccccccccccccccccccccccccc
c
c                          L L F 3 G L A S
c
c  program to detrend sea-ice scanner data by linear fit with
c  outlier rejection and optional collocation filtering of minimal values
c  will also make histogram of freeboard data
c
c  input:
c
c  ICESat file (dech,lat,lon,height)
c  outfile
c  dtmin, rejl, hcutoff, dtave, histsp, lcut, lcol
c  thalf, rmsn    (if lcol true)
c
c  where
c
c  dtmin: time spacing (dechr) for taking min value (0: just cut)
c  rejl:  limit for rejecting minimum values from linear fit
c  hcutoff: max scan height allowed (remove clouds)
c  dtave:  along-track averaging time for "fitlinc.ave"
c  histsp: histogram spacing
c  lcut: false: cut output in 0.02 dechr segments for plotting with pse
c        (assuming readscan thr,cross-trk output)
c        true: standard lat,lon output (lgeo=true in readscan)
c  lcol: use collocation after detrending, with corr.length thalf (hr) and
c        noise rmsn (c0 scaled from residuals). 2nd order Markov cov function.
c        warning: program makes one solution with all data - so keep number of
c        minimum points small (solves no of linear equations = no of min pts)!
c
c  outputfile contains freeboard heights and amplitude
c  "fitlinc.hst" contains histogram information
c  "fitlinc.ave" contains averaged free-boards (t,lat,lon,h_fb,n_points)
c
c  (c) Rene Forsberg/National Survey and Cadastre (KMS)
c  thule air base 19 may 2002
c  updated Alert 19 may 2004 (reading new format readscan data + collocation)
c  changed by Henriette Skourup (DNSC) July 2005 to read ICESat data files
c  including more than one orbit. Sort on time - for gaps larger than 1h
ccccccccccccccccccccccccccccccccccccccccccccccccccccccccccccccccccccc
c       n number of lines in each orbit
c       no number of orbits
c       nint number of minimum points
c       nh number of intervals in histogram
        implicit real*8(a-h,o-z)
        character*72 ifile,ofile
        character*1 ch
        logical lcut,lcol
        real*8 tmin(1000),hmin(1000),d(1000),td(1000)
        real*8 tminx(1000,100),hminx(1000,100)
        real*8 tminsum(1000),hminsum(1000)
        real*8 hsum50(1000),have50(1000)
        real*8 xhr(25000),rlat(25000)
        real*4 thr(25000),h(25000),gpst(25000)
        real*4 ino(25000)
        real*8 ha(25000)
        integer nlt,nobs,ks,ksend
        integer jint,nint,maxmin,jmin
        integer iamp(25000)
c       collocation dimension: icdim = (maxobs*(maxobs+1))/2+maxobs
        dimension c(501500)
        dimension nhist(100)
        nmax = 25000
        maxobs = 2500
        maxhist = 100
        maxmin = 3
c
        read(*,'(a)') ifile
        read(*,'(a)') ofile
        read(*,*) dtmin,rejl,hcutoff,dtave,histsp,lcut,lcol
        if (lcol) then
          read(*,*) thalf,rmsn
        endif
c
        write(*,*) 'FITLINC - linear detrending and collocation filtering'
```



```
c
        open(10,file=ifile,status='unknown')
        open(20,file=ofile,status='unknown')
        open(14,file='fitlinc.ave',status='unknown')
        open(15,file='fitlinc.hst',status='unknown')

c-----------------------------------------------------------------
c       Read in data
c       More than one orbit if timegap greater than 1h
c-----------------------------------------------------------------
        write(*,*) '- reading data from: ',ifile

        tdiff = 0
        ks = 1
        ksend = 0

        nlt=1
        i = 1
10      read(10,*,end=34) x1,x2,x3,x4,x5
        if (ks.eq.1) then
         ino(i) = x1
         rlat(i) = x2
         xhr(i) = x3
         gpst(i) = x4
         h(i) = x5
         thr(i) = gpst(i)/3600
         if (i.eq.1) GPSt(0) = GPSt(1)
         tdiff = GPSt(i) - GPSt(i-1)
        else
         ino(i) = x1
         rlat(i) = x2
         xhr(i) = x3
         gpst(i) = x4
         h(i) = x5
         thr(i) = gpst(i)/3600
         tdiff = GPSt(i) - GPSt(i-1)
        end if
        if (abs(tdiff).gt.3600) goto 35
        i = i+1
        nlt = nlt+1
        goto 10

34      continue
        ksend = ks

c       ks number of orbits
c       nobs number of observations in each orbit
35      nobs = i-1

c-----------------------------------------------------------------
c       Starting to do the calculation for each interval
c-----------------------------------------------------------------
36      if (dtmin.eq.0) goto 200
        nint = (thr(nobs)-thr(1))/dtmin + 0.5
        write(*,*) nint,thr(nobs),thr(1),dtmin,gpst(nobs),gpst(1)
        if (nint.gt.maxobs) stop 'too many minimum intervals'
c
c-----------------------------------------------------------------
c       now find minimum values
c       nint number of minimum values
c-----------------------------------------------------------------
        do j = 1, nint
        do k = 1, maxmin
                tminx(j,k) = -9999
                hminx(j,k) = 9999
        end do
        end do

        do i = 1,nobs
        jint = (thr(i)-thr(1))/dtmin+1
        if (h(i).lt.hminx(jint,1)) then
                hminx(jint,3) = hminx(jint,2)
                tminx(jint,3) = tminx(jint,2)
                hminx(jint,2) = hminx(jint,1)
                tminx(jint,2) = tminx(jint,1)
                hminx(jint,1) = h(i)
```

```
              tminx(jint,1) = thr(i)
        else if (h(i).lt.hminx(jint,2)) then
              hminx(jint,3) = hminx(jint,2)
              tminx(jint,3) = tminx(jint,2)
              hminx(jint,2) = h(i)
              tminx(jint,2) = thr(i)
        else if (h(i).lt.hminx(jint,3)) then
              hminx(jint,3) = h(i)
              tminx(jint,3) = thr(i)
        end if
        end do

        do j = 1, nint
        if (hminx(j,3).eq.9999.or.hminx(j,2).eq.9999.
     .     or.hminx(j,3).eq.9999) then
        do k = 1, maxmin
              tminx(j,k) = -9999
              hminx(j,k) = 9999
        end do
        end if
        end do
c
        do j = 1, nint
        tminsum = 0
        hminsum = 0
          do k = 1, maxmin
            tminsum(j) = tminsum(j) + tminx(j,k)
            hminsum(j) = hminsum(j) + hminx(j,k)
          end do
          tmin(j) = tminsum(j)/maxmin
          hmin(j) = hminsum(j)/maxmin
        end do

        write(*,31) ks,nobs,thr(1),thr(nobs)
31      format(///' orbit',i5,' read',i7,' points in interval:',2f9.4)
        write(*,*) 'Number of intervals: ',nint
        write(*,*) 'Mimimum values:'
        write(*,32) (hminx(j,1),j=1,nint)
        write(*,*) ' '
        write(*,32) (hminx(j,2),j=1,nint)
        write(*,*) ' '
        write(*,32) (hminx(j,3),j=1,nint)
        write(*,*) ' '
        write(*,32) (hmin(j),j=1,nint)
32      format(' ',10f7.1)

c-----------------------------------------------------------------
c  now detrend with linear funtion - reject outliers one by one
c  flag rejected points by time 9999
c  ---------------------------------------------------------------
        iloop = 1
        bias = 0
        alfa = 0

40      nsum = 0
        sumt = 0
        sumt2 = 0
        sumh = 0
        sumth = 0
        resmax = 0
        ressum2 = 0
        do 41 j = 1, nint
          if (tmin(j).eq.9999) goto 41
            tt = tmin(j)-thr(1)
            hh = hmin(j)
            res = abs(hh-(bias+alfa*tt))
          if (iloop.gt.1) then
            ressum2 = ressum2 + res**2
            if (res.gt.resmax) then
              resmax = res
              jmax = j
            endif
          endif
        nsum = nsum + 1
        sumt = sumt + tt
        sumt2 = sumt2 + tt**2
```



```
        sumh = sumh + hh
        sumth = sumth + tt*hh
41      continue
c
        if (resmax.ge.rejl) then
          tt = tmin(jmax)-thr(1)
          hh = hmin(jmax)
          nsum = nsum - 1
          sumt = sumt - tt
          sumt2 = sumt2 - tt**2
          sumh = sumh - hh
          sumth = sumth - tt*hh
          tmin(jmax) = 9999
          write(*,42) jmax,tt+thr(1),hh,bias+alfa*tt
42        format(' rej j,t,hh,hlin = ',i3,f9.4,3f9.2)
        elseif (iloop.gt.1) then
          goto 49
        endif
c
        r = nsum*sumt2 - sumt**2
        if (r.eq.0) r = 1.d-99
        bias = (sumt2*sumh - sumt*sumth)/r
        alfa = (-sumt*sumh + nsum*sumth)/r
c
        iloop = iloop+1
        goto 40
c
49      write(*,*) 'number of rejected min values: ',nint-nsum,
     .  ' out of ',nint
        write(*,491) sqrt(ressum2/nsum)
491     format(' r.m.s. residual of linear fit:',f9.2)
        nsel = nsum

c
c  collocation prediction
c  ----------------------
c  set up collocation equations
c  first move together arrays
c
80    if (lcol) then
        c0 = ressum2/nsum
        beta = 0.595*thalf
        cnn = rmsn**2
        write(*,101) thalf,rmsn,nsel
101     format(/' Collocation min value interpolation, thalf:',f6.3,
     .  ' hr, rmsn:',f6.2/' number of equations:',i4)

        j = 1
        do i = 1, nint
          if (tmin(i).lt.9998) then
            d(j) = hmin(i)
            td(j) = tmin(i)
            j = j+1
          endif
        enddo

        k = 0
        do 120 i = 1,nsel
        do 120 j = 1,i
        k = k+1
          r = abs(td(i)-td(j))

c  second order markov covariance function
          cov = c0*(1 + r/beta)*exp(-r/beta)
          if (i.eq.j) cov = cov + cnn
          c(k) = cov
120     continue
        irhs = k
        do i = 1,nsel
          c(irhs+i) = d(i) - (bias + alfa*(td(i)-thr(1)))
        end do
c
c  solve equations
c
        call chol(c,nsel,nsing)
        if (nsing.ne.0) write(*,*)
```

```
     .  '*** warning: singular equations - nsing = ',nsing
        write(*,*) '- Collocation equations solved -'
      endif
c
c  output data, cut in slices if lcut=true, geo output if lcut=false
c  -------------------------------------------------------------------
c
      hhmin = 9999
      hhmax = -9999
      hhsum = 0
      colsum2 = 0
      if (histsp.le.0) stop '*** histsp must be positive'
      nh = 3.0/histsp+1
      if (nh.gt.maxhist) nh = maxhist
      do i = 1,nh
        nhist(i) = 0
      enddo
c
      tave0 = thr(1)
      tsum = 0
      nsum = 0
      rlatsum = 0
      rlonsum = 0
      havesum = 0
c
      do i = 1, nobs
        hc = bias + alfa*(thr(i)-thr(1))
        cbias = 0
        if (lcut) then
          cbias = int((thr(i)-thr(1))*50)/50.d0
          throut = thr(i) - cbias
          xhrout = xhr(i) + cbias*0.1
        else
          throut = thr(i)
        endif
c
        hh = h(i)-hc
c
c  collocation prediction signal
        if (lcol) then
          sum = 0
          do k = 1, nsel
            r = abs(td(k)-throut)
            cov = c0*(1 + r/beta)*exp(-r/beta)
            sum = sum + cov*c(irhs+k)
          enddo
          hh = hh - sum
          hc = hc + sum
          colsum2 = colsum2 + sum**2
        endif
c
c  histogram
c
        if (hh.lt.hhmin) hhmin = hh
        if (hh.gt.hhmax) hhmax = hh
        hhsum = hhsum + hh
        ii = hh/histsp+2
        if (ii.ge.1.and.ii.le.nh) nhist(ii) = nhist(ii)+1
c
c  output
c
        if (lcut) then
          if (mod(i,500000).eq.1)
     .    write(*,50) i,throut,xhrout,hh
c     ,iamp(i),hc
          write(20,50) i,throut,xhrout,hh
c         ,iamp(i),hc
c50        format(i7,2f11.6,f9.2,i4,f7.2)
50        format(i7,2f11.6,f9.2)
          rlatsum = rlatsum + throut
          rlonsum = rlonsum + xhrout
        else
          if (mod(i,500000).eq.1)
     .    write(*,51) throut,rlat(i),xhr(i),hh,hc,h(i)
          write(20,51) throut*3600.d0,rlat(i),xhr(i),hh,hc,h(i)
51        format(f16.4,f11.5,f12.5,2f7.2,f8.2)
```



```
c         write(20,51) throut,rlat(i),xhr(i),hh,hc,h(i)
c51       format(f10.6,f11.5,f12.5,2f7.2,f8.2)

c         if (mod(i,500000).eq.1)
c     .    write(*,51) throut,rlat(i),xhr(i),hh,hc,h(i),ha(i)
c         write(20,51) throut,rlat(i),xhr(i),hh,hc,h(i),ha(i)
c       51       format(f10.6,f11.6,f12.6,2f7.2,f8.2,f7.2)
          rlatsum = rlatsum + rlat(i)
          rlonsum = rlonsum + xhr(i)
        endif
        nsum = nsum + 1
        tsum = tsum + throut
        havesum = havesum + hh
c
c  average output
c
        if ((thr(i)-tave0).gt.dtave) then
          if (nsum.gt.0) write(14,52)
     .    tsum/nsum,rlatsum/nsum,rlonsum/nsum,havesum/nsum,nsum
52        format(f9.6,f10.6,f11.6,f8.2,1x,i5)
          tave0 = thr(i)
          tsum = 0
          nsum = 0
          rlatsum = 0
          rlonsum = 0
          havesum = 0
        endif
c
      enddo
c
c  statistics and histogram
c  ------------------------
c
      n = nobs
      if (lcol) write(*,54) sqrt(colsum2/n)
54    format(' r.m.s. collocation signal: ',f9.2)
      write(*,55) hhmin,hhmax,hhsum/n
55    format(' min, max and average output values: ',3f9.2)
c
      write(*,*)
      write(*,*) 'Histogram of freeboards (percent):'
      write(15,58) ks
58    format('Histogram orbit',i5)
      do i = 1,nh
        ch = '*'
        pct = nhist(i)*100.d0/n
        ipct = pct/2.5 + 0.5
        write(*,56) histsp*(i-2),histsp*(i-1),nhist(i),pct,(ch,j=1,ipct)
56      format(f6.2,' -',f5.2,i7,f9.3,' !',41a)
        write(15,57) histsp*(i-2),histsp*(i-1),nhist(i),pct
57      format(f6.2,f6.2,i6,f9.3)
      enddo

c-------------------------------------------------------------------
        ino(1) = ino(nobs+1)
        rlat(1) = rlat(nobs+1)
        xhr(1) = xhr(nobs+1)
        gpst(1) = gpst(nobs+1)
        h(1) = h(nobs+1)
        thr(1) = thr(nobs+1)
        if (ks.eq.ksend) goto 200
        ks = ks + 1
        i = 2
        goto 10

200     continue
        write(*,*) ' '
        write(*,*) 'End of File'
        write(*,*) 'Total number of lines in data file: ',nlt-1
        write(*,*) 'Number of orbits in file: ',ks-1
        close(10)
        close(20)
        close(14)
        close(15)
        end
c
```

```
c
        subroutine chol(c,n,nsing)
        implicit double precision(a-h,o-z)
ccccccccccccccccccccccccccccccccccccccccccccccccccccccccccccccccc
c
c                       c h o l
c
c  subroutine solves positive definite symmetric linear equations
c  using cholesky decomposition. coefficients stored columnwise
c  in c, followed by righthand side. n is number of unknowns.
c  solution is returned as last column in c.
c  'nsing' is number of singularities. it should be zero for a
c  succesful solution.
c
c  rf, nov 85
c
ccccccccccccccccccccccccccccccccccccccccccccccccccccccccccccccccc
      dimension c(501500)
      nsing = 0

      do 50 nr = 1,n+1
        i=nr*(nr-1)/2
        ir=i
        do 40 nc = 1,nr
          if (nc.gt.n) goto 50
          sum=0
          ic=nc*(nc-1)/2
          i=i+1
          nc1=nc-1
          do 30 np = 1,nc1
30        sum = sum - c(ir+np)*c(ic+np)
          ci = c(i)+sum
          if (nr.eq.nc) goto 31
          cc = c(ic+nc)
          if (cc.eq.0) then
            write(*,*) '*** Cholesky reduction zero-division'
            cc = 1.0e9
          endif
          c(i) = ci/cc
          goto 40
31        if (nr.gt.n) goto 40
          if (ci.gt.0) goto 32
            nsing = nsing+1
            c(i) = 1.0e9
            goto 40
32        c(i) = sqrt(ci)
40      continue
50    continue
c
c  back substitution
c
      do 80 nc = n,1,-1
        ir=i
        ic=nc*(nc+1)/2
        cc = c(ic)
        if (cc.eq.0) then
          write(*,*) '*** Cholesky subsitution zero-division'
          cc = 1.0e9
        endif
        c(i) = c(i)/cc
        do 70 np = nc-1,1,-1
          ir=ir-1
          ic=ic-1
          c(ir) = c(ir) - c(i)*c(ic)
70      continue
        i = i-1
80    continue
      return
      end
```

G Published papers

The references of the enclosed papers are:

Skourup, H. and R. Forsberg: Sea ice freeboards from ICESat - A comparison to airborne lidar measurements. Arctic Sea Ice Thickness: Past, Present and Future, edited by P. Wadhams and G. Amanatidis. Climate Change and Natural Hazards Series, Brussels, 2006

Skourup, H., R. Forsberg and A. Braun: Gravity Anomalies and Sea Ice Thickness in the Arctic Ocean from ICESat. Proceedings, Gravity Field of the Earth - 1st meeting of the International Gravity Field Service. Harita Dergisi, vol. 73, issue 18, pp. 242 - 247, Ankara 2007

Skourup, H. and R. Forsberg: Geoid, Sea Level and Vertical Datum of the Arctic - Improved by ICESat and GRACE. GEOMATICA Vol. 62, No. 2, pp. 287 - 298, 2008

Sea ice freeboard from ICESat – an airborne lidar validation

H. Skourup, R. Forsberg
Geodynamics Dept, Danish National Space Center
Juliane Maries Vej 30, DK–2100 Copenhagen Oe, Denmark
hsk@spacecenter.dk

Abstract
In connection with the GreenICE ice camp in the Arctic Ocean north of Alert, May 2004, airborne sea-ice laser scanner data was measured on transits to the drifting icecamp, as well as in dedicated laser scanner flights. Two lines were flown along ICESat ground tracks, in order to do a near-coincident underflight of the ICESat satellite. In this paper we report on the intercomparison of the freeboards estimated by high-resolution airborne swath laser data and the laser altimetry from ICESat. Our results show that the satellite laser measurements have good agreement with the airborne laser scanner, but due to the larger footprint and lower along-track laser shot sampling, ridges and leads are significantly underestimated, when using a lowest-level filtering method to estimate the mean sea level. In the very rough and thick sea-ice region north of Greenland, this bias is found to be around 35 cm for our specific filtering algorithm, thus providing a possible systematic error in ICESat derived freeboards. We conclude the paper by deriving Arctic Ocean-wide freeboard map for two ICESat periods in 2003 (laser 1 and laser 2A). The derived ice freeboard (and implied thickness) are plotted and compared to QuikSCAT backscatter maps, showing a good qualitative agreement.

1. Introduction

The utilization of altimeter satellites to measure ice thickness is important for repeated large-scale change measurements of the Arctic Ocean sea-ice. Such large-scale monitoring is practically impossibly to other by other techniques alone, such as airborne, by ship, or submarines. NASA's ice, cloud, and elevation laser altimeter satellite (ICESat) launched in January 2003, gives for the first time the opportunity to produce detailed maps of the sea ice freeboards in most of the Arctic Ocean, covering up to 86°N, expanding the sea-ice thickness coverage from ERS radar altimetry, available south of 81°N (Laxon et al., 2003). First published investigations on the use of ICESat for sea-ice thickness measurements include Kwok et al. (2004), and Forsberg and Skourup (2005). In this paper we report on the first direct underflight of ICESat with a high-resolution airborne lidar system, giving more insight into the return signals of ICESat.

The airborne lidar data were collected as part of the Danish National Space Center GreenIce field campaign 2004, using an Air Greenland Twin-Otter, equipped with precise GPS, INS and a swath scanning laser system, see Hvidegaard et al. (this volume) for a more detailed description of the DNSC lidar system. The 2004 operations and processing are described in detail in a DNSC technical report (Dalå et al., 2005). As part of the GreenIce/SITHOS flight operations, a detailed survey of the sea-ice north of

Greenland was carried out, in part to repeat earlier lidar flights in the region (Hvidegaard and Forsberg et al., 2002).

The lidar underflight of ICESat was flown in the Arctic Ocean north of Greenland on May 25, 2004, following the demobilization of the GreenIce ice camp, and after a long period of waiting for good weather at the Canadian Forces station Alert. Two near-coincident partially cloud-free tracks were flown on May 25, 2004, see Figure 1 for the track location.

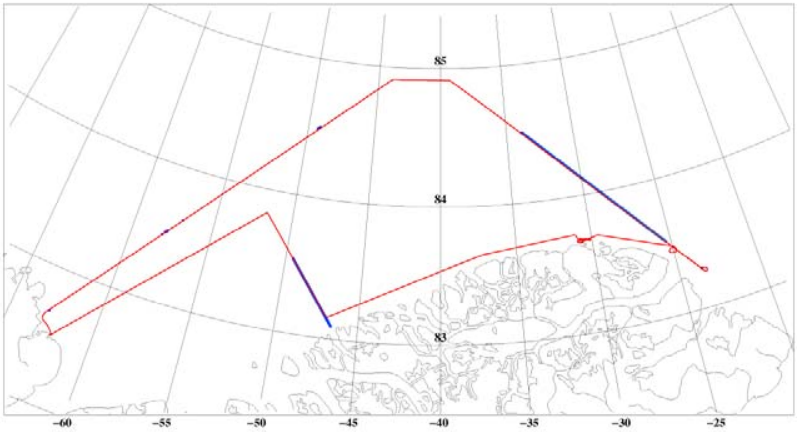

Figure 1. The red line is the Twin-Otter flight track of May 25, lined up along several ICESat tracks. The blue lines are the cloud-free near-coincident ICESat subtracks.

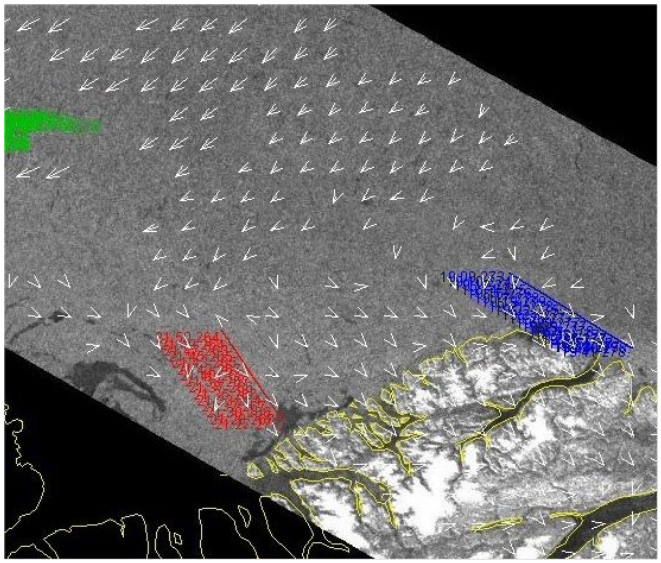

Figure 2. ENVISAT ASAR imagery for May 25, with estimated ice drift vectors from repeated ASAR scenes. The maximum velocity is roughly 3 km/day to be found in the northwestern area of the image. The random nature of the velocities off the coast of northern Greenland confirms the essentially no-drift condition in the survey area. Figure courtesy Leif Toudal, Danish Technical University.

Both subtracks span approximately 50 km or approximately 300 ICESat observations. Unfortunately a timing error for the aircraft scheduling gave an 8 hr delay in the underflight compared to the ICESat passage. However, by luck, the ice both along the western and eastern flight tracks showed essentially no movement in the period due to calm wind conditions, as verified by drift vectors estimated from ENVISAT ASAR interferometry, cf. Figure 2.

2. Freeboard estimation from ICESat and airborne lidar

The ICESat laser instrument (GLAS) operates at two wavelengths, an infrared channel (1064 nm), primarily used for surface altimetry, and a green (532 nm) channel primarily used to measure the vertical distribution of clouds and aerosols (Zwally et al., 2002). The infrared channel wavelength is almost identical to the DNSC airborne laser scanner system working at a wavelength of 904 nm. The pulse repetition frequency for ICESat is 40 Hz corresponding to an along-track separation of the centers of the footprints by approximately 172 m, and the footprint size is approximately 70 m wide. The accuracy of the ICESat ellipsoidal heights of the sea-ice surface is approximately 15 cm. We have here used ICESat data from release 18 (Laser 1, March 2003) and release 21 (laser 2A, October 2003).

The ICESat laser data are to be compared to the DNSC high-resolution airborne laser scanner data. In this system swath scanning is used, with a basic laser footprint size of 1 x 1 m at the flight height of 300 m. The lidar system measures data in an across-track swath of width roughly equal to the flight height, with an inherent relative precision of a few cm. Absolute errors in determing the sea-ice ellipsoidal errors are estimated to be 20-30 cm due to errors in the long-range kinematic aircraft positioning. For more information on the airborne instrumentation and the system setup, see the paper by Hvidegård et al. (this volume).

For both ICESat and the airborne freeboard estimation, a geoid model is used as a first approximation of the sea surface heights (SSH) above the ellipsoid. However, due to tidal errors, ocean mean dynamic topography, and measurement errors, it is necessary to use a lowest-level filtering scheme, where the lowest geoid-reduced measured laser ranges are fitted to a smooth curve, supposedly reflecting the instantaneous SSH. For airborne laser data this method was originally described in Hvidegård and Forsberg (2002), using a polynomial fit scheme to define the smooth SSH surface. In the ICESat investigations here, this scheme has been updated to use a smooth least-squares collocation (optimal estimation) function, yielding nearly equivalent results to the polynomial scheme, but allowing a more flexible fitting to the assumed “lowest level” points (assumed to be open water or leads with thin ice). The typical distance used between such points is 5-15 km, and will in practice be chosen based on ice properties and geoid model errors. We here use an updated arctic geoid model, derived by spherical FFT methods from the Arctic Gravity Project terrestrial data (Forsberg and Kenyon, 2004) and GRACE satellite data, for more details see (Forsberg and Skourup, 2005). An example of the lidar swath free-board data, and coincident nadir imagery, is shown in Figure 3.

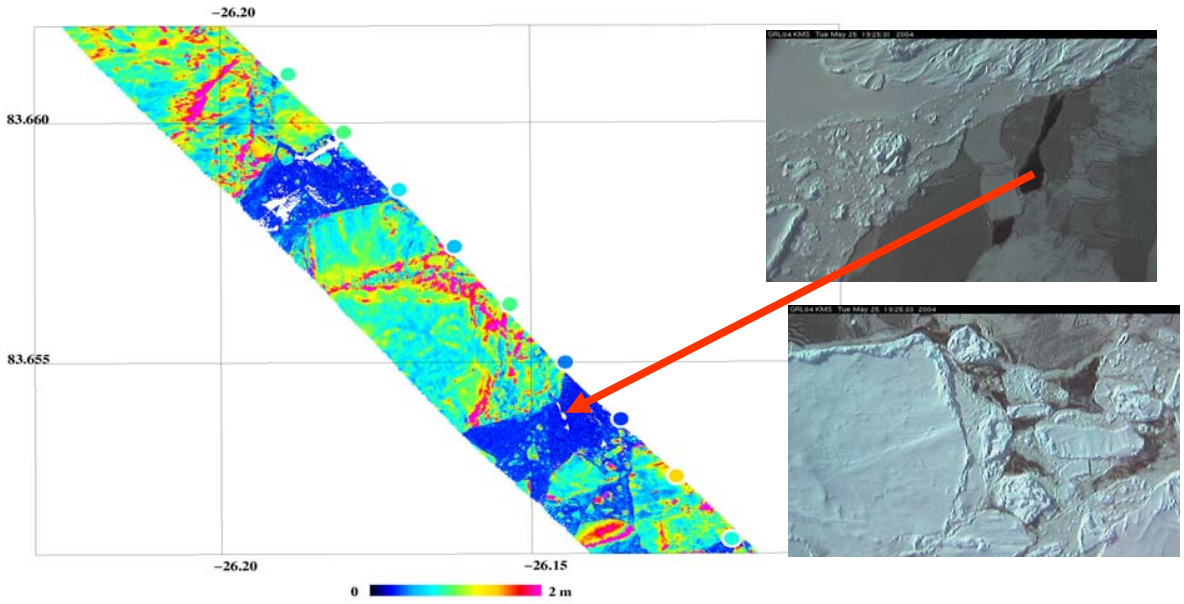

Figure 3. Example of lidar swath freeboard data (width approx. 250 m) after lowest-level filtering. ICESat measurements shown with circles, same color coding. A good qualitative agreement is seen.

In this study, the raw laser scanner data has been converted to sea ice freeboards by applying the above described technique. The airborne data volume has been decreased by averaging across-track and thinning along-track to a resolution of approximately 5 by 5 m. For the ICESat-derived freeboards we have used the GLA13 data product, specially designed for sea ice applications. The May 25, 2004, ICESat data were from laser 2C, release 17. The lowest level algorithm was applied to ICESat taking the average value of the three lowest levels for each interval of 10 km. For the airborne lidar data, with the much higher spatial resolution, the lowest level of the vertical component is used within an average interval of 10 km along the swath. We also made tests with 5 km resolution "lowest-level" filtering, yielding changes in the lowest level surface of typically 5 cm. Therefore algorithm-dependent biases in the freeboard results could be at a similar level.

3. Comparison of ICESat and airborne lidar

Figure 4 shows the vertical component of the scanner data plotted against the ICESat freeboard, as well as the reflectivity of the surface, as measured by ICESat. An offset on 36 cm for the eastern most track and 37 cm for the western most track were found. The offset is believed to originate from an overestimation of the lowest-level fit points, as the sea-ice heights are averaged over the relative large ICESat footprint ~70 m and the lower along-track resolution. We also show the ICESat-measured reflectivity of the ice surface, which can be an indicator of presence of leads; work done by Kwok et al. (2004) shows that the reflectance of open water, and newly formed lead ice has a very low value, which rapidly increases with thickness.

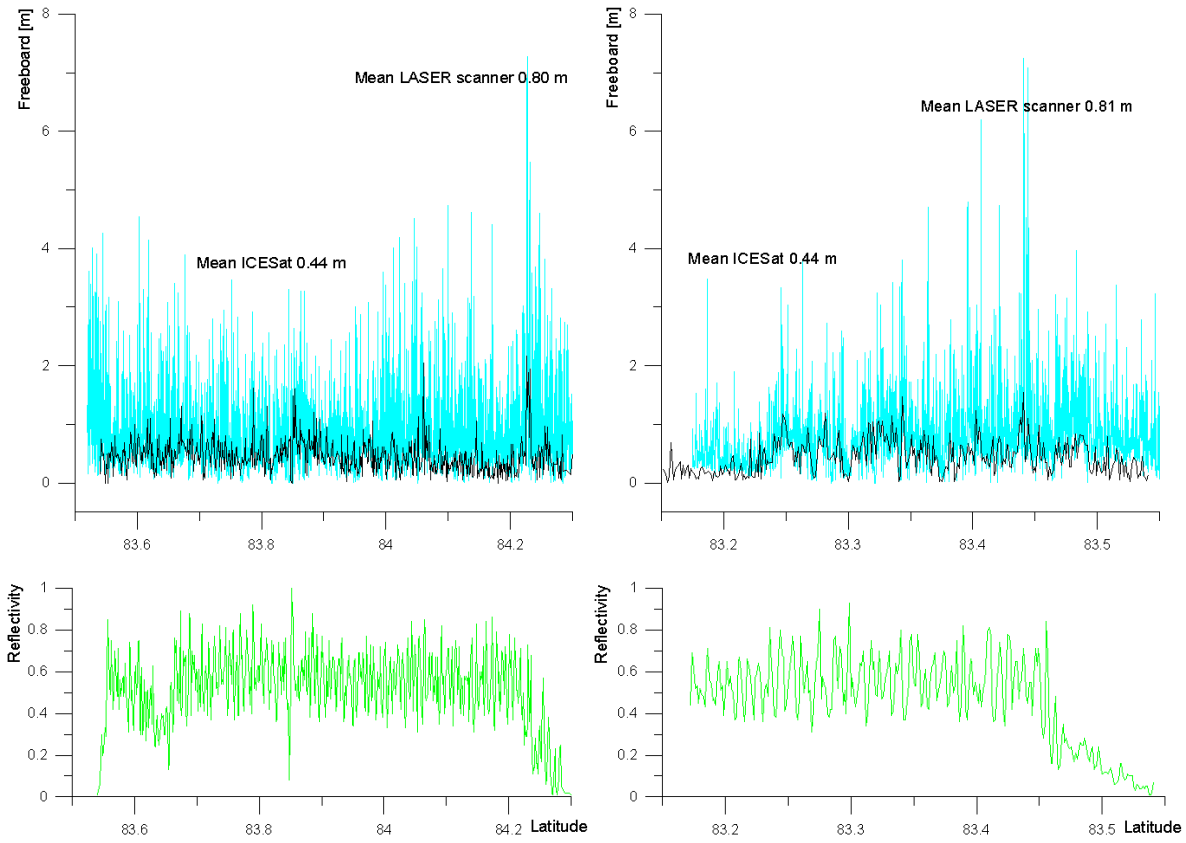

Figure 4. Sea freeboard heights from ICESat (black), and the vertical component from airborne lidar (blue) for the eastern flight (to the left) and the western subtrack (to the right). Lower plot in green: reflectivity of ICESat. It is seen that the sea-ice region north of Greenland ridges up to 6 m high.

The effect of smoothing across the ICESat footprint can also be detected in the freeboard distributions, see Figure 5, where the probability density functions of freeboard heights for ICESat and scanner data are plotted. In these plots we have added a bias to the ICESat freeboard to be able to compare the features. It is seen that the thinnest ice classes and ridges are almost absent in the ICESat freeboard distributions, but present in the laser scanner freeboard distributions.

To further compare the airborne scanner and ICESat derived freeboards, the airborne scanner data has been modeled to match the ICESat footprint. The modeled footprint is assumed to be circular, and has been weighted by the far field beam pattern, taken to be near Gaussian in shape, with 1/e-width set to 35 m to match the footprint size. The result of this comparison is shown in Figure 6 for the western track. The correlation between the two data sets has a correlation coefficient r = 0.65, which is fairly good. The ICESat freeboard seems to decrease in the northern-most end of the data set, which can possibly be explained by the presence of low fog and clouds in this area, causing decay in the strength of the laser signal from the satellite.

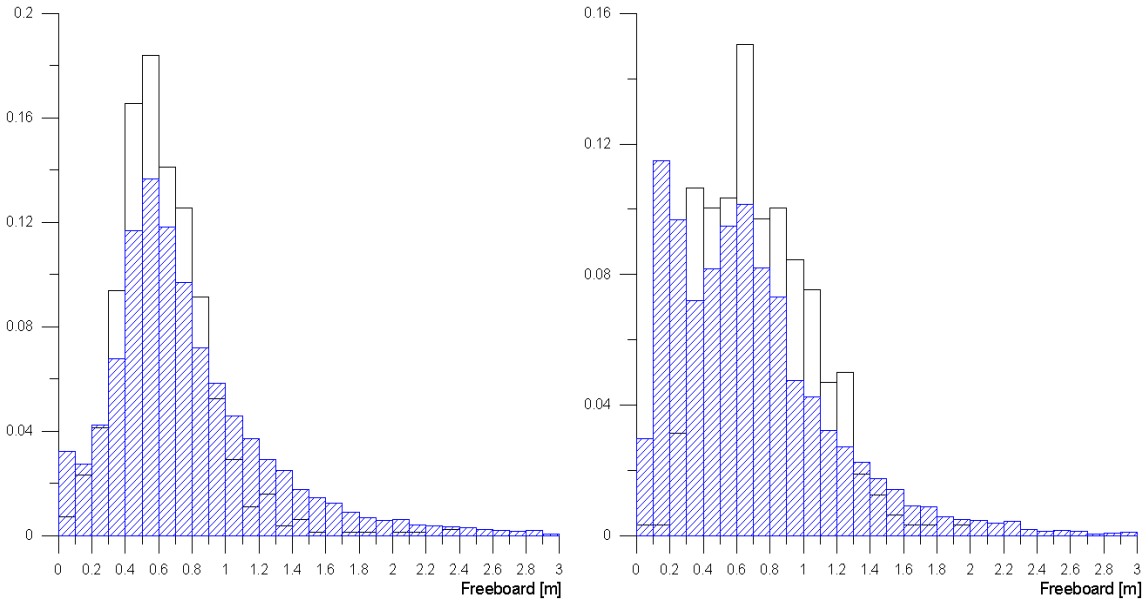

Figure 5. Probability functions for sea-ice freeboard heights from ICESat (open bars) and airborne lidar (hatched bars), for the western subtrack (left) and the eastern subtrack (right).

The lowest-level technique used to estimate the sea ice freeboards is highly dependent on the presence of leads with open water or thin ice. North of Greenland the sea ice is primarily thick perennial ice, with heavy ridges and rubble fields with very few or no open leads (Figure 7). It is therefore likely the cause of the bias is that the "lowest points" as seen by ICESat are more thick ice than the narrow leads seen by the airborne lidar. This is also sustained by the reflectivity profiles of Figure 4, where no major leads, expressed by the lower reflectivity, are seen.

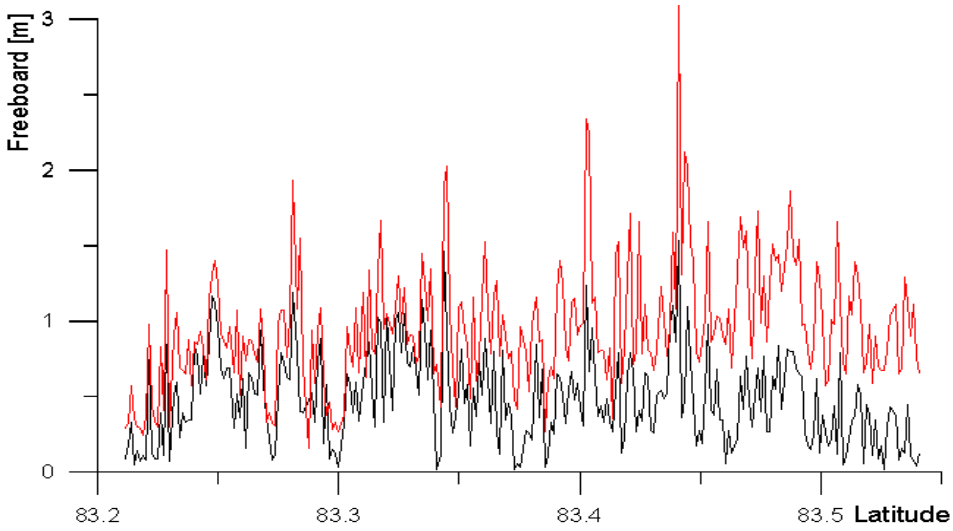

Figure 6. Comparison of ICESat freeboard heights (black) and averaged airborne lidar data (red) for the western subtrack. Due to lack of leads the ICESat values are biased.

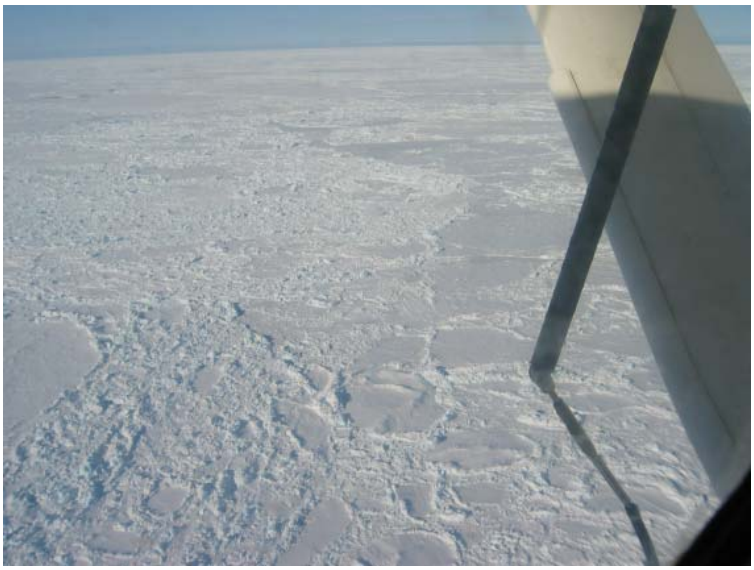

Figure 7. Typical sea-ice north of Greenland (eastern subtrack), May 25, 2004.

4. Arctic Ocean-wide sea ice freeboard maps

The same procedure as described above to estimate the sea ice freeboard has been applied to two periods of ICESat data (the only data sets currently available at the National Snow and Ice Data Center) to estimate Arctic Ocean-wide sea ice freeboard maps. The data covers periods February 20 – March 29, 2003 (laser 1, release 18) and September 25 – November 18, 2003 (laser 2a, release 21).

The algorithms have been applied to each ICESat track in a given period, taking the three lowest levels averaged for each interval of 20km. To remove effects from clouds, heights above/below 1.5 m has been rejected after removal of the geoid. In addition data have been rejected if the standard deviation of Gaussian fit to the waveform is larger then 60 mV, and the reflectivity uncorrected for atmospheric effects has to be within limitation 0 and 1. As the data covers large areas and relatively long periods, the inverted barometer (IB) correction is applied each ICESat shot by use of NCEP sea level pressure fields, which has been converted to IB by use of a conversion equation (Kwok, pers.comm.)

$$IB\ (mm) = -13.1 * (P\ (mbar) - 1013.3)$$

The resulting Arctic Ocean sea-ice freeboard maps are plotted in Figure 8, together with backscatter maps obtained by the SeaWinds scatterometer - QuikSCAT – for comparison. The data from QuikSCAT has been used to define a 40% ice concentration mask, so that only ice-covered regions are analysed. The backscatter data from QuikSCAT backscatter shows qualitatively the same features as in the ICESat estimated freeboards, with thick perennial sea ice north of Greenland (with freeboards up to 1 m, corresponding to a sea-ice thickness of 6 m), and less thick sea-ice in the Arctic Ocean north of Siberia.

In addition the ICESat freeboard maps show seasonal variations with winter conditions present in the laser 1 data set, represented by a larger extent of sea ice, e.g. off the coast of east Greenland. Laser 2a represents fall conditions, just after the minimum sea-ice extent in September. The freeboard map shows here much less ice, both in extent but also in freeboard, especially in the Siberian Arctic (Chukchi Sea).

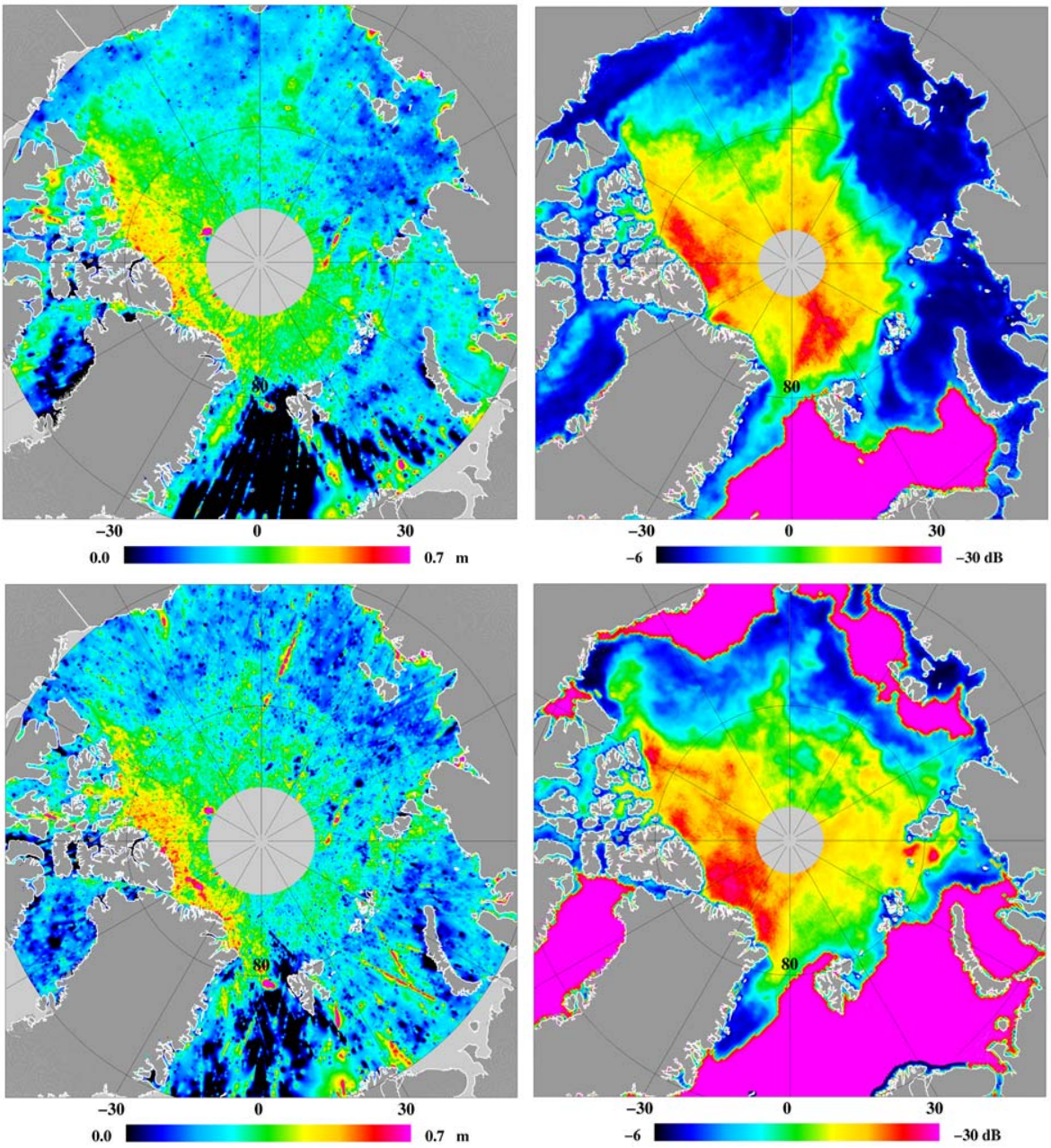

Figure 8. Left column: ICESat derived sea ice freeboards in the Arctic Ocean, upper image laser 1 February 20 – March 29, 2003 and lower image laser 2A September 25 – November 18, 2003. Right column: QuikSCAT backscatter maps for the Arctic Ocean with ocean mask (pink), upper image February 21, 2003 and lower image October 15, 2003.

5. Conclusions

The airborne underflight of ICESat shows that lowest level filtering techniques for ICESat may produce a bias in the estimated sea-ice freeboard heights. We found a bias of approximately 35 cm in the region north of Greenland for 10 km-resolution lowest level filtering. We believe the bias is due to the lower spatial sampling of ICESat, with fewer points to hit the open leads, and also due to averaging the freeboard across the footprint. The smoothing features in ICESat was also seen in the comparison of the probability density functions, where thin ice, and ridges are absent in the ICESat data, but present in the laser scanner data. By modeling the high-resolution scanner data to match the ICESat footprint return, a fairly good correlation is found, and the short-wavelength ICESat features are mapped well in the modeled data.

Only very few cases of low reflectivity are found in the two ICESat subtracks, indicating that ICESat only picks up very few open or thin-ice leads to represent the lowest levels. This information can be implemented in future sea ice thickness products based on ICESat data, where a combination of lowest level and reflectivity probably would give better results. It is also to be expected that the bias problem is less in other regions of the Arctic Ocean, where ice is thinner and more leads are found.

We also used the lowest-level filtering method to analyse the ICESat data for 2003, and presented two Arctic Ocean-wide freeboard maps. These were consistent with backscatter features as seen by QuikSCAT. Thick ice approximately 6m is found north of Greenland with thinner ice classes in the Chukchi Sea. The maps also show seasonal variations. For future more accurate recovery of sea-ice freeboards from ICESat we believe that combination methods using both lowest level filtering and reflectivity could be useful. More coincident airborne data in other parts of the Arctic would also be useful for a more detailed characterization of possible biases as a function of sea-ice roughness and dynamics.

Acknowledgements

We thank B. Schutz, Univ. of Texas, for providing the ICESat orbit information. The ICESat data used for the airborne comparison were obtained from NASA-GSFC (D. Yi and J. Zwally). The 2003 ICESat data were obtained from NSIDC. L. Toudal, DTU, provided the Envisat SAR interferometry ice drift vectors for the ICESat tracks. NCEP Reanalysis data were provided by the NOAA-CIRES Climate Diagnostics Center, Boulder, Colorado, USA, from their Web site at http://www.cdc.noaa.gov/ The QuikSCAT data were obtained from CERSAT, at IFREMER (France). Nynne S. Dalå and Sine M. Hvidegård, DNSC, have contributed to the processing of the lidar data.

References:

Dalå, N.S., R. Forsberg, K. Keller, H. Skourup, L. Stenseng, and S. M. Hvidegaard: *Airborne lidar measurements of sea ice north of Greenland and Ellesmere Island 2004. GreenICE/SITHOS/CryoGreen/A76 projects,Final Report.* Technical Report, Danish National Space Center, 2005.

Forsberg, R., K. Keller, S. M. Jacobsen: Airborne Lidar measurements for Cryosat validation. Proc. IEEE IGARSS-2002, Toronto, vol. III pp. 1756-1758, 2002.

Forsberg, R. and S. Kenyon: *Gravity And Geoid in The Arctic Region – The Northern Polar Gap Now Filled*. 6 pp., Proc. GOCE Workshop, ESA-ESRIN, March 2004.

Forsberg, R., and, H. Skourup: *Arctic Ocean Gravity, Geoid and Sea-ice Freeboard Heights from ICESat and GRACE*. Geophysical Research Letters, vol. 32, L21502, 2005.

Hvidegaard, S.M., and R. Forsberg: *Sea-ice thickness from airborne laser altimetry over the Arctic Ocean north of Greenland*, Geophysical Research Letters, vol. 29, no. 20, pp.1952-1955, 2002.

Kwok, R., H.J. Zwally, and D. Yi: *ICESat observations of Arctic sea ice: A first look.* Geophysical Research Letters, vol. 31, L16401, 2004.

Zwally, H.J., B. Schutz, W. .Abdalati, J. Abshire, C. Bentley, A. Brenner, J. Bufton, J. Dezio, D. Hancock, D. Harding, T. Herring, B. Minster, K. Quinn, S. Palm, J. Spinhirne, and R. Thomas: *ICESat's laser measurements of polar ice, atmosphere, ocean, and land.* Journal of Geodynamics 34, pp. 405-445, 2002.

Laxon , S., N. Peacock, and D. Smith, High interannual variability of sea ice thickness in the Arctic region, Nature 425, 947-950, 2003.

Gravity Anomalies and Sea Ice Thickness in the Arctic Ocean from ICESat

H. Skourup, R. Forsberg
Department of Geodynamics,
Danish National Space Center, Juliane Maries Vej 30, DK-2100 Copenhagen Oe, Denmark

A. Braun
Department of Geomatics Engineering,
The University of Calgary, 2500 University Drive N.W., Calgary, Alberta, Canada, T2N 1N4

Abstract

The ICESat laser altimetry mission has since January 2003 provided satellite altimetry over the ice-covered Arctic Ocean up to 86°N. The laser altimetry surface elevation data is the sum of geoid, sea ice freeboard and ocean mean dynamic topography, but by a combination of lowest level filtering and GRACE-based geoid models the signals may be separated, and sea ice thickness and gravity field information be recovered. In the paper we derive an improved gravity anomaly field for the Arctic Ocean using FFT Wiener filtering methods. The composite ICESat gravity grid shows all the major tectonic features of the Arctic Ocean at high resolution. The results are compared to the recently revised Arctic Gravity Project anomaly grid and airborne gravity. The results show that the laser altimetry data may provide excellent gravity results comparable to open ocean altimetry even over the most heavy ice conditions.

1 Introduction

Satellite altimetry missions have in the past decade improved the knowledge of the gravity field in vast, remote regions such as the oceans. Over the oceans altimeters map the mean sea surface (MSS), after correction for tides. The MSS represent the marine geoid if the mean dynamic topography (MDT) is neglected. The marine geoid can be inverted to gravity anomalies, e.g. by use of Fast Fourier Transforms.

If we consider even more remote and hostile regions like the Arctic Ocean, access to satellite data are limited in coverage due to the inclination of the satellite orbits, leaving a gap around the pole. Since the launch in January 2003 NASA's laser altimeter onboard the Ice, Cloud and land Elevation Satellite (ICESat) have for the first time collected data up to 86°N. This is an improvement compared to the ESA missions ERS-1/2 and ENVISAT, which covers up to 81.5°N. Another important factor in the Arctic Ocean is the presence of sea ice. To estimate the Arctic MSS it is necessary to remove the sea ice freeboard height (the part of the sea ice above sea level) from the altimetry measurements. The MSS can be expressed as

$$MSS = h - F = N + MDT \quad (1)$$

where h is the ellipsoidal height of the altimetry measurements corrected for tides, F the freeboards, N the geoid, and MDT the mean dynamic topography.

The sea ice freeboards can be obtained directly from altimetry data. Methods to determine sea ice freeboards from radar altimetry were originally developed for ERS by Laxon et al (2003). Here we apply a lowest level filtering algorithm developed for airborne lidar flights, Hvidegaard and Forsberg (2002), to estimate sea ice freeboards from ICESat data.

The studies in this paper are part of an ongoing ESA study ArcGICE, which have as a main objective to make an improved Arctic Ocean MSS, to be used as reference for future CryoSat measurements of the sea ice freeboard. In order to improve the MSS the aim is to improve the existing geoid and MDT models by combining surface, airborne and satellite measurements. Here we investigate ICESat altimetry observations to derive gravity anomalies and sea ice freeboards in the Arctic Ocean.

A preliminary gravity field based on two ICESat epochs from 2003 was published by Forsberg and Skourup (2005). In this paper we investigate how the gravity field is influenced by including seven epochs of ICESat data covering the period 2003-2005, which

Table 1. Used ICESat epochs 2003-2005

LASER	Period	Year
1	February 20 – March 29	2003
2A	September 25 – November 18	2003
2B	February 17 – March 21	2004
2C	May 18 – June 21	2004
3A	October 3 – November 8	2004
3B	February 17 – March 24	2005
3C	May 20 – June 23	2005

we have gained access to within the ArcGICE project. The ICESat epochs to be included here are listed in Table 1. We also estimate an Arctic Ocean wide sea ice freeboard map for each of the ICESat periods, and compare the gravity anomalies derived from the MSS not corrected for sea ice freeboard heights (the raw altimeter measurements) to a field corrected for sea ice. This is done to investigate whether or not the resulting field is improved by removal of the sea ice from the altimeter data. In order to validate the three gravity fields, they are compared to the Arctic Gravity Project and airborne gravity campaigns carried out during the 1990's.

The results of the ICESat derived gravity anomalies can be used to improve existing gravity models in regions with sparse or poor data. The improved gravity field or geoid can then also be used to estimate better sea ice freeboards.

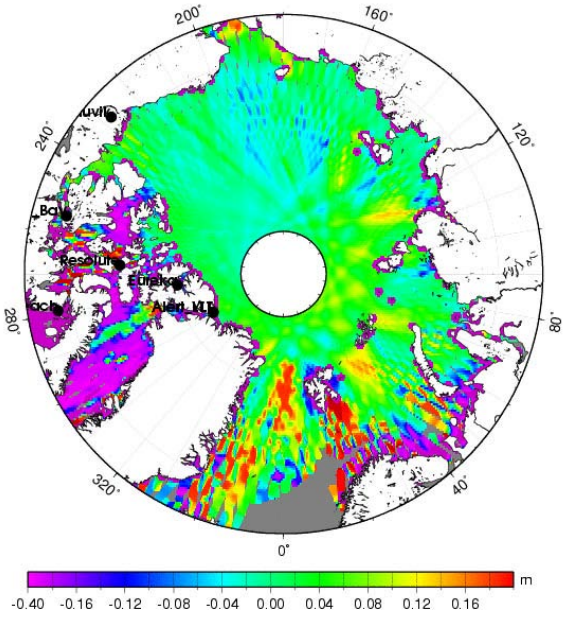

Fig. 1 Differences between GOT99.2 and the Padman tide models applied to ICESat epoch February-March, 2003.

2 Method

In order to compute the gravity anomalies from ICESat observation data have to be corrected for tidal and atmospheric effects, and the sea ice freeboards need to be removed.

2.1 Tide Corrections and Inverse Barometer Effects

ICESat altimeter data have been corrected for tides using the global tide model GOT99.2 (GOT = Goddard/Grenoble Ocean Tide) [Ray, 1999]. This tide model is primarily based on TOPEX/Poseidon altimetry data available south of 66°N. We apply here the Arctic Ocean regional tide model by Padman and Erofeeva (2004), which uses a combination of TOPEX/Poseidon and ERS altimetry, and assimilates coastal and benthic tide gauges. Accordingly, the Padman model is expected to perform better in the Arctic regions.

The tide corrections from the two models have been computed and applied to all the ICESat epochs. The differences between the two tide models are shown in Figure 1 for ICESat epoch February-March 2003. Differences between the two fields are primarily seen in the coastal regions; the Canadian Arctic Archipelago, Nares Strait, the Baffin Bay and Labrador Sea. The regional as well as the seasonal variability obtained are on the order of a few centimeters.

The inverse barometer (IB) effect removes some of the "trackiness" present in the altimeter data. The correction originating from inverse barometer (IB) effect can be calculated from the sea level pressure (SLP):

$$IB = \alpha\,(SLP - 1013.3) \qquad (2)$$

where the constant 1013.3 mbar represent the global mean sea level pressure calculated over the oceans, and the proportionality constant α is taken to be -11.2 mm/mbar based on work done by repeated ICESat tracks in the Arctic by Kwok et al. (2006). The sea level pressure (SLP) fields used here to obtain the IB correction for each ICESat sample is linearly interpolated from 6-hourly NCEP/NCAR reanalysis products provided by the NOAA-ESRL PSD Climate Diagnostics Center Branch, Boulder Colorado. Spatial and temporal differences due to the IB effects are on the order of a few decimeters.

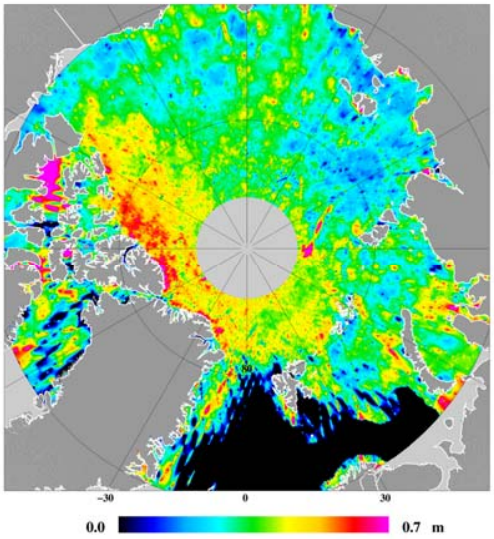

Fig. 2 Map of sea ice freeboard height in the Arctic Ocean derived from ICESat data epoch February-March, 2003.

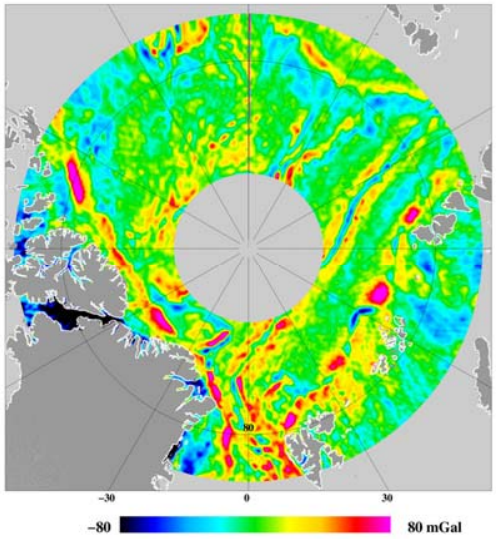

Fig. 3 Gravity anomalies in the Arctic Ocean with all seven epochs merged into one field. Corrected for sea ice.

2.2 ICESat Sea Ice Freeboard Heights

To estimate the sea ice freeboards from ICESat we are using a modified method developed for airborne lidar campaigns, Hvidegaard and Forsberg (2002). From equation (1) the freeboard (F), including snow cover, is given by

$$F = h - N - MDT - e \qquad (3)$$

where h is the ellipsoidal height of the altimeter measurements after removal of tides, N is the geoid, MDT the mean dynamic topography, and e measurement errors. The first step is to remove the geoid from the altimeter data. We are here using the geoid representation from the Arctic Gravity Project (ArcGP) see Kenyon and Forsberg (2001).

We apply a lowest-level filtering scheme to the height (h-N) by taking the average of the three lowest values of an along-track interval of 20 km. The lowest values are believed to represent open leads or thin ice in between the floes. A smooth curve determined by least-squares collocation is computed between the lowest levels, which we assume represent the sea surface height. Subsequently the freeboard heights are estimated by subtracting the smooth curve from the data.

To remove false freeboard heights over open ocean, originating from the lowest-level algorithm favoring the trough of the waves, an open water mask

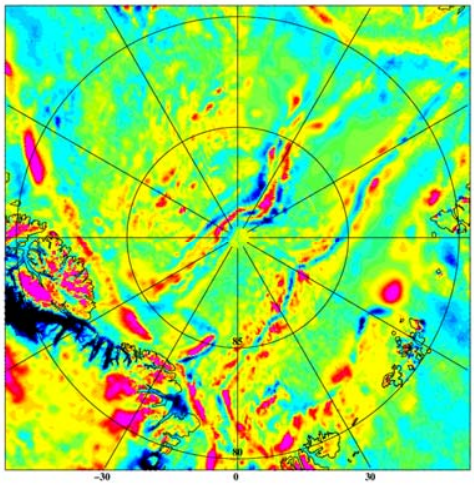

Fig. 4 The Arctic Gravity Project (ArcGP) gravity anomalies, version February 2006. Same colour scaling as in Figure 3.

is applied. The mask is obtained from SeaWinds scatterometer mission QuikSCAT, and combines backscatter and brightness temperatures to define a 40% sea ice concentration.

Figure 2 displays an example of an ICESat derived Arctic Ocean sea ice freeboard map from the period February-March, 2003. The typical winter ice situation shows thicker sea ice North of Greenland forced against the coast by the Beaufort Gyre, and thinner ice in the Russian Arctic. Some residual track noise, e.g. north of Russia, is also apparent.

2.3 ICESat-derived Gravity Anomalies

Each of the mean sea surfaces computed from ICESat is cross-over adjusted, and the seven fields (listed in Table 1) are merged and draped into one combined MSS. This MSS is approximated to be the geoid by neglecting the MDT. The geoid is then inverted into gravity anomalies by techniques equivalent to the derivation of marine gravity anomalies from satellite radar altimetry over the open ocean. Here we have used Fast Fourier Transform (FFT).

In the computations we take into account only the longer wavelengths of the freeboards, and use a Wiener filtering method to suppress short-wavelength noise. In the Fourier domain it is expressed as

$$F(\Delta g) = G\frac{k}{1+ck^4}F(N) \qquad (4)$$

where F is the two-dimensional Fourier transform, k is the wave number, and c is a resolution constant described by Forsberg and Solheim (1988), and also by Andersen and Knudsen (1998). The above technique is used in combination with a remove-restore technique, to keep longer wavelengths from the global GRACE model GGM02S.

The resulting gravity anomalies corrected for sea ice freeboards can be seen in Figure 3. The gravity anomalies based on the ICESat data alone, compares qualitatively well to the Arctic Gravity Project's (ArcGP) gravity anomalies, cf. Figure 4, and maps nicely the major tectonic features, such as the Gakkel and Lomonosov Ridges, the deeper Canadian Basin, and the continental shelves. A similar procedure has been applied to compute the gravity anomalies with no sea ice corrections applied to the ICESat altimeter observations. The differences between these fields are outlined in the next chapter.

3 Evaluation of Results

3.1 Comparison to Airborne Campaigns

For a more quantitative comparison of the ICESat derived gravity anomalies, the two fields derived above (one not corrected for sea ice freeboards, and the other corrected for sea ice), together with the fields based on only two ICESat epochs from 2003 by Forsberg and Skourup (2004), are compared to high-resolution airborne gravity campaigns.

The airborne campaigns were carried out by the US Naval Research Laboratory (NRL) in the Arctic Ocean during the years 1992-99, and by the Danish National Space Center (DNSC) in the period 1998-2003. Four sub-regions have been selected for comparison, shown in Figure 5 by different colours. The NRL survey 1998-99 north of Svalbard, marked by red, are limited by latitudes 83-86°N, the DNSC survey north of Greenland (blue) are limited by 84-86°N, and the NRL surveys of 1995 (yellow) and 1994 (green) in the Canadian Arctic, are limited to a the latitude band 79-81°N. Biases between the 1994 and 1995 survey from NRL data are found, and therefore the data are divided into two regions.

Table 2 lists the mean and standard deviation of the differences between the ICESat gravity fields and the airborne gravimetry. It is seen that more data included to determine the gravity anomalies improves the estimated gravity field. In all but one case north of Greenland, the field is improved by taking the sea ice freeboard heights into account. For this particular area north of Greenland, with very compact ice, an airborne underflight of ICESat with high-resolution laser scanning (Forsberg, and Skourup, 2005), indicates that the freeboards based on ICESat are underestimated by approximately 35 cm, mainly due to imperfect lowest level filtering. The ICESat derived gravity anomalies, including data from 2003-05 and sea ice correction, are comparable to gravity anomalies based on 7 years of ERS data (S. Laxon, pers.comm.).

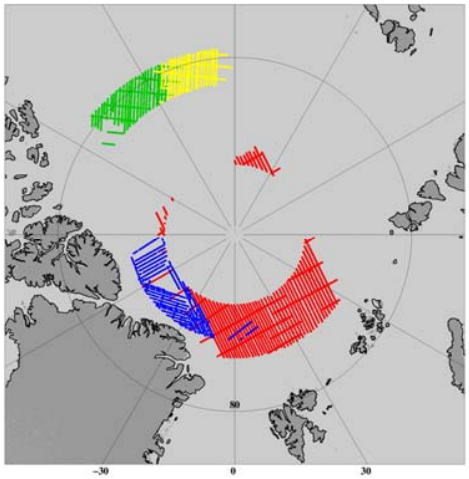

Fig. 5 Flight Lines from airborne gravity surveys used for evaluation of the ICESat gravity. NRL 98/99 survey (red), NRL 95 (yellow), NRL 94 (green), and DNSC survey 1998-2003 (blue).

Table 2 Comparison of gravity anomalies derived from ICESat and ERS to airborne gravity campaigns. NRL and DNSC are airborne campaigns carried out by the Naval Research Laboratory and the Danish National Space Center, respectively, each with an estimated accuracy around 2 mGal. The four airborne comparison regions are displayed the different colours in Fig. 5.

	NRL 98/99 (red)		DNSC 98-03 (blue)		NRL 95 (yellow)		NRL 94 (green)	
Gravity Field	mean	std.dev	mean	std.dev	mean	std.dev	mean	std.dev
ICESat 2003	-1.3	6.4	0.3	7.5	2.4	7.2	-11.5	10.9
ICESat 2003-5	-0.6	5.2	0.5	6.6	3.4	4.2	-10.8	9.4
ICESat 2003-5, ice corrected	-0.7	4.9	3.5	7.5	3.5	3.8	-10.8	9.3
ERS (Laxon)	-	-	-	-	-0.2	3.5	-14.3	9.1

4 Conclusions and Outlook

ICESat based gravity anomalies for the Arctic Ocean has been derived based on seven epochs of ICESat data (2003-05). By neglecting mean dynamic topography and sea ice freeboards the mean sea surface (MSS) for each ICESat epoch were merged and draped into a combined MSS, and inverted into gravity anomalies by FFT Wiener filtering methods. When validated to airborne gravity surveys it is concluded that the gravity field estimated from seven ICESat epochs is improved compared to gravity anomaly fields based on the hitherto only two available ICESat epochs from 2003. Thus, the more ICESat data available, the better gravity fields can be obtained, as expected.

A technique to estimate Arctic Ocean sea ice freeboard heights from ICESat data based on an along-track lowest level filtering was described and applied to the ICESat observations. The technique assumes the lowest levels to represent open water or thin ice in between the floes. The ICESat derived sea ice freeboards provides realistic Arctic Ocean freeboard heights with thicker ice north of Greenland, and thinner ice in the Russian Arctic.

The sea ice derived freeboards are used to see whether or not the gravity anomalies are improved by removing the sea ice from the observed ICESat altimeter data (h-F). By including freeboard corrections the gravity field improves in all regions except for the area north of Greenland, which are believed to be due to a combination of very compact ice conditions with few sufficiently large open leads or thin ice to allow reliable lowest-level filtering.

Overall the ICESat derived gravity anomalies compare qualitatively very well to the Arctic Gravity Project (ArcGP) gravity anomalies, and map in details the major tectonic features, such as the Gakkel and Lomonosov Ridges, the deeper Canadian Basin and the continental shelves. The ICESat gravity results will be used to improve the existing ArcGP gravity field models for the Arctic Ocean, especially for sectors north of Russia where some of the underlying data in ArcGP has a relatively poor resolution.

Future work for improved the ICESat gravity field should include corrections to the observed ICESat heights due to e.g. laser saturation, and the influence of the mean dynamic topography on the gravity fields should be investigated.

Acknowledgements

This work was done as part of the ArcGICE project, sponsored by the European Space Agency (ESTEC, contract officer M. Drinkwater). Thanks to John Brozena, NRL, for providing original airborne gravity data, and to S. Laxon, UCL, for providing the ERS 97W gravity grid based on ERS-1.

References

Andersen, O.B., and P. Knudsen (1998). Global marine gravity field from the ERS-1 and GEOSAT geodetic mission altimetry. *J. Geophys. Research, 103,* 8129-8137.

Dalå, N.S., R. Forsberg, K. Keller, H. Skourup, L. Stenseng, and S. M. Hvidegaard (2005). Airborne lidar measurements of sea ice north of Greenland and Ellesmere Island 2004. GreenICE/SITHOS/CryoGreen/A76 projects. *Final Report. Technical Report, Danish National Space Center.*

Forsberg, R., and H. Skourup (2005). Arctic Ocean Gravity, Geoid and Sea-ice Freeboard Heights from ICESat and GRACE. *Geophysical Research Letters, vol. 32, L21502.*

Forsberg, R., and D. Solheim (1988). Performance of FFT methods in local gravity field modeling. *Proceedings, Chapman Conference on Progress in the Determination of the Earths Gravity Field, AGU, Ft. Lauderdale.*

Hvidegaard, S.M., and R. Forsberg (2002). Sea ice thickness from airborne laser altimetry over the Arctic Ocean north of Greenland, *Geophysical Research Letters, vol. 29, no. 20, pp.1952-1955.*

Kenyon, S., and R. Forsberg (2001). Arctic Gravity Project – A status. *In Gravity, Geoid and Geodynamics 2000,*

International Association of Geodesy Symposia, Vol. 123, edited by M.G. Sideris, pp. 391-395, Springer, New York.

Kwok, R., G.F. Cunningham, H.J. Zwally, and D. Yi (2006). ICESat over Arctic sea ice: Interpretation of altimetric and reflectivity profiles. *Journal of Geophysical Research, vol. 111, C06006, doi: 10.1029/2005JC003175.*

Laxon, S., N. Peacock, and D. Smith (2003).High interannual variability of sea ice thickness in the Arctic Region, *Nature 425, 947-950.*

Padman, L., and S. Erofeeva (2004). A barotropic inverse tidal model for the Arctic Ocean. *Geophysical Research Letters, vol. 31, L02303, doi:10.1029/2003GL019003.*

Ray, R.D. (1999).A global ocean tide model from TOPEX/Poseidon altimetry: GOT99.2. *NASA Tech. Memo., 209478, 58 pp.*

GEOID, SEA LEVEL AND VERTICAL DATUM OF THE ARCTIC—IMPROVED BY ICESAT AND GRACE

GÉOÏDE, NIVEAU DE LA MER ET SYSTÈME DE RÉFÉRENCE ALTIMÉTIQUE DE L'ARCTIQUE—AMÉLIORÉS PAR ICESAT ET GRACE

Henriette Skourup and/et Rene Forsberg, Danish National Space Center, Copenhagen, Denmark
Centre spatial national danois, Copenhague, Danemark

Henriette Skourup
hsk@space.dtu.dk

Rene Forsberg
rf@space.dtu.dk

In the Arctic, a vertical reference system is typically based on local sea-level and tide-gauge observations. When using GPS for height measurement, a local geoid model, fitted to sea level, must therefore be used. Developments in satellite altimetry, such as NASA ICESat, which has since 2003 provided laser altimetry over the ice-covered regions up to 86°N, allows the direct measurement of sea level (or sea ice surface heights) even in narrow straits and fjords. Improved geoid models from GRACE, in combination with local gravity data, provide a new way to define a uniform vertical datum at sub-dm accuracy across larger regions of the Arctic, suitable for height measurement using GPS. This paper describes the use of ICESat laser altimetry data to estimate a mean sea surface (MSS) for the Arctic, using a low-level filtering method, in combination with an updated geoid model, based on updated surface, airborne and satellite gravity data (ArcGP and GRACE). As part of the ICESat MSS determination, we also determine sea ice freeboard heights, which show a good correlation to multi-year ice distribution as determined from QuikSCAT. Using the MSS and geoid model, the dynamic ocean topography can be determined. Some comparisons are shown of this ocean topography to oceanographic models derived in a recent ESA European-Canadian study called "ArcGICE". The variations in local ocean topography are the primary source of vertical datum offsets, and we illustrate the local variation of the sea-surface heights, tides and geoid by recent GPS profiles along fjords in western Greenland, carried out to validate local geoid models.

Dans la région arctique, le système de référence altimétrique est généralement basé sur le niveau de la mer local et les observations des marégraphes. Lorsqu'on utilise le GPS pour mesurer la hauteur, un géoïde local, adapté au niveau de la mer, doit alors être utilisé. Les développements en matière d'altimétrie satellitaire, tels que ceux avec ICESat de la NASA, qui fournit depuis 2003, une altimétrie laser sur les régions recouvertes de glace jusqu'à la latitude 86°N, permettent une mesure directe du niveau de la mer (ou des hauteurs par rapport à la surface des glaces de mer), même dans des détroits et fjords étroits. Ces développements, associés aux géoïdes améliorés de GRACE, en lien avec les données gravimétriques locales, devraient offrir une nouvelle manière de définir une référence altimétrique uniforme à une exactitude sous décimétrique dans les plus grandes régions arctiques, compatibles avec le GPS. Dans cet article, nous utilisons les références altimétriques laser ICESat afin d'estimer une surface moyenne des mers en Arctique, à l'aide d'une méthode de filtre du plus bas niveau, associée à un modèle du géoïde mis à jour, basé sur des données gravimétriques mises à jour par moyens terrestres, aéroportés et satellitaires (ArcGP et GRACE). Dans le cadre de la détermination de la surface moyenne des mers avec ICESat, nous définissons également les hauteurs du franc-bord des glaces de mer, qui montrent une belle corrélation avec la distribution pluriannuelle de glace, comme identifié par QuikSCAT. À l'aide de la surface moyenne des mers et du géoïde, la topographie dynamique de l'océan peut être déterminée. Nous donnons des exemples de comparaison entre cette topographie de l'océan et des modèles océanographiques; ces exemples sont tirés d'une récente étude de l'Agence spatiale européenne, intitulée « ArcGICE », étant une coopération canado-européenne. La variation de la topographie locale de l'océan est la source principale des écarts en matière de référence altimétrique; nous illustrons la variation locale des hauteurs de la surface des mers, des marées et du géoïde grâce à des profils GPS récents effectués le long des fjords du Groenland occidental pour valider les modèles du géoïde local.

1. Introduction

The geoid is the fundamental reference height surface, corresponding to the undisturbed world ocean level. With improved absolute accuracy in geoid modelling due to satellite gravity field missions, notably GRACE [*Tapley et al*. 2004], and

…the geoid is known in an absolute sense to better than 10 cm over large parts of the Arctic.

improved detailed gravity field information from surface, airborne and satellite altimetry, such as that compiled in the Arctic Gravity Project [*Forsberg and Kenyon* 2004], the geoid is known in an absolute sense to better than 10 cm over large parts of the Arctic. One application of the geoid model is in the determination of heights on land by GPS

$$H = h - N \quad (1)$$

where H is the orthometric height, h the GPS ellipsoidal height and N the geoid height. Another is at sea, to determine the mean dynamic topography (MDT) from measurements of ocean ellipsoidal heights from satellite altimetry

$$MDT = h - N \quad (2)$$

The heights h at sea are often compiled in a mean sea surface (MSS) grid, referring to a particular epoch, because the ocean heights tend to show decadal variations at the 10-cm level or more [*Forsberg et al*. 2007].

In practice, vertical datums in the Arctic are determined from local sea level observations, either at communities or at tide points in the few older trigonometric networks available (e.g., along the Greenland west coast). In such cases it is not the geoid which is the reference surface, but rather the N+MDT; therefore geoid models for practical use for geospatial referencing and urban use are usually fitted locally to GPS and levelling or tide gauge data, providing a "GPS geoid" which is no longer an equipotential surface in the gravity field. With advances in the accuracy of MSS and MDT determination, both from satellite methods and oceanographic models, there is now an opportunity to define a more consistent vertical reference system across larger arctic regions, linked to a global vertical datum (W_0), soon to be adopted by the International Association of Geodesy.

In this paper, we give some examples of the current status of geoid determination, MSS and MDT in the Arctic Ocean region, based on new satellite missions GRACE and ICESat [*Zwally et al. 2002*]. Our results provide some indication of future possibilities with the upcoming satellites GOCE and CryoSat. For coastal arctic regions, local irregularities in the geoid and MDT limit the transfer of open ocean results, especially as they affect the determinations of the geoid in mountainous and fjord areas where limited gravimetric data can reveal major variations in the geoid. Such effects can readily be measured with GPS. We conclude the paper with an example from western Greenland, where GPS measurements of N+MDT are made in winter on frozen fjords, primarily to evaluate geoid models.

1. Introduction

Le géoïde est la surface de référence fondamentale de la hauteur, correspondant au niveau qu'aurait l'océan s'il n'y avait pas de continents. Grâce à l'exactitude absolue améliorée en matière de modèles du géoïde, due aux missions satellitaires sur le champ gravitationnel, notamment GRACE [*Tapley et coll*. 2004], et de l'information détaillée améliorée sur le champ gravitationnel tirée de l'altimétrie obtenue par des moyens terrestres, aéroportés et satellitaires, p. ex. compilés dans l'Arctic Gravity Project [*Forsberg et Kenyon* 2004], le géoïde est connu dans un sens absolu, à mieux de 10 cm sur de grands espaces de l'Arctique. Les deux applications principales du géoïde sont, dans les régions terrestres, la détermination des hauteurs par GPS

$$H = h - N \quad (1)$$

où H est la hauteur orthométrique, h la hauteur ellipsoïdale du GPS et N l'ondulation du géoïde (ou la hauteur au-dessus du géoïde). Dans l'océan, l'application principale est océanographique, afin de déterminer la topographie dynamique moyenne (TDM) à partir des mesures des hauteurs ellipsoïdales de l'océan, tirées de l'altimétrie satellitaire

$$TDM = h - N \quad (2)$$

Dans les océans, les hauteurs h sont souvent compilées dans une grille de surfaces moyennes des mers, qui correspond à une époque particulière, car les hauteurs de l'océan ont tendance à montrer des variations décennales de l'ordre de 10 cm ou plus [*Forsberg et coll*. 2007].

Dans la pratique, les références altimétriques en Arctique sont définies à partir d'observations locales du niveau de la mer, soit dans des communautés soit à des points de mesure des marées dans les quelques réseaux trigonométriques plus anciens disponibles (p. ex. le long de la côte ouest du Groenland). Dans de tels cas, le géoïde n'est pas la surface de référence; il s'agit plutôt de N+TDM. Ainsi, les modèles du géoïde pour une utilisation pratique pour un référencement géospatial et un usage urbain sont en général ajustés au GPS local et aux données de nivellement ou aux données des marégraphes. Ces modèles proposent un « géoïde GPS », qui ne correspond plus à une surface équipotentielle dans le champ gravitationnel. Grâce aux avancées en matière de précision du niveau moyen des mers et de la topographie dynamique moyenne (TDM), déterminés grâce aux méthodes satellitaires et aux modèles océanographiques, il est aujourd'hui possible de définir un système de référence altimétrique plus fidèle sur de plus grandes régions arctiques; ce système est lié à une référence altimétrique mondiale

2. Geoid of the Arctic Region

The Arctic Region has been the focus of various bathymetric and gravimetric activitie, since the early 1990's, following the end of the Cold War. The Arctic Gravity Project (ArcGP) was initiated in 1998 as a cooperative project under the International Association of Geodesy, following in the footsteps of earlier cooperative compilations of bathymetric data and magnetic data. The ArcGP released the first 5' x 5' gravity data and terrain grids, including major classified datasets from U.S. and Russian sources by 2002; see *earth-info.nga.mil/GandG/wgs84/agp/index.html*. The grids cover all areas north of 64°N, with extensions for southern Greenland and Iceland. The latest release (February 2006) includes additional surface and ICESat-derived gravity data.

The gravity data available for the compilation includes surface (ground, helicopter and marine) data, airborne data and submarine data, each with special error characteristics in terms of both accuracy and resolution. Some data, especially from Russia, was presented in the form of grids derived from digitized gravity maps. Along with these data types, satellite altimetry has been used over some ice-free and ice-covered areas up to the limits of ERS-1 coverage at 81.5°N.

Of special importance for the filling of the High Arctic polar gap has been the long-range airborne gravity surveys using spring-type gravimeters and kinematic GPS techniques for georeferencing. Airborne gravity holdings in the Arctic are currently the predominant data source over the Arctic Ocean and Greenland and are primarily the results of surveys by the U.S. Naval Research Laboratory [*Brozena and Salman* 1996], see Figure 1. The Naval Research Laboratory (NRL) Arctic Ocean surveys followed the successful pioneering aerogravity coverage of Greenland by high-altitude surveys 1991-92 [*Forsberg and Sideris* 1993]. In addition, airborne gravity surveys by Russian, Canadian and Danish/Norwegian sources have been used. Airborne gravity accuracy has developed significantly since the early 1990's, with recent surveys having a typical accuracy of 1.5-2 mGal r.m.s. (1 mGal = 10^{-5} m/s^2), at a resolution of 6-15 km, depending on aircraft speed.

The final combination of all data from airborne, submarine and surface data was done using least-squares collocation gridding and draping methods. Over Greenland and Svalbard, high-altitude airborne gravity data from NRL and the Danish National Survey and Cadastre were reduced to the surface. Only over Siberia (east of 60°E) and for a few minor

(W_0), qui sera bientôt adoptée par l'Association internationale de géodésie.

Dans cet article, nous vous donnerons quelques exemples de l'état actuel du géoïde, de la surface moyenne des mers et de la topographie dynamique moyenne dans la région de l'océan Arctique, d'après de nouvelles missions par satellite, GRACE et ICESat [*Zwally et al. 2002*]. Nos résultats sont seulement des indications sur de futures possibilités, avec les satellites à venir, GOCE et CryoSat. Dans les régions côtières de l'Arctique, les irrégularités locales du géoïde et de la topographie dynamique moyenne limitent le transfert des résultats pour la pleine mer; par exemple, le comportement du géoïde dans les zones montagneuses et les fjords, associé à des données gravimétriques limitées, peut produire des variations majeures du géoïde. De tels effets peuvent être facilement mesurés avec le GPS. Nous concluons cet article avec l'exemple du Groenland occidental, où les mesures GPS de N+TDM sont effectuées en hiver dans des fjords gelés, principalement pour évaluer des modèles du géoïde.

2. Le géoïde de la région arctique

La région arctique est au centre de diverses activités bathymétriques et gravimétriques depuis le début des années 1990, à la suite de la guerre froide. L'Arctic Gravity Project (ArcGP) a été lancé en 1998, dans le cadre d'une coopération au sein de l'Association internationale de géodésie. Il faisait suite à une précédente compilation coopérative de données bathymétriques et magnétiques. L'ArcGP a publié en 2002, les premières données gravimétriques et grilles du terrain (5' x 5'), y compris d'importants jeux données classifiées tirées de sources américaines et russes (voir *earth-info.nga.mil/GandG/wgs84/agp/index.html)*. Les grilles couvrent toutes les zones au nord de la latitude 64°N, avec des prolongements pour le sud du Groenland et de l'Islande. La dernière publication (février 2006) inclut des données gravimétriques supplémentaires dérivées de mesures à la surface et à partir d'ICESat.

La région arctique est au centre de diverses activités bathymétriques et gravimétriques depuis le début des années 1990…

Les données gravimétriques disponibles à la compilation incluent des données de la surface (sol, hélicoptère et en mer), des données aéroportées et des données sous-marines. Chacune d'elles contient des caractéristiques d'erreurs spéciales en termes de précision et de résolution. Certaines données, notamment celles venues de Russie, ont été présentées sous la forme de grilles dérivées de cartes gravimétriques numérisées. Associée à ces types de données, l'altimétrie satellitaire a été utilisée sur

data voids in the Arctic Ocean was the global model EGM96 used for grid cell fill-ins. The final Arctic Gravity Project gravity grid is shown in Figure 2.

Geoid models are determined from available airborne and surface gravimetric data using a remove-restore technique, where a reference field based on GRACE data is removed from the free-air gravity data, and subsequently restored in the final geoid modelling. The gravity to geoid conversion of the residual gravity signal is done by spherical FFT, using the bandwise approach derived in [*Forsberg and Sideris* 1993], where the geoid signal is obtained by a number of bandwise Fourier transformations of the form

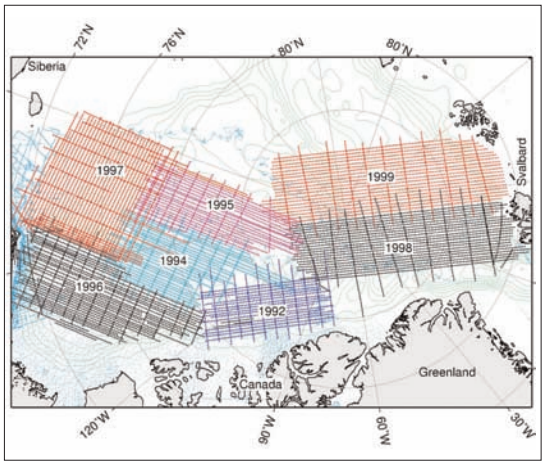

Figure 1: Tracks from the Naval Research Laboratory's airborne gravity surveys in the Arctic, 1992-1999. / Figure 1 : Traces tirées des levés gravimétriques aéroportés en Arctique du Naval Research Laboratory, 1992-1999.

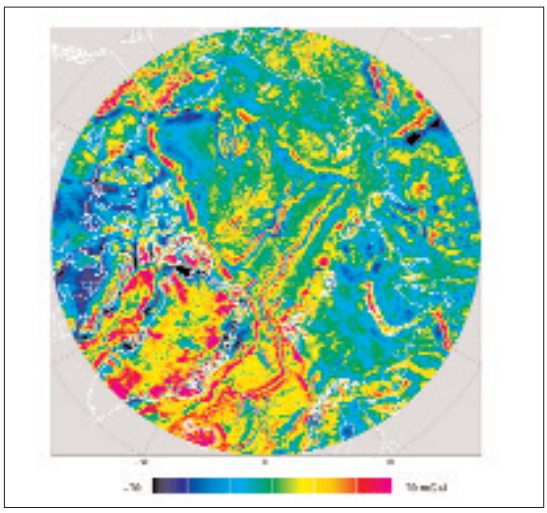

Figure 2: Gravity anomalies of ArcGP. / Figure 2 : Anomalies de la pesanteur d'ArcGP.

des zones sans glace et des zones couvertes de glace jusqu'à la limite de la couverture de ERS-1 à la latitude 81,5°N.

Les levés gravimétriques aéroportés à longue distance ont été particulièrement importants pour combler le grand vide de données polaires en Arctique. Ces levés ont été menés à l'aide de gravimètres à ressort et de techniques GPS cinématiques pour le géoréférencement. Les données gravimétriques aéroportés en Arctique sont actuellement la principale source de données pour l'océan Arctique et le Groenland. Elles résultent principalement de levés menés par le Naval Research Laboratory américain [*Brozena et Salman* 1996] (voir figure 1). Les levés de l'océan Arctique du Naval Research Laboratory ont suivi la couverture aérogravimétrique d'avant-garde du Groenland, réussie grâce à des levés en haute altitude en 1991-1992 [*Forsberg et Sideris* 1993]. Par ailleurs, on a utilisé des levés gravimétriques aéroportés effectués par des sources russes, canadiennes et danoises ou norvégiennes. En général, la précision de la gravité aéroportée s'est beaucoup améliorée depuis le début des années 1990. Les levés récents ont une précision type de 1,5-2 mGal (moyenne quadratique) (1 mGal = 10^{-5} m/s^2), avec une résolution de 6-15 km, selon la vitesse de l'aéronef.

La combinaison finale de toutes les données gravimétriques tirées des données aéroportées, terrestres et sous-marines a été réalisée à l'aide de méthodes de maillage et de moulage incluant une collocation par moindres carrés. Au-dessus du Groenland et de Svalbard, la cueillette des données gravimétriques aéroportées en haute altitude tirées du Naval Research Laboratory et du Danish National Survey and Cadastre a été prolongée à la surface. En Sibérie seulement (à l'est de la latitude 60°E) et aussi pour quelques vides de données mineurs dans l'océan Arctique, le modèle international EGM96 a été utilisé pour compléter les cellules de la grille. La grille gravimétrique finale de l'Arctic Gravity Project est présentée à la figure 2.

Les modèles du géoïde sont déterminés à partir des données gravimétriques disponibles des missions aéroportée et terrestre, à l'aide d'une technique supprimer-restaurer, dans laquelle un champ de référence basé sur les données GRACE est supprimé des données gravimétriques à l'air libre, puis restauré subséquemment dans le géoïde final. La conversion de la gravité au géoïde du signal gravimétrique résiduel est effectuée par la transformée de Fourier rapide (TFR) sphérique, à l'aide d'une approche par bande, élaborée dans [*Forsberg et Sideris* 1993], où le signal du géoïde est obtenu par une série de transformées de Fourier par bande

$$N = F^{-1}[F(S)\,F(\Delta g \sin\phi)] \qquad (3)$$

where F is the two-dimensional Fourier transform, N the geoid, Δg the gravity anomaly, ϕ the latitude, and S the classical Stokes' function. For practical computations a modified Stokes' function

$$s'(\psi) = \sum_{l=N}^{\infty} \frac{2l+1}{l-1} w_1 p_l(\cos\psi) \qquad (4)$$

is used. This allows only the shorter and medium wavelengths of the geoid to be determined, with the GRACE reference field geoid in principle determining the longest wavelengths (here l > 90). Figure 3 shows the computed geoid model of the Arctic, also available from the ArcGP Website.

3. MSS and MDT from ICESat and ERS

Over the oceans, satellite altimeters in principle map the MSS after correction for tides. This process is complicated in the Arctic Ocean by the presence of sea ice. Here it is necessary to estimate and remove the sea-ice freeboard height (the part of the sea ice above sea level) from the altimetry measurements to obtain the MSS

$$MSS = h - F = N + MDT \qquad (5)$$

where h is the ellipsoidal height of the altimetry measurements corrected for tides, F the freeboard height, N the geoid, and MDT the mean dynamic topography. In the above equation, MDT is the quantity of primary interest in oceanography, MSS is the link between local datums based on mean sea

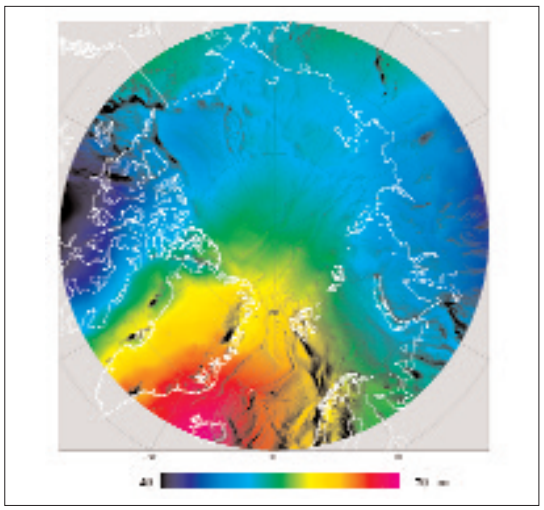

Figure 3: Shaded relief geoid model of the Arctic region. / Figure 3 : Modèle du géoïde en relief par ombres portées de la région arctique.

$$N = F^{-1}[F(S)\,F(\Delta g \sin\phi)] \qquad (3)$$

où F est la transformée de Fourier en deux dimensions, N est le géoïde, Δg l'anomalie de la pesanteur, ϕ la latitude et S la fonction de Stokes classique. Pour les calculs pratiques, une fonction de Stokes modifiée

$$s'(\psi) = \sum_{l=N}^{\infty} \frac{2l+1}{l-1} w_1 p_l(\cos\psi) \qquad (4)$$

est utilisée. Elle permet seulement de déterminer les longueurs d'ondes plus courtes et moyennes du géoïde, avec le géoïde du champ de référence GRACE déterminant, en principe, les plus longues longueurs d'ondes (ici l > 90). La figure 3 présente le modèle du géoïde calculé de l'Arctique, également disponible à partir du site Web de l'ArcGP.

3. Surface moyenne des mers et TDM tirées d'ICESat et d'ERS

Au-dessus des océans, les altimètres des satellites cartographient en principe la surface moyenne des mers après correction pour les marées. La présence des glaces de mer complique ce procédé dans l'océan Arctique. Pour obtenir la surface moyenne des mers à cet endroit, il est nécessaire d'estimer, puis d'enlever la hauteur du franc-bord des glaces de mer (partie des glaces de mer au-dessus du niveau de la mer) des mesures altimétriques.

Surface moyenne des mers

$$(SMM) = h - F = N + TDM \qquad (5)$$

ici, h est la hauteur ellipsoïdale des mesures altimétriques corrigées pour les marées, F correspond aux francs-bords, N est le géoïde et TDM la topographie dynamique moyenne. Dans l'équation ci-dessus, TDM est la quantité de première utilité en océanographie, SMM est le lien entre les références locales basées sur le niveau moyen des mers, et F est en soi très intéressant, car il est directement lié à l'épaisseur des glaces de mer.

Des techniques récentes, élaborées pour estimer les francs-bords des glaces de mer tirés de l'altimétrie, utilisent la mer libre ou de fins chenaux de glace dans la couche des glaces de mer, pour obtenir une référence pour les hauteurs de la surface locale de la mer. Identifiant ainsi les retours de chenaux libres et corrigeant pour les marées, une surface moyenne des mers peut être trouvée. Pour les altimètres radar conventionnels (p. ex. ERS), le diamètre d'une empreinte mesure en général plusieurs kilomètres de largeur, soit bien plus que la majorité des chenaux libres de l'Arctique. Dans ce

Recent techniques developed to estimate sea-ice freeboard from altimetry use open water or thin-ice leads within the sea-ice cover to get a reference for the local sea surface heights.

level, and F is by itself of strong interest, since it is directly related to sea-ice thickness.

Recent techniques developed to estimate sea-ice freeboard from altimetry use open water or thin-ice leads within the sea-ice cover to get a reference for the local sea surface heights. Thus identifying the returns from open leads and correcting for tides, an MSS can be found. For conventional radar altimeters (e.g. ERS), the footprint diameters are typically several kilometres wide, much wider than most of the open leads in the Arctic. In this case, the leads can be identified by a characteristic peak in the returned waveform [*Laxon et al*. 2003]. For laser altimetry, the relatively narrow footprint (~70 m for ICESat) is believed to better detect the larger open leads, and the open water can be identified locating the lowest levels in the geoid-reduced measured altimeter heights. The method was first described by [*Hvidegaard and Forsberg* 2002] for airborne lidar measurements and has recently been adapted to be used for ICESat by [*Forsberg and Skourup* 2005].

Using the above-mentioned techniques, a composite MSS for the entire Arctic Ocean is estimated by using altimetry from ERS (1995-2003), kindly provided by University College London (UCL), and 7 epochs of ICESat data (2003-2005), with the ArcGP geoid draped in areas north of 86°N to close the polar gap. Because of differences in epochs and reference systems, we have adopted the WGS84 data of ERS as reference. The draping technique uses the ERS MSS as reference in the overlap band 79-81.5°N, and is essentially a collocation approach, where the difference

$$\varepsilon = SSH_{ERS} - SSH_{ICESat} \quad (6)$$

is modelled by a bias and a random function. The result of the composite MSS is seen in Figure 4.

Figure 5 shows an example of an ICESat-derived Arctic Ocean sea-ice freeboard map for the period February—March, 2003. An open-water mask is applied to remove false freeboard heights over open ocean, originating from the lowest-level algorithm favouring the trough of the waves. The mask is obtained from SeaWinds scatterometer mission QuikSCAT, and combines backscatter and brightness temperatures to define a 40% sea-ice concentration. In the figure, the typical winter ice situation shows thicker sea ice North of Greenland forced against the coast by the Beaufort Gyre, and thinner ice in the Russian Arctic. Some residual track noise, e.g. north of Russia, is also apparent.

If a geoid model (in this case, the most updated release from ArcGP, February 2006) is subtracted from the MSS based on satellite altimetry measurements, the mean dynamic topography (MDT) is

cas, les chenaux peuvent être identifiés par un pic particulier dans l'oscillogramme retourné [*Laxon et coll*. 2003]. Pour l'altimétrie laser, l'empreinte relativement étroite (~70m pour ICESat) est censée mieux détecter les plus grands chenaux libres, et la mer libre peut être identifiée en localisant les niveaux les plus bas dans les hauteurs altimétriques mesurées et réduites au géoïde. La méthode a été présentée pour la première fois par [*Hvidegaard et Forsberg* 2002] pour les mesures lidar aéroportées et a récemment été adaptée pour être utilisée pour ICESat par [*Forsberg et Skourup* 2005].

À l'aide des techniques mentionnées ci-dessus, une surface moyenne des mers composée pour la totalité de l'océan Arctique est estimée en utilisant l'altimétrie ERS (1995-2003), gracieusement offerte par le University College London (UCL), ainsi que 7 époques de données ICESat (2003-2005), tandis que le géoïde du projet ArcGP moule le nord de la latitude 86°N, pour combler le fossé de données polaires. À cause des différences d'époques et de systèmes de référence, nous avons adopté les données WGS84 d'ERS comme référence. La technique de moulage utilise la surface moyenne des mers d'ERS comme référence dans la bande de recouvrement 79-81,5°N; elle est principalement une approche de collocation, où la différence

$$\varepsilon = HSM_{ERS} - HSM_{ICESat} \quad (6)$$

est modélisée par un biais et une fonction aléatoire. Le résultat de la surface moyenne des mers (SMM) composée est présenté à la figure 4.

La figure 5 présente l'exemple d'une carte du franc-bord des glaces de mer de l'océan Arctique dérivée d'ICESat pour la période de février et mars 2003. Un masque de la mer libre est appliqué, afin d'éliminer les mauvaises hauteurs du franc-bord au-dessus de l'océan libre, découlant de l'algorithme du plus bas niveau qui favorise le creux des vagues. Le masque est obtenu grâce à la mission du diffusiomètre radar SeaWinds QuikSCAT. Ce dernier associe les températures de rétrodiffusion et de brillance pour définir une concentration de 40 % des glaces de mer. Sur la figure, l'état typique de la glace en hiver montre des glaces de mer plus épaisses au nord du Groenland, poussées contre la côte par le tourbillon Beaufort, et des glaces plus fines dans l'Arctique russe. Un certain bruit résiduel de suivi, p. ex. au nord de la Russie, apparaît également.

Si un modèle du géoïde (ici, utilisation de la dernière publication mise à jour de l'ArcGP, février 2006) est soustrait de la surface moyenne des mers, d'après des mesures altimétriques satellitaires, la topographie dynamique moyenne (TDM) est obtenue (équation 2) en cartographiant les modèles

obtained, (Equation 2), mapping the permanent ocean circulation patterns. For the first time, an MDT from observations is obtained in the Arctic. The result is presented in Figure 6 (left), and maps the high values toward the Canada side representing the Beaufort Gyre, and low values north of Russia in continuation of the MDT low in the Greenland/Norwegian Seas.

For comparison, two coupled ice-ocean models are also shown in Figure 6. These represent a model developed by the University of Washington (UW) [*Steele et al.* 2004] and [*Morison et al.* 2006], and the Polar Ice Prediction System (PIPS)

permanents de circulation de l'océan. Une TDM tirée d'observations est obtenue pour la première fois en Arctique. Le résultat est présenté à la figure 6 (gauche); il montre les hautes valeurs sur le flanc canadien, représentant le tourbillon de Beaufort, et les faibles valeurs au nord de la Russie, en continuation de la TDM, qui est basse dans la mer du Groenland et la mer de Norvège.

En comparaison, deux modèles glace-océan associés sont également présentés à la figure 6. Ils représentent un modèle conçu par l'Université de Washington (UW) *[Steele et coll.* 2004] et [*Morison et coll.* 2006] et le système de prédiction

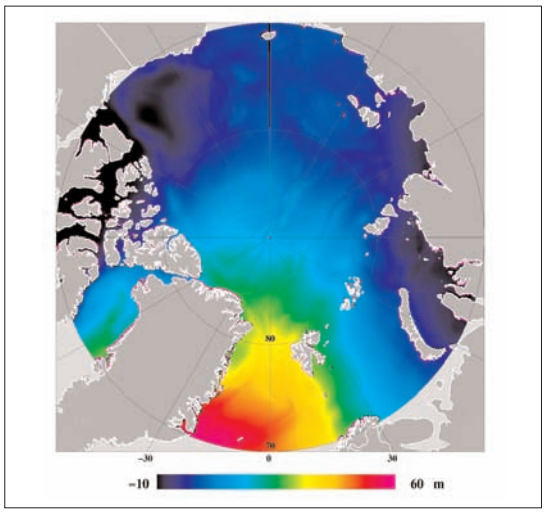

Figure 4: Composite MSS from ERS and ICESat, with ArcGP draped in around the North Pole. / Figure 4 : Surface moyenne des mers composée d'ERS et d'ICESat, avec l'ArcGP moulé autour du pôle Nord.

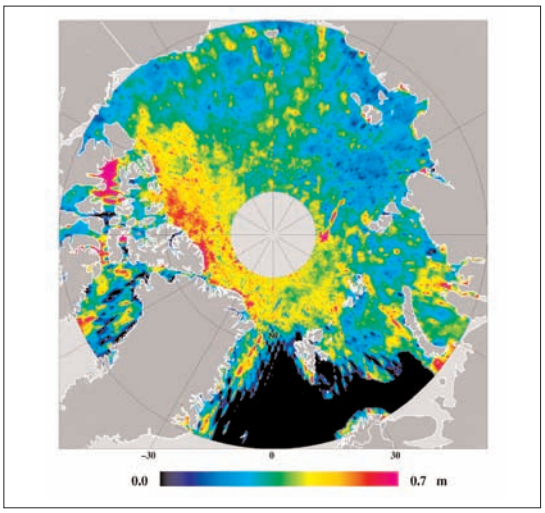

Figure 5: Map of sea-ice freeboard heights in the Arctic Ocean derived from ICESat data February—March, 2003. / Figure 5 : Carte des hauteurs du franc-bord des glaces de mer dans l'océan Arctique, dérivées des données ICESat, février-mars 2003.

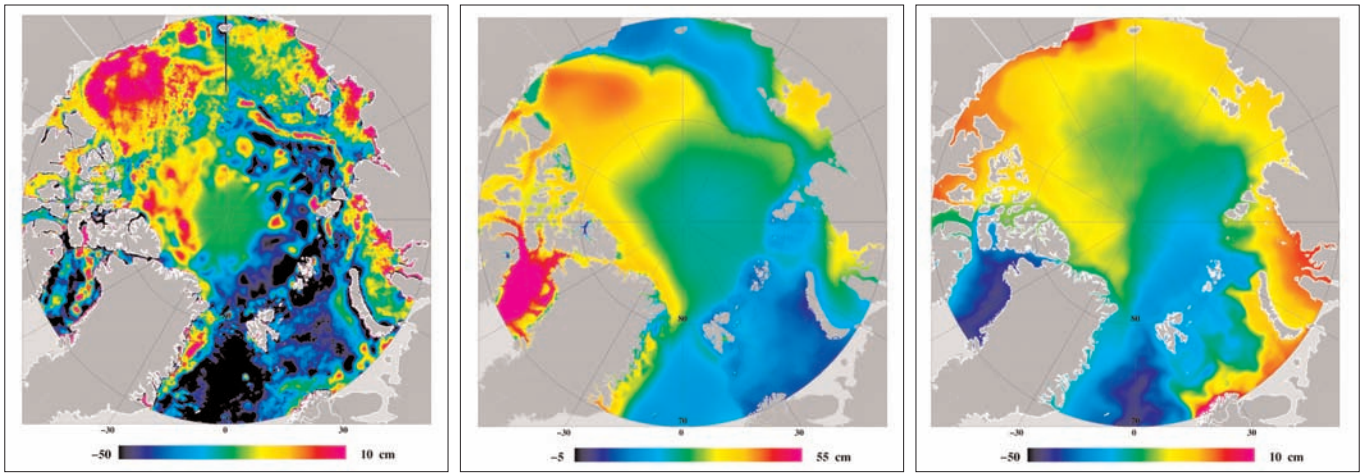

Figure 6: MDT determined from the composite Arctic Ocean MSS (left). Modelled MDT from UW 1955-2006 (centre), and PIPS 1995-2003 averaged for March only (right). The MDT surfaces have different reference levels, but the scales are given within the same interval (60 cm). / Figure 6 : Topographie dynamique moyenne (TDM) déterminée à partir de la surface moyenne des mers composée de l'océan Arctique (gauche). TDM modélisée à partir du modèle de l'UW 1955-2006 (centre) et des moyennes du système de prédiction de la glace polaire (SPGP)1995-2003 pour mars seulement (droite). Les surfaces de la TDM ont des niveaux de référence différents, mais les échelles sont données dans le même intervalle (60 cm).

from the U.S. Naval Postgraduate School. The PIPS model is a high-resolution, 9-km eddy-resolving model, whereas UW is a lower resolution model with an average resolution around 40 km. The oceanographic models show large differences; however, the overall circulation patterns are reproduced.

The MDT observed from "remote sensing" compares reasonably with oceanographic models, especially the UW model; thus the potential of space-based methods for MDT determination are noted. The ability to map changes in the MDT, and thus the underlying ocean circulation, could in principle provide new constraints on oceanographic models of the region, especially with improved MDT from future satellite missions like CryoSat and GOCE. This could, moreover, provide insight into the basal melting process of the sea ice, since the changing inflow of Atlantic and Pacific waters is believed to be a major source of currently observed sea-ice thickness changes.

4. Local Measurements of MSS by GPS and Tide Gauges in Greenland

Le géoïde des zones côtières montagneuses montre de grandes variations, liées à la topographie, aux systèmes de fjords profonds et à la géologie.

The geoid in mountainous coastal areas shows large variations related to topography, deep fjord systems and geology. Also, tidal variations are large, as is the MDT. In this chapter, we describe a small experiment, carried out over 5 days in April 2005, to directly measure the sea surface topography along a 150-km long profile from the outer coast to the ice sheet in the Uummannaq area of west Greenland. The area is mountainous with some peaks higher than 2,000 m elevation, and fjord depths in excess of 1,500 m, (Figure 7). The purpose of the experiment was to provide geoid "ground truth" data to evaluate geoid model accuracy, especially with a view to the proper weighting of airborne and surface data in the medium-range wavelength band. Greenland is unique since a complete airborne gravity survey was already done in 1991-92, in the infancy of operational airborne gravity [*Brozena* 1991]; however, data biases and biases from unknown terrain masses (fjord depths, ice thickness) affecting necessary terrain reductions and downward reduction provide a potentially serious source of geoid error.

The SSH was measured by GPS on the frozen fjords. Two classes of stations were used: 1) long-term (12-24hr) GPS stations processed as kinematic data following the tidal movements, and 2) supplementary short-term GPS occupations at shorter

de la glace polaire (SPGP) de la Naval Postgraduate School américaine. Le modèle SPGP est un modèle de résolution des turbulences en haute résolution de 9 km, tandis que celui de l'UW a une résolution plus faible, avec une moyenne de 40 km. Les modèles océanographiques montrent de grandes différences; cependant, les modèles de circulation généraux sont tout de même reproduits.

La topographie dynamique moyenne (TDM) observée par « télédétection » présente une comparaison raisonnable avec les modèles océanographiques, notamment le modèle de l'UW; le potentiel des méthodes spatiales pour la détermination de la TDM est ainsi souligné. La possibilité de cartographier les changements dans la TDM, et ainsi dans la circulation océanique sous-jacente, pourrait en principe fournir de nouvelles contraintes sur les modèles océanographiques de la région, notamment avec une TDM améliorée, tirée de futures missions par satellite comme CryoSat et GOCE (Mission d'étude du champ gravitationnel et des paramètres permanents de la circulation océanique). Ceci pourrait également fournir des indices sur le processus de fonte de la base des glaces de mer, car l'apport variable des eaux de l'Atlantique et du Pacifique est censé être une source majeure de changements dans l'épaisseur des glaces de mer actuellement à l'étude.

4. Mesures locales de la surface moyenne des mers par GPS et par marégraphes au Groenland

Le géoïde des zones côtières montagneuses montre de grandes variations, liées à la topographie, aux systèmes de fjords profonds et à la géologie. De plus, les variations de la marée sont également grandes, ainsi que celles de la topographie dynamique moyenne. Dans cette section, nous décrivons une petite expérience, menée pendant 5 jours en avril 2005, afin de mesurer directement la topographie de la surface marine sur un profil de 150 km de long, du rivage extérieur à la nappe glaciaire dans la région d'Uummannaq dans l'ouest du Groenland. La zone est une région montagneuse dont les montagnes dépassent les 2 000 m d'altitude, et la profondeur des fjords dépasse 1 500 m (voir la figure 7). Le but de l'expérience était de fournir des données du géoïde en « réalité terrain », afin d'évaluer la précision du modèle du géoïde, notamment la pondération adéquate des données aéroportées et terrestres dans la bande des longueurs d'ondes moyennes. Le Groenland est unique car un levé gravimétrique aéroporté complet

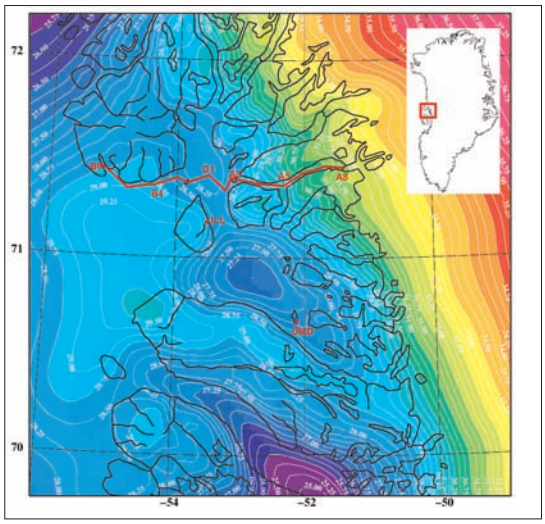

Figure 7: SSH profile measured in western Greenland, shown on a map of the geoid (25 cm contour interval). The numbers along the profile are the "kinematic" ice GPS points. Reference GPS and tide gauge were at the settlements of Illorsuit (ILL) and Uummannaq (UMD). / Figure 7 : Profil pour la hauteur de la surface de la mer (HSM) mesuré au Groenland occidental, présenté sur une carte du géoïde (équidistance de 25 cm). Les nombres le long du profil sont les points GPS de glace « cinématiques ». La référence du GPS et des marégraphes se trouvaient dans les communautés d'Illorsuit (ILL) et d'Uummannaq (UMD).

distances from the "kinematic" stations, or the semi-permanent GPS reference station at the settlement of Illorssuit. Two temporary tide gauges were used to monitor sea level (at Illorssuit and the larger village of Uummannaq). The tide-gauge data were used to refer stations to average sea level at Uummannaq, and sea-ice snow depth and freeboard were measured by drilling, in order to refer GPS heights directly to sea level. An example of kinematic GPS solutions and tide-gauge data is shown in Figure 8.

From the combined GPS and tide gauge measurements, the SSH was derived relative to average sea-level at Uummannaq. ICESat might also be able to measure directly the SSH (or sea ice surface) in the fjords due to the relatively narrow footprint (~70m in diameter). Figure 9 plots the ICESat ellipsoidal heights corrected for tides, showing the tracks available from the period February 17-March 24, 2005. Because the MDT in the area is assumed to be nearly constant, the measured SSH variations can be treated as geoid variations. Figure 10 shows the two SSH profiles as measured by GPS and ICESat, together with two different geoid models. The ICESat values are extracted by gridding the tracks from Figure 9. The geoid models are

avait déjà été effectué en 1991-1992, dans les débuts de la gravimétrie aéroportée opérationnelle [*Brozena* 1991]. Cependant, les biais des données et les biais provenant des masses inconnues du terrain (profondeur des fjords, épaisseur de la glace) dans les réductions nécessaires du terrain et la continuation dégressive, fournissent une source d'erreur du géoïde potentiellement sérieuse.

La hauteur de la surface de la mer a été mesurée par GPS dans les fjords gelés. Deux classes de stations ont été utilisées : 1) stations GPS à long terme (12-24 heures) traitées comme données cinématiques suivant les mouvements de la marée et 2) stations GPS supplémentaires à court terme à de plus courtes distances des stations « cinématiques », ou la station de référence GPS semi-permanente dans la communauté d'Illorsuit. Deux marégraphes temporaires ont été utilisés pour surveiller le niveau de la mer (à Illorsuit et dans le plus grand village de Uummannaq). Les données des marégraphes ont été utilisées pour référencer les stations au niveau de la mer à Uummannaq; les glaces de mer, la profondeur de la neige et le franc-bord ont été mesurés en forant afin de référencer directement les hauteurs de GPS au niveau de la mer. Un exemple de solutions GPS cinématiques et de données des marégraphes est présenté à la figure 8.

À partir des mesures combinées du GPS et des marégraphes, la hauteur de la surface de la mer est obtenue relativement au niveau de la mer moyen à Uummannaq. ICESat pourrait aussi être capable de mesurer directement la hauteur de la surface de la mer (ou la surface des glaces de mer) dans les fjords, grâce à l'empreinte relativement étroite (~70 m de

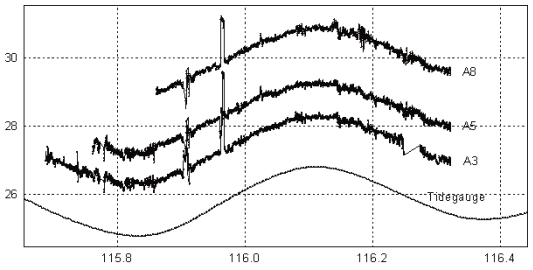

Figure 8: Example of tidal variation from the kinematic GPS points (A3, A5 and A8) compared to tide gauge data from Uummannaq. The comparison shows that the similarity of tidal phase and amplitudes also holds in the fjord systems. / Figure 8 : Exemple de variation de la marée, d'après les points GPS cinématiques (A3, A5 et A8) comparés aux données du marégraphe d'Uummannaq. La comparaison montre une similarité entre la phase de la marée et les amplitudes, également contenues dans les systèmes de fjords.

represented by the ArcGP model, at a 5' grid spacing and giving relatively high weight to the airborne gravity data; and the "GOCINA model" [*Forsberg et al*. 2004], derived at a higher resolution (3') by different methods and higher weighting of surface data. The comparisons are also shown in Table 1.

It is seen that the GPS measurements confirm that the GOCINA model is likely better than 10 cm r.m.s. in this area, with the MDT inferred from both models at least of the same sign and magnitude, and in reasonable accordance with the -40-cm estimate from the PIPS oceanographic model, cf. Figure 6. The results confirm that it is possible to obtain

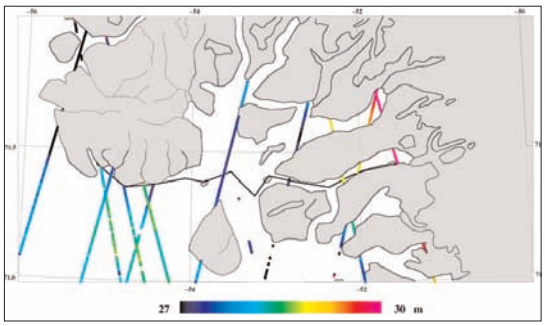

Figure 9: Ellipsoidal heights showing track location from ICESat period February 17-March 24, 2005. / Figure 9 : Hauteurs ellipsoïdales montrant l'emplacement de la trace à partir d'ICESat, période du 17 février au 24 mars 2005.

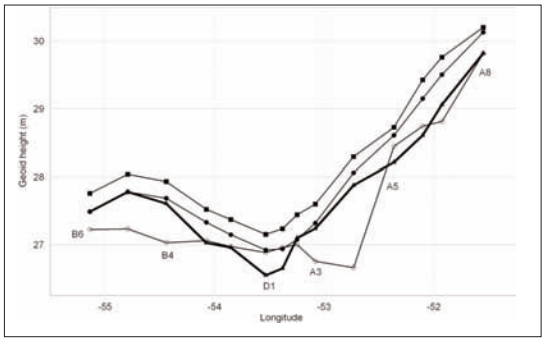

Figure 10: The two lower graphs map the measured SSH profiles from GPS (thick line) and ICESat (open circles), and the two upper graphs map two geoid models: GOCINA (filled squares) and ArcGP (filled circles). Both geoid models as well as ICESat are converted to WGS84, allowing comparison to GPS. / Figure 10 : Les deux graphiques du bas montrent les profils de la hauteur de la surface de la mer (HSM) mesurés à partir du GPS (trait large) et d'ICESat (cercles ouverts) et les deux graphiques du haut montrent deux modèles du géoïde : GOCINA (carrés pleins) et ArcGP (cercles pleins). Les deux modèles du géoïde et ICESat sont convertis au WGS84, permettant la comparaison avec le GPS.

diamètre). À la figure 9, les hauteurs ellipsoïdales d'ICESat corrigées pour les marées sont montrées, présentant les traces disponibles du 17 février au 24 mars 2005. Étant donné que la topographie dynamique moyenne est considérée comme étant pratiquement constante dans la région, les variations mesurées de la hauteur de la surface de la mer peuvent être traitées comme des variations du géoïde. La figure 10 présente les deux profils de la hauteur de la surface de la mer, tels qu'ils sont mesurés par GPS et ICESat, avec chacun deux modèles du géoïde différents. Les valeurs d'ICESat sont extraites en quadrillant les traces de la figure 9. Les modèles du géoïde sont représentés par le modèle ArcGP, avec un espacement du quadrillage de 5' et en utilisant une pondération relativement élevée pour les données gravimétriques aéroportées; le « modèle GOCINA » [Géoïde et circulation de l'océan dans l'Atlantique nord] [*Forsberg et coll*. 2004] est dérivé à une plus haute résolution (3') par différentes méthodes et une pondération plus élevée des données terrestres. Les comparaisons sont également présentées dans le Tableau 1.

L'on s'aperçoit que les mesures GPS confirment que le modèle GOCINA est probablement meilleur que 10 cm (moyenne quadratique) dans cette zone, avec la topographie dynamique moyenne déduite des deux modèles, ayant au moins le même signe et la même magnitude, et en accord raisonnable avec l'estimation de -40 cm du modèle océanographique du SPGP (système de prédiction de la glace polaire) (voir figure 6). Les résultats confirment qu'il est possible d'obtenir des précisions de l'ordre de 10 à 20 cm, même avec les déploiements rapides du GPS, et que les profils de fjords semblables dans d'autres régions du Groenland peuvent ainsi être très utiles pour valider les géoïdes régionaux et les modèles internationaux, tels que EGM08. La hauteur de la surface de la mer d'ICESat montre en général la même tendance que les valeurs mesurées par GPS : des valeurs élevées au fond du fjord et des valeurs plus basses vers l'océan libre, mais avec de plus grandes variations entre les deux profils. Ces variations peuvent être tout d'abord expliquées par le nombre limité de traces disponibles d'ICESat dans la région à cette période particulière; le profil GPS croise seulement 10 traces ICESat, dont la moitié sont proches de la côte. De plus, le modèle de la marée (GOT99.2) appliqué à ICESat est un modèle international de marée, principalement fondé sur les données altimétriques de TOPEX/Poseidon; et l'on ne s'attend pas à ce que ce modèle fonctionne bien dans les zones côtières et dans les systèmes de fjords profonds. Enfin et surtout, la hauteur de la surface de la mer n'est pas corrigée pour la profondeur de la neige et les hauteurs du franc-bord des glaces de mer, en raison

Table 1: Fit of the measured SSH to two recent geoid models in Greenland. / Tableau 1 : Ajustement de la hauteur de la surface de la mer mesurée à deux modèles récents du géoïde au Groenland.

Units/Unités : m	All GPS ice points(14)/ Tous les points GPS de glace (14)		Kinematic GPS ice points only(6)/ Seulement lespoints GPS de glace cinématiques (6)	
	Mean/ Moyenne	Std.dev./ Écart-type	Mean/ Moyenne	Std.dev./ Écart-type
GOCINA geoid/ Géoïde GOCINA	-0.46	0.17	-0.41	0.13
ArcGP geoid/ Géoïde ArcGP	0.23	0.18	-0.21	0.17
ICESat SSH/ HSM ICESat	0.17	0.43	0.12	0.38

accuracies of 10-20 cm even with rapid GPS deployments, and that similar fjord profiles in other areas of Greenland could thus be very useful in the validation of both regional geoids and global models such as EGM08. The ICESat SSH shows generally the same trend as the GPS measured values with high values in the bottom of the fjord and lower values towards the open ocean, but with larger variations along the two profiles. These variations can be explained first of all by the limited ICESat tracks available in the area during this particular period; the GPS profile crosses only 10 ICESat tracks, of which half of the tracks are close to the coast. Second, the tide model (GOT99.2) applied to ICESat is a global tide model, primarily based on TOPEX/Poseidon altimetry data, which is not expected to perform well in coastal areas and deep fjord systems. Last, but not least, the SSH are not corrected for snow depths and sea-ice freeboard heights, due to the lack of open leads in the fast ice covering the area.

5. Conclusions

New geoid models based on GRACE and ArcGP, together with satellite laser and radar altimetry from ICESat and ERS, have been used for the first time to provide a realistic model of the MDT of the Arctic Ocean. ICESat allows direct measurement of sea level (or sea-ice surface heights) even in narrow straits and fjords, and in the presence of sea ice our results also illustrate that it is possible to derive realistic sea-ice freeboards. Although results of the geoid model are consistent at the 10-20 cm level in the open Arctic Ocean, they are more uncertain close

d'un manque de chenaux libres dans la glace fixée couvrant cette région.

5. Conclusions

Les nouveaux modèles du géoïde basés sur GRACE et ArcGP ont, avec l'altimétrie satellitaire, laser et radar à partir d'ICESat et ERS, été utilisés pour la première fois pour fournir un modèle réaliste de la topographie dynamique moyenne (TDM) de l'océan Arctique. ICESat permet la mesure directe du niveau de la mer (ou des hauteurs de la surface des glaces de mer), même dans les détroits et les fjords étroits; en présence de glaces de mer, nos résultats démontrent également qu'il est possible de calculer les francs-bords réalistes des glaces de mer. Même si les résultats du modèle du géoïde sont cohérents dans l'ordre de 10 à 20 cm dans l'océan Arctique libre, ils sont plus incertains près des côtes, où les communautés locales ont besoin d'information améliorée sur le géoïde, afin d'unifier les systèmes verticaux. Une petite expérience menée au Groenland avec le GPS sur les glaces de mer montre qu'il est possible de fournir une information de bonne qualité sur la hauteur de la surface de la mer dans l'ordre de 10 cm, offrant ainsi un équivalent aux données « de nivellement GPS », utilisées pour valider les modèles du géoïde dans des régions continentales plus tempérées. Un certain nombre de ces jeux de données du niveau de la mer par GPS, associés à des modèles de TDM océanographiques détaillés, peut largement contribuer au contrôle de qualité des géoïdes, et ainsi aider la définition future d'une référence altimétrique améliorée à travers l'Arctique.

to the coasts, where local communities have a need for improved geoid information to unify vertical systems. A small experiment in Greenland with GPS on sea ice shows that it is possible to provide high-quality SSH information at the 10-cm level, providing an equivalent to the "GPS-levelling" data used for validating geoid models in more temperate continental regions. A number of such GPS-sea-level data sets, combined with detailed oceanographic MDT models, could be an important contribution to quality control in geoid modelling, and thus facilitate the future definition of an improved vertical datum across the Arctic.

Acknowledgements / Remerciements

We sincerely thank Seymour Laxon and Andy Ridout, University College London, U.K., for providing the ERS MSS data; W. Maslowski, U.S. Naval Postgraduate School; and M. Steele, University of Washington, for providing oceanographic model MDT data.

Nous remercions sincèrement Seymour Laxon et Andy Ridout, University College London, R.-U., de nous avoir fourni la surface moyenne des mers ERS, W. Maslowski, de la Naval Postgraduate School américaine, et M. Steele, University of Washington, de nous avoir fourni les TDM du modèle océanographique.

References / Références

Brozena, J. M. and R. Salman. 1996. Arctic airborne gravity measurement program. In: Segawa et al. (eds) *Gravity, Geoid and Marine Geodesy*. IAG Sympsium series 117, Springer Verlag pp. 131-139.

Brozena, J. 1991. The Greenland Aerogeophysics Experiment: Airborne Gravity, Topographic and Magnetic Mapping of an entire Continent. In: Colombo (eds) *From Mars to Greenland: Charting Gravity with Space and Airborne Instruments*. IAG Symposium Series 110, Springer Verlag pp. 203-214.

Forsberg, R. and S. Kenyon. 2004. Gravity And Geoid in The Arctic Region – The Northern Polar Gap Now Filled. *Proceedings GOCE Workshop, ESA-ESRIN*, March 2004, ESA SP-562, p. 6.

Forsberg, R., H. Skourup, O. B. Andersen, P. Knudsen, S. W. Laxon, A. Ridout, J. Johannesen, F. Siegismund, H. Drange, C. C. Tscherning, D. Arabelos, A. Braun and V. Renganathan. 2007. Combination of Spaceborne, Airborne and In-Situ Gravity Measurements in Support of Arctic Sea Ice Thickness Mapping. Danish National Space Center, Technical Report No. 7, pp 136.

Forsberg, R. and H. Skourup. 2005. Arctic Ocean Gravity, Geoid and Sea-ice Freeboard Heights from ICESat and GRACE. Geophyscial Research Letters, Vol. 32, L21502, doi:10.1029/2005GL023711.

Forsberg, R., A. V. Olesen, A. Vest, D. Solheim, R. Hipkin, O. Omang and P. Knudsen. 2004. Gravity Field Improvements in the North Atlantic Region. *Proceeding GOCE Workshop, ESA-ESRIN*, March 2004, ESA SP-562.

Forsberg, R. and M. G. Sideris. 1993. Geoid computations by the multi-band spherical FFT approach. Manuscripta Geodaetica, 18 pp. 82-90.

Hvidegaard, S. M. and R. Forsberg. 2002. Sea ice thickness from airborne laser altimetry over the Arctic Ocean north of Greenland, Geophysical Research Letters, 29(20), pp. 1952-1955.

Laxon, S., N. Peacock and D. Smith. 2003. *High interannual variability of sea ice thickness in the Arctic Region, Nature* 425, pp. 947-950.

Morison, J., M. Steele, T. Kikuchi, K. Falkner and W. Smethie. 2006. Relaxation of central Arctic Ocean hydrography to pre-1990s climatology. Geophysical Research Letters, Vol. 33, L17604, doi:10.1029/2006GL026826.

Steele, M., J. Morison, W. Ermold, I. Rigor, M. Ortmeyer and K. Shimada. 2004. Circulation of summer Pacific halocline water in the Arctic Ocean. *Journal of Geophysical Research*, Vol. 109, C02027, doi:10.1029/2003JC002009.

Tapley, D. B., S. Bettadpur, J. Ries, P. Thomson and M. Watkins. 2004. GRACE measurements of mass variability in the earth system. Science, 305, issue 5683, 503-505 [doi: 10.1126/science.1099192].

Zwally, H. J. et al. 2002. ICESat's laser measurements of polar ice, atmosphere, ocean and land, *Journal of Geodynamics*, 34, pp. 405-445.

Authors / Auteurs

Henriette Skourup received her M.Sc. from the University of Copenhagen in 2004. She worked as a research assistant at the Danish National Space Center until starting a Ph.D. program in January 2006 in Arctic Ocean sea-ice thickness and mean sea level from satellite altimetry. Since 1997, her experience has been in sea ice. She worked part-time during her studies as a sea-ice analyst at the Danish Meteorological Insitute. Since 1999, she has joined several field campaigns, primarily in airborne altimetry and gravity surveying in the Arctic, Mongolia and Germany.

Henriette Skourup a obtenu une maîtrise ès sciences de l'Université de Copenhague en 2004. Elle a travaillé comme assistante de recherche au Centre spatial national danois jusqu'au moment où elle a débuté un programme de doctorat en janvier 2006 sur la mesure de l'épaisseur des glaces de mer

et du niveau moyen de la mer de l'océan Arctique au moyen de l'altimétrie satellitaire. Son expérience des glaces de mer remonte à 1997, puisqu'elle a travaillé à temps partiel pendant ses études comme analyste des glaces de mer à l'institut danois de météorologie. Depuis 1999, elle a participé à plusieurs campagnes sur le terrain touchant l'altimétrie aéroportée et les levés gravimétriques en Arctique, en Mongolie et en Allemagne.

Rene Forsberg received his M.Sc. from the University of Copenhagen in 1980. He joined the Danish Geodetic Institute as research geodesist working in the fields of gravimetry, satellite geodesy and on Greenland projects. He was a visiting scientist at Ohio State University in 1983-84 and the University of Calgary in 1984-85. Since 1989, Rene has been an external lecturer in the Department of Geophysics at the University of Copenhagen, and Department Head of the Geodynamics Department at the National Survey and Cadastre since 1997. He has held the same position, at the Danish National Space Center, since 2005. He is a member of the scientific advisory board for the ESA Cryosat mission, and Chairman of the IAG International Gravity Field Service, since 2003. Since 1978, Rene has authored and coauthored more than 200 papers.

Rene Forsberg a obtenu une maîtrise ès sciences de l'Université de Copenhague en 1980. Il est entré à l'institut danois de géodésie en tant que chercheur en géodésie sur des projets sur le terrain concernant la gravimétrie, la géodésie par satellite et le Groenland. Il a été scientifique invité à l'Université de l'État de l'Ohio (1983-1984) et à l'Université de Calgary (1984-1985). Depuis 1989, il oeuvre en tant que conférencier extérieur au département de géophysique de l'Université de Copenhague. Il est chef du service de géodynamique du National Survey and Cadastre depuis 1997 et occupe le même poste au Centre spatial national danois depuis 2005. Il est membre du conseil scientifique formé pour la mission CryoSat de l'ESA et président du International Gravity Field Service de l'Association internationale de géodésie depuis 2003. Rene a écrit et coécrit plus de 200 articles depuis 1978.❑